The Dissertation Committee for Tianheng Feng Certifies that this is the approved version of the following Dissertation:

MODELING AND CONTROL OF DRILLSTRING DYNAMICS FOR VIBRATION SUPPRESSION

Committee:

Dongmei Chen, Supervisor

Dragan Djurdjanovic

Joseph J. Beaman

Raul G. Longoria

Spyros A. Kinnas

MODELING AND CONTROL OF DRILLSTRING DYNAMICS FOR VIBRATION SUPPRESSION

by

Tianheng Feng

Dissertation

Presented to the Faculty of the Graduate School of

The University of Texas at Austin

in Partial Fulfillment

of the Requirements

for the Degree of

Doctor of Philosophy

The University of Texas at Austin

May 2019

Acknowledgements

First, I want to express my sincere gratitude to my doctoral supervisor, Dr. Dongmei Chen. She is wise and patient, guides me and encourages me when I have difficulties in researches. This dissertation won't be possible without her support. She is more than a supervisor, who I can share my happiness and sadness. She gave me courage and strength to walk over this difficult yet enjoyable journey.

Second, I want to thank the professors on my Ph.D. defense committee: Dr. Djurdjanovic, Dr. Beaman, Dr. Longoria, and Dr. Kinnas. Thank you for the feedback and suggestions on this dissertation. I learned time serial, stochastic control, system modeling, and numerical methods from them. The valuable knowledge from these classes was very helpful to my research.

Third, I would like to appreciate all my lab-mates in Dr. Chen's group. I benefit a lot from the discussions with them. Zheren and Soovadeep, in particular, set great role models for me. They are smart and dedicated to their work. Talking to these smart minds always gives me inspirations.

Finally, I want to thank my family. My parents give me their best. I would not go this far without their support. Thank my mom, Jing for her selfless love. Thank my wife, Huidong. Eight years ago, we first met in SJTU. After overcoming so many difficulties, we finally got married in Austin while pursuing our doctoral degrees in UT. Thank you for taking good care of our little family while being busy as a doctoral student. You become the person who knows me best after going through all these things together. It's lucky to have you in my life.

Abstract

Modeling and Control of Drillstring Dynamics for Vibration Suppression

Tianheng Feng, Ph.D.
The University of Texas at Austin, 2019

Supervisor: Dongmei Chen

Drill-string vibrations could cause fatigue failure to downhole tools, bring damage to the wellbore, and decrease drilling efficiency; therefore, it is important to understand the drill-string dynamics through accurately modeling of the drill-string and bottom-hole assembly (BHA) dynamics, and then develop controllers to suppress the vibrations. Modeling drill-string dynamics for directional drilling operation is highly challenging because the drill-string and BHA bend with large curvatures. In addition, the interaction between the drill-string and wellbore wall could occur along the entire well. This fact complicates the boundary condition of modeling of drill-string dynamics.

This dissertation presents a finite element method (FEM) model to characterize the dynamics of a directional drill-string. Based on the principle of virtual work, the developed method linearizes the drill-string dynamics around the central axis of a directional well, which significantly reduced the computational cost. In addition, a six DOF curved beam element is derived to model a curved drill-string. It achieves higher accuracy than the widely used straight beam element in both static and dynamic analyses.

As a result, fewer curved beam elements are used to achieve the same accuracy, which further reduces the computational cost.

During this research, a comprehensive drill-string and wellbore interaction model is developed as the boundary condition to simulate realistic drilling scenarios. Both static and dynamic analyses are carried out using the developed modeling framework. The static simulation can generate drill-string internal force as well as the drilling torque and drag force. The dynamic simulation can provide an insight of the underlying mechanism of drilling vibrations. Top drive controllers are also incorporated as torsional boundary conditions. The guidelines for tuning the control parameters are obtained from dynamic simulations.

Drill-string vibrations can be suppressed through BHA configuration optimization. Based on the developed modeling framework, the BHA dynamic performance is evaluated using vibration indices. With an objective to minimize these indices, a genetic algorithm is developed to optimize the BHA stabilizer location for vibration suppression. After optimization, the BHA strain energy and the stabilizer side force, two of the vibration indices, are significantly reduced compared to the original design, which proves the BHA optimization method can lead to a significant reduction of undesirable drilling dynamics. At the end of this dissertation, reduced order models are also discussed for fast simulation and control design for real time operation.

Table of Contents

List of Tables

List of Figures

Chapter 1. INTRODUCTION

1.1. Drilling Background

Oil and gas provide affordable and reliable energy to power modern society, and drilling constitutes a large portion of the oil and gas mining cost [1]; therefore, drilling is intensively studied by both academia and industry. In recent decades, directional drilling has gained a wide application with the development of advanced navigation and steering systems [2]. These techniques involve deviating a well along a predefined path to a target located at a certain horizontal distance from the rig [3]. Using directional drilling technology, multiple rigs and wells can be grouped together for increased drilling and production efficiencies. The ground facilities and underground obstacles can be avoided through an extended reach of the well in the horizontal direction [4]. This technology can also be used to remedy blowout by intersecting the trouble well using a relief well [5].

1.2. Rotary Drilling System Basics

The rotary drilling system is most commonly used in the oil and gas industry. It mainly consists of a hoisting unit, a rotating unit, and a circulating unit [6]. Through rock cutting and hydraulic fracture, this system is able to drill a well longer than 10 kilometers [7]. Figure 1-1 illustrates a typical rotary drilling system. A draw-works is used to hoist the drill-string and move it up and down. A top drive (or rotary table) is fixed on the rig and creates torque to drive the drilling system. The drill-string, which is connected by

long slender drill-pipes (common length: 27-32 ft, common outer diameter: 3.5 in, 4.5 in and 5 in), transmits driving torque from the top drive to the bit.

Located at the lower end of the drill-string is the bottom-hole assembly (BHA), which mainly consists of thick-wall drill collars. Since the length-to-diameter ratio of the drill-string is very high, the BHA must be heavy enough to pull the drill-string in tension to avoid buckling. The additional BHA weight is applied on the bit to help crush rocks. Stabilizers have larger diameters than drill-collars. They can keep the BHA centralized within the borehole and increase BHA stiffness. Some stabilizers also have blades to aid the cutting process. Rotary steerable systems (RSS) are devices used to steer the BHA toward the desired direction to build the well. Based on the deviating mechanism, RSS can be classified into push-the-bit RSS and point-the-bit RSS [8]. The former uses pads outside the BHA to press against the wellbore and cause a direction change at the bit. The latter bends the BHA internally with a non-rotating shaft curved inside the BHA housing [9][10].

For better measurement and control of bottom-hole activities, many BHAs are also equipped with measurement-while-drilling (MWD) tools [11], logging-while-drilling (LWD) tools [12], and telemetry tools [13]-[15] to measure, record, and transmit downhole information. During drilling operation, the drilling fluid (called *mud*) will circulate through the hollow drill-pipes, bit nozzle, well annulus (the gap between drill-string and wellbore), and then back to surface. In this procedure:

1. The bit gets lubricated for cutting and friction;
2. Heat generated from cutting and friction is carried out;

3. Cutting debris is transported to surface from bottom hole;
4. Rock breaking process is expedited through hydraulic fracture;
5. Bottom-hole pressure is maintained at designed level to prevent formation fluid from entering well annulus.

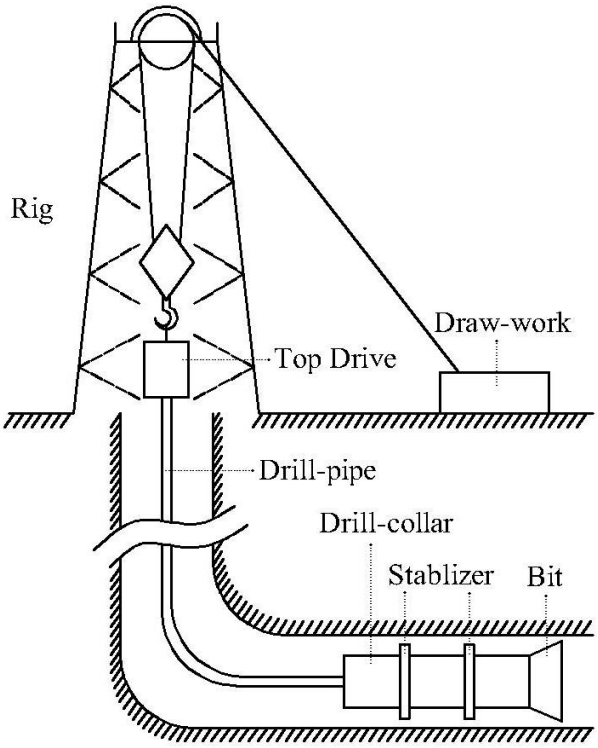

Figure 1-1. Rotary drilling system

1.3. Drilling Vibration

Drill-string vibration can manifest in axial, lateral, and torsional directions and cause phenomena known as bit bounce, whirl, and stick-slip, respectively [16]-[18]. Vibration is very common and generally detrimental to drilling operations. Excessive vibration could cause fatigue failure of the drill-string, increase the wear rate of the bit and BHA, as well as reduce drilling efficiency [19]. Failure of downhole tools and the

associated non-drilling period can significantly increase drilling costs. In directional drilling, vibrations can also influence directional control, cause well instability, and harm wellbore quality [20].

The axial bit bounce is characterized by the bit temporarily lifting off the bottom-hole formation [21]. It usually happens with roller-cone bits and can cause damage to the bit bearing and cutter.

The torsional stick-slip is characterized by large velocity fluctuation of the bit under a relatively constant top drive speed [22]. In some extreme cases, the peak speed of the bit can be ten times as high as the speed of the top drive [23]. Stick-slip is initiated at bit side, where a torsional wave is generated due to velocity-weakening mechanisms [24]. As the wave travels upwards and hits the stiff top drive, it will be reflected into the drill-string and stick-slip becomes self-sustained at its torsional natural frequencies [25]. Stick-slip can cause BHA fatigue, twist off connections, and reduce drilling rate.

The lateral vibration is usually manifested as whirl, where the bit rolls around the wellbore aggressively [26]. Whirl vibration frequency can be up to tens of Hz [7] and the amplitude is restricted by the narrow annulus; therefore, the lateral waves easily attenuate before reaching surface. As a result, whirl is usually unobservable to the rig and has been overlooked for decades. After equipping downhole MWD and LWD tools, these vibrations have been studied [27]-[29]. Usually, the BHA is manufactured with some out-of-balance mass (by defect or on purpose) to increase wellbore clearance. As the drill-string rotates, a centrifugal force is produced, leading to a forward whirl [26]. Another form is called backward whirl, which is caused by the friction between BHA/bit and

wellbore. Whirl can produce large side forces between BHA/bit and wellbore; therefore, resulting in undesirable deviation of well profile and causing failure of downhole tools.

The vibrations in the axial, torsional, and lateral directions are usually coupled. When stick-slip happens, the high rotary speed in the slip phase can result in a large centrifugal force and lead to a lateral vibration. The contact force in lateral direction can also contribute to the axial force as the drill-string slides, and to the torsional torque as the drill-string rotates. Since vibrations can significantly influence drilling operations, the MWD and LWD tools usually have a dedicated unit to detect and analyze downhole vibrations. The lateral vibration wave quickly attenuates when traveling upwards; therefore, it can only be determined by downhole measurements [30]. The telemetry device can transmit the measured downhole information to the surface. However, the mud pulse telemetry, which is most widely used by drilling industry, has very limited bandwidth (common value, 8-10 *bits*/*s*) [30]. As a result, the large downhole data cannot be directly transmitted to surface and data compression is necessary beforehand. In [31], the vibration level was determined based on the root-mean-square value of BHA lateral acceleration. In [32], shock, measured in counts per second, was used to indicate the lateral vibration severity. In the same report**,** stick-slip severity level was determined by the percentage of time during a stick-slip cycle that the downhole string rotation was below 5 rpm. The above practices used vibration level to indicate and compress downhole vibration information and make real-time communication possible. The torsional waves can travel much further and are observable to the top drive. In [33], torque fluctuation is measured at the top end of a drill-string, and then BHA rotary speed

is calculated backwards to detect stick-slip vibration. Drilling vibrations are well observed by drilling industry and measured by MWD and LWD tools. A lot of research has been conducted to model these vibrations and to mitigate them.

1.4. Drilling Mechanics and Models

The primary function of a drill-string is to transmit torsional motion to the bit. A driving torque is loaded by the top drive on the upper side of a drill-string. At the lower side, a reactive torque, called *torque on bit* (TOB), is produced due to bit-rock interaction. Typical TOB can range from 0.5 kNm to 10 kNm [34]. In the axial direction, the drill-string is hoisted by draw-works and the hoisting force, called *hook load*, controls the up and down motion of the drill-string. As discussed in previous sections, the BHA is heavy enough to keep the slender drill-pipes in tension and the additional weight can act on the bit, pushing it to crush the rock. The reactive force from the bottom hole is called *weight on bit* (WOB). From the discussion above, the whole drill-pipe and the upper part of BHA are in tension, while the lower part of BHA is in compression.

In directional wells, the drill-string can have a lateral contact with wellbore due to its internal bending moment and gravity. Normal force is produced at contacting positions, which causes a frictional *torque* as the drill-string rotates, and a frictional *drag* as the drill-string slides down or trips out. Since the drill-string is saturated in mud, the buoyance and viscous damping also need to be considered.

1.4.1. Drilling Statics

Based on the static analysis, the strain and stress distribution along the BHA can be obtained to evaluate the BHA structure; external forces, such as static WOB, wellbore contact, torque and drag can be obtained with given well profile and operating parameters; contact positions can also be obtained for modal analysis. In [35], Johancsik et. al. proposed a soft-string model to calculate the torque and drag. This method assumes the drill-string continuously lies down on wellbore. The contact force is obtained by analyzing each lumped mass segment, and the drag and torque are obtained based on the Coulomb friction theorem. In [36], Sheppard et. al. included mud buoyance and hydraulic pressure to improve the soft-string model. However, since drill-string stiffness and wellbore clearance are ignored, the soft-string method lacks accuracy [37]. A transformation was made by Ho et. al. in [38], which presented a hybrid model combining stiff BHA and soft drill-pipes. In recent research [39]-[41], fully stiff drill-string models were presented to calculate torque and drag and achieved improved accuracy. Although some dynamic methods are also proposed [37], static analysis is still the common practice for torque and drag calculation considering its high computational efficiency and accuracy.

Besides torque and drag calculation, in [42], Tan proposed a three-dimensional finite element method (FEM) model to analyze the statics of directional drill-strings. Drill-string deformation, contact force, and static WOB are obtained for any drill-bit design. In [43], Millheim et. al. applied an FEM model to calculate the side force of a BHA assuming the stabilizers are pinned by the wellbore. Based on the lateral force obtained at bit side, BHA pointing tendency can be determined for well propagation

prediction. In [44], Wilson et. al. obtained BHA contacts based on static analysis. The result is applied as boundary conditions for modal analysis. In [45] and [46], Bailey et. al. developed a lumped model to characterize BHA lateral behaviors. Static analysis is performed to get BHA deflection, rotation, contact force, and bending moment to evaluate BHA performance.

1.4.2. Drilling Dynamics

In addition to static analysis summarized above, drill-string dynamics is also extensively studied to explore downhole vibrations and to develop vibration mitigation control. Drill-string dynamic analysis can be further divided into steady-state dynamic analysis and transient dynamic analysis. The steady-state dynamics can be easily obtained by decoupling vibration amplitude from vibration frequency, which is equal to the excitation frequency. In [47], Spanos et. al. applied this method to get BHA dynamic transfer function using its natural modes. In [45] and [46], Bailey et. al. obtained BHA lateral mode shapes over a frequency range, which are used to calculate vibration indices to evaluate BHA performance. The transient dynamics involves a time-integration process. Although more computationally expensive, the transient dynamic model can accept generic boundary conditions without assuming periodic excitation. Most dynamic analysis falls into the latter category and various modeling methods have been developed to understand and mitigate drilling vibrations.

1.4.3. Drill-string Models

In this section, different modeling methods are discussed and compared with a focus on drill-string transient dynamics, including the lumped-parameter method, the transfer matrix method, and FEM.

The lumped-parameter model represents the continuous drill-string with discrete mass-spring-damper system, where the heavy BHA is modeled as a lumped mass and the slender drill-pipe is modeled as a spring. This method is computationally fast and easy to implement; therefore, widely used for bit-rock interaction study and control design. In [48] and [49], Yigit and Christoforou applied the lumped-parameter model to analyze the axial and transverse vibrations of a rotary drilling system. In [24], Richard et. al. implemented this method to explore the root cause of BHA stick-slip vibration. In [50], Leine et. al. investigated stick-slip, whirl, and their coupling mechanism with the lumped model. Some lumped-parameter models can simulate more degrees of freedom (DOF) using multiple masses and springs [51]. However, the simplification of lumped mass and spring sacrifices much accuracy. In addition, since bending stiffness is ignored, the lumped-parameter models are usually not suitable for directional drilling analysis.

The transfer matrix method solves the structural wave equations analytically in the frequency domain. Through inverse Fourier transform, the motions and forces at two ends of the drill-string are correlated using time-delay matrices. Using this method, in [52], Han et. al. analyzed the axial, torsional, and flexural dynamics of a hollow pipe. In [53], Kreuzer et. al. modeled drill-string torsional dynamics using the transfer matrix method, and developed a controller based on it to reduce wave reflection from the surface. The transfer matrix method can generate the analytical solution in the case of

conventional drilling but is inextensible to directional drilling. In addition, this method cannot deal with the changing cross-sectional area; therefore, the complex geometric features of the BHA cannot be completely captured.

FEM can solve beam wave equations with a high-fidelity, weak-form solution. Although more computationally expensive when compared with the other two methods, the advantages of FEM are significant. Using FEM, six DOF vibrations and dynamics along the entire drill-string can be accurately obtained. In addition, FEM models can easily incorporate comprehensive boundary conditions and reproduce realistic drilling scenarios; therefore, has gained a wide application in drill-string dynamic analysis. In [54], Millheim et. al. presented a three-dimensional dynamic FEM model to study the propagating tendency of the bit and gained an increased accuracy compared with its static counterpart. In [55], Khulief et. al. developed an FEM model for drill-string using the Lagrangian method. An order reduction was also achieved through modal transformation. In [56], Ritto et. al. modeled the uncertainties of bit-rock interactions in the finite element analysis of drill-string vibration. The aforementioned FEM models and most research in this field still focus on vertical wells where the drill-string vibrates around its natural position linearly. With respect to directional drilling, the bending displacements are large; therefore, the geometry nonlinearity cannot be neglected. In [57], a four DOF FEM model was implemented for directional drilling considering drill-string and wellbore interaction. However, the internal force associated with large bending is ignored. In [42], Tan proposed an FEM model to investigate the static force applied on a directional drill-string using displacement decomposition to account for large drill-string displacement.

However, the developed model is stationary, thus unable to deal with the dynamic vibration problem. Another shortcoming of current research is oversimplifying the boundary conditions, especially the external forces applied on the bit. This oversimplification could result in misrepresentation of the drill-string dynamics. It is necessary to develop a comprehensive modeling framework to adequately consider both drill-string dynamics and bit forces.

1.5. Drilling Vibration Mitigation

As discussed in earlier sections, drilling vibrations can cause fatigue failure of downhole tools, cause damage to the wellbore, and reduce *rate of penetrate* (ROP, to measure drilling rate). To increase drilling efficiency and reduce drilling cost. Many methods have been proposed to mitigate drilling vibrations.

1.5.1. Passive Method

Passive methods do not use any external power but improve the inherent system to reduce drilling vibrations [58]. This can be achieved through bit redesign, adding a vibration absorber and changing the BHA structure. In [59], Barton et. al. presented a new PDC bit to reduce drilling vibration. The proposed PDC bit has 6 blades with 16 mm cutters, and a tapered structure used to reduce friction. In [60], Pessier et. al. presented a hybrid bit which can take as high WOB as a roller-cone bit and can sustain *revolutions per minute* (RPM) comparable to a PDC bit. Based on the test results, this bit can reduce stick-slip at low RPM and reduce whirl at high RPM. In [61], Schwefe et. al. developed a

PDC bit to mitigate stick-slip vibration. The TOB can be reduced by drilling with a manageable depth of cut (DOC).

The vibration absorber is a device to provide additional damping to BHA structure [62]. When shock happens, it is able to dissipate the impulse energy inputted to BHA and smoothen the drilling process. This device can be used in both axial and torsional directions. In [63], a vibration absorber is installed, and the test results indicate a reduction of severe vibration by 46%.

Another passive method is changing BHA design. The underlying idea is to make BHA natural frequencies different from the operating RPM and avoid resonance. In [64], Dareing et. al. found BHA axial and torsional natural frequencies can fall into drill-string operating RPM which can cause resonance. To avoid this problem, the authors proposed to increase the lengths of the drill-collar and the heavy drill-pipe to reduce BHA natural frequency. In a series of work from Exxonmobil [45][46], Bailey et. al. modified BHA lateral dynamics through changing stabilizer positions. In a redesigned BHA, the near-bit stabilizer was removed and the roller ream was moved up to the heavy wall drill-pipe. According to field tests, the new BHA had less lateral and torsional vibrations, and the average ROP was also significantly increased.

1.5.2. Active Method

Active methods reduce downhole vibrations through adjusting operating parameters. Based on field observations [65], stick-slip usually happens at low RPM and high WOB; forward whirl tends to appear at high RPM and low WOB; backward whirl is

more likely to occur at high RPM and high WOB. Accordingly, these vibrations can be avoided by carefully operating the drill-string with medium WOB and RPM. However, overly adjusting RPM and WOB can sacrifice the potential of increasing ROP with less conservative RPM and WOB [58]. A higher-level active method is to adjust the top drive (or rotary table) torque and speed to reduce downhole vibrations especially the stick-slip vibration. Active methods can cure stick-slip vibration more effectively than the passive methods [33].

In [66], a robust H_∞ linear controller was implemented to suppress stick-slip oscillation and to improve the transient behavior of the drilling system. In [67] and [68], a sliding model control was implemented to suppress stick-slip considering external disturbances. In [69], the authors developed a controller based on back-stepping technique to stabilize stick-slip vibration, and an observer is designed to estimate the unmeasurable states. Among many controllers developed by industry and academy, two kinds of control strategies have achieved commercialization and been applied in real drilling rigs: the soft torque method and the soft speed method.

The underlying idea of the soft torque method is to control top drive (or rotary table) torque to make it work as an energy absorber for torsional waves [70][71]. This can be achieved by feeding surface torque fluctuation back into a speed Proportional-Integral (PI) controller. As a result, the reflection rate of the torsional waves can be reduced at the top drive, which helps to mitigate the stick-slip vibrations. As an additional benefit, the smoother bit rotation can also result in a reduction of axial and lateral vibrations [70]. In real world applications, the torque signal is hard to measure. Therefore, in [72], Jansen et.

al. estimated torque fluctuations indirectly by monitoring motor current and reported improved results of the soft torque method.

The soft speed controller keeps the form of a speed PI controller, where the proportional gain and integral gain are carefully selected to damp out torsional vibrations at desired frequencies [73]. The frequency where maximum damping happens can be determined by tuning the integral gain. Further tuning the proportional gain changes the reflection rate of the torsional waves. A small reflection rate can effectively reduce BHA stick-slip. However, the speed fluctuation at surface increases as a side effect. Accordingly, a certain level of reflection rate needs to be maintained to keep top drive speed constant. Hardware-in-the-loop tests and field tests indicate that the soft speed method can effectively mitigate BHA stick-slip vibration [73]. Usually, the stick-slip frequency is the first torsional natural frequency of a drill-string. In some cases, high order modes can be excited. In [74], Kyllingstad selected the absorbing frequency in between different modes and balanced the reduction of reflection rate at different frequencies.

1.6. Objectives of This Research

The objectives of this research are to establish a comprehensive and high-fidelity modeling framework for directional drilling analysis and explore methodologies to suppress drill-string vibrations. This modeling framework can predict the dynamics of drill-string vibrations and help understand the underlying mechanisms subject to these vibrations. Based on the modeling result, top drive controllers will be developed and

BHA structure optimizations will be performed to mitigate the undesired drill-string dynamics.

1.7. Outline of This Dissertation

This dissertation studies drill-string modeling, design, and control. The high-fidelity FEM is implemented to model directional drill-strings and a comprehensive boundary condition is applied to simulate realistic drilling scenarios. Both static and dynamic analyses are carried out using the proposed modeling framework. The static simulation can obtain the drill-string internal force as well as drilling torque and drag. The dynamic simulation can provide an insight of the mechanism of drilling vibrations. For BHA structure design, its dynamic performance is evaluated using vibration indices. With an objective to minimize these indices, an algorithm is proposed to relocate BHA stabilizers for vibration suppression. With proper model reduction, such as using lumped-parameter models and reduced order FEM models, controllers are designed to actively mitigate the stick-slip vibrations. The above topics are discussed in five chapters as follows.

Chapter 2, *Directional Well Trajectory*, studies the approach to generate the three-dimensional well trajectory. Well trajectory plays an important role in directional drilling analysis. Drill-string displacement can be conveniently represented with reference to the well trajectory. Additionally, the well trajectory along with well clearance also determines the boundaries for interaction between the drill-string and wellbore. However, there is no convenient sensor that is able to measure the continuous well trajectory;

therefore, interpolation algorithms become necessary. In this chapter, the minimum curvature method is discussed, which obtains continuous well trajectories from discrete survey data, such as *measured depth* (MD, measures the length of well drilled), *inclination* (measures the angle between well and vertical direction), and *azimuth* (measures the angle between well and north direction).

Chapter 3, *Drill-string Finite Element Model*, derives finite element methods to simulate drill-string statics and dynamics. The large bending of directional drilling involves nonlinearities to drill-string vibrations. To increase computational efficiency, an FEM model is developed based on the principle of virtual work, which linearizes drill-string dynamics around the central axis of a directional well. In addition, a six DOF curved beam element is derived to model curved drill-string. Compared with straight beam elements, the developed curved beam element is free from discretization error and achieves higher accuracies in both static and dynamic analyses. As a result, fewer curved beam elements can be used to achieve the same accuracy, which further reduces the computational cost.

Chapter 4, *Boundary Condition and Numerical Method*, develops the boundary conditions for directional drillings, which include models for the top drive and the draw-works, a model for drill-string and wellbore contact, and a model for bit forces. By combining the FEM models and the boundary conditions, a comprehensive modeling framework is established for directional drilling. Numerical methods are presented for static and dynamic analyses. From static analyses, drilling torque and drag are calculated to prevent drilling failure. The strain and stress distributions along the drill-string is

obtained to avoid stress concentration. From dynamic analyses, the normal drilling scenarios, the stick-slip vibrations, and the whirling vibrations are simulated using the proposed FEM modeling framework. Top drive controllers, such as the soft speed controller and the soft torque controller are also incorporated as torsional boundary conditions. The guidelines for tuning the control parameters are obtained from dynamic simulations.

Chapter 5, *BHA Configuration Optimization*, proposes a framework to optimize BHA structure for vibration suppression. Based on FEM simulations, vibration indices, such as the BHA strain energy and the stabilizer side forces, are calculated to formulate the cost function. The cost function is nonconvex within the feasible domain; therefore, the genetic algorithm (GA) is selected to solve the nonconvex optimization problem. The proposed optimization framework can find the optimal solution with a high accuracy and low computational effort. After optimization, the BHA strain energy and the stabilizer side force are significantly reduced compared to the original design, which proves the developed BHA design optimization framework can lead to a significant reduction of undesirable drilling dynamics.

Chapter 6, *Reduced Order Model and Control*, studies reduced order models for fast simulation. First, low order FEM models and modal truncated FEM models are developed, which capture drill-string dynamics at low frequencies where stick-slip happens. A lumped parameter model is also established, which can represent the first mode of a drill-string. Based on the lumped parameter model, dynamic programming (DP) is implemented to get the optimal policy that minimizes the stick-slip vibrations. A

dimension reduction is also performed to eliminate the dependence of control input on BHA rotary speed, which significantly increases the computational efficiency and makes online optimization possible.

Chapter 2. DIRECTIONAL WELL TRAJECTORY

Getting three-dimensional well trajectory is the first step to analyze drilling statics and dynamics. With reference to well central axis, drill-string displacements can be conveniently represented. Wellbore boundaries can also be determined by the well trajectory. However, there is no such sensor that can measure the continuous well trajectory; therefore, interpolation is necessary to fill the gap in between discrete survey points. Usually, the interval between two consecutive survey points is around 90 ft (the length of three drill-pipes) when taking survey with MWD tools. High resolution surveys can be taken using the wireline where the interval in between two survey points is less than 1 ft. *Measured depth*, *inclination*, and *azimuth* are most used parameters to generate a well trajectory, where the measured depth can be determined by calculating the length of drill-string, inclination and azimuth can be measured using magnetometer and gyroscope.

2.1. Minimum Curvature Method

The minimum curvature method is well accepted by oil and gas industry to calculate three-dimensional well trajectory. It assumes the adjacent points on the well trajectory are connected by circular arcs with the orientation determined by inclination and azimuth [75]. This algorithm accepts the measured depth, bit inclination, and bit azimuth as inputs and converts them to north-east-vertical (NEV) coordinate to determine

the well trajectory. Given an initial position (usually assign $[0\ \ 0\ 0]^{\mathrm{T}}$ to rig position for initialization), Eq. (2.1) is used to calculate the coordinates of the survey points [75]

$$\boldsymbol{p}_{i+1} = \boldsymbol{p}_i + \frac{f(\alpha_i)(s_{i+1} - s_i)}{2}\left[\boldsymbol{t}(\theta_i, \phi_i) + \boldsymbol{t}(\theta_{i+1}, \phi_{i+1})\right] \tag{2.1}$$

$$\begin{cases} f(\alpha) = \dfrac{\tan(\alpha/2)}{\alpha/2}, & \alpha \geq \xi \\ f(\alpha) = 1 + \dfrac{a^2}{12}\left(1 + \alpha^2/10\left(1 + \alpha^2/168\left(1 + 31\alpha^2/18\right)\right)\right), & \alpha < \xi \end{cases} \tag{2.2}$$

where $\boldsymbol{p}_i$, equal to $[N\ E\ V]_i^{\mathrm{T}}$, is the coordinates of the i^{th} survey point; s_i is the measured depth of the i^{th} survey point; $\boldsymbol{t}$ calculates the tangent direction of a directional well; α_i is the extended angle of the i^{th} segment; ξ is a small positive value, when α is close to zero, the first equation of Eq. (2.2) becomes singular and the second equation is applied to approximate the first one using Taylor expansion. The relationship between the measurements and the NEV coordinates is illustrated in Figure 2-1.

In Eq. (2.1), α_i indicates the extended angle of the well at the i^{th} segment. According to [75], it can be calculated by

$$\alpha_i = 2\sin^{-1}\left\{\left[\sin^2\left(\frac{\theta_{i+1} - \theta_i}{2}\right) + \sin(\theta_i)\sin(\theta_{i+1})\sin\left(\frac{\phi_{i+1} - \phi_i}{2}\right)\right]^{1/2}\right\} \tag{2.3}$$

With α_i, dogleg severity (DLS, in degrees per 100 ft) can be calculated to describe the deflecting rate of a directional well, given by

$$DLS = \frac{18000\alpha_i}{\pi S_{i,i+1}} \tag{2.4}$$

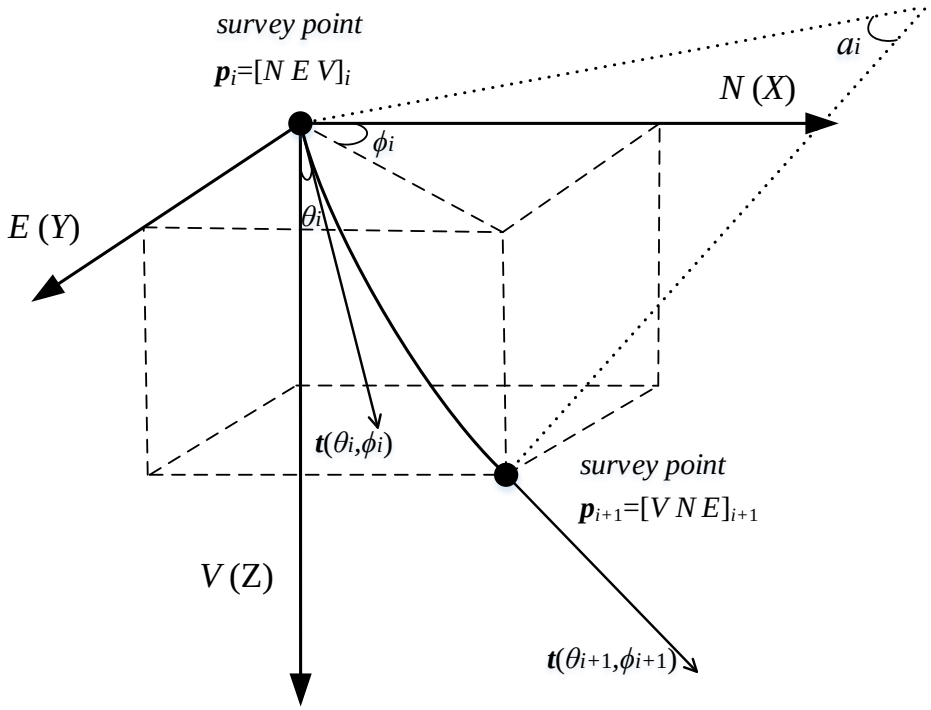

Figure 2-1. NEV coordinate frame where *N*, *E*, and *V* coincide with the global axes *X*, *Y*, and *Z*

$\boldsymbol{t}$ is tangent to the well trajectory and points to the deeper measured depth. It can be obtained from the inclination θ and the azimuth ϕ, given by

$$\boldsymbol{t}(\theta,\phi)=\begin{bmatrix}\sin(\theta)\cos(\phi)\\ \sin(\theta)\sin(\phi)\\ \cos(\theta)\end{bmatrix} \tag{2.5}$$

With Eqs. (2.1), (2.2), (2.3), and (2.5), the coordinates of discrete survey points can be obtained. In between survey points, interpolation is implemented to get the continuous well trajectory. In the segment *i*, define S_i^* as the interpolating length starting from survey

point i (so the total MD is $s_i + S_i^*$), and the corresponding extended angle α_i^*, well tangent direction $\boldsymbol{t}_i^*$, and NEV coordinate $\boldsymbol{p}^*$ can be determined by

$$\alpha_i^* = \frac{S_i^* \alpha_i}{S_{i,i+1}} \tag{2.6}$$

$$\boldsymbol{t}_i^* = \frac{\sin\left(\alpha_i - \alpha_i^*\right)}{\sin\left(\alpha_i\right)} \boldsymbol{t}\left(\theta_i, \phi_i\right) + \frac{\sin\left(\alpha_i^*\right)}{\sin\left(\alpha_i\right)} \boldsymbol{t}\left(\theta_{i+1}, \phi_{i+1}\right) \tag{2.7}$$

$$\boldsymbol{p}^* = \boldsymbol{p}_i + \frac{S_i^* f\left(\alpha_i^*\right)}{2} \left[\boldsymbol{t}\left(\theta_i, \phi_i\right) + \boldsymbol{t}_i^*\right] \tag{2.8}$$

Through Eqs. (2.6), (2.7), and (2.8), the continuous well trajectory can be determined. Using the minimum curvature method, the well tangent direction $\boldsymbol{t}$ can be proved to be continuous, as follows:

Proposition: well tangent direction $\boldsymbol{t}$ is continuous

Proof:

In between survey points:

$$\frac{d\boldsymbol{t}_i^*}{dS_i^*} = \frac{\partial \boldsymbol{t}_i^*}{\partial \alpha_i^*} \frac{\partial \alpha_i^*}{\partial S_i^*} = \frac{\alpha_i}{S_{i,i+1}} \left[-\frac{\cos\left(\alpha_i - \alpha_i^*\right)}{\sin\left(\alpha_i\right)} \boldsymbol{t}\left(\theta_i, \phi_i\right) + \frac{\cos\left(\alpha_i^*\right)}{\sin\left(\alpha_i\right)} \boldsymbol{t}\left(\theta_{i+1}, \phi_{i+1}\right) \right]$$

Therefore, $\boldsymbol{t}$ is differentiable in between survey points, which is a sufficient condition for continuity.

At survey point:

For segment i, we have

$$\alpha_i^* = 0 \rightarrow \boldsymbol{t}_i^* = \boldsymbol{t}\left(\theta_i, \phi_i\right)$$

For segment *i*-1, we have

$$\alpha_{i-1}^* = \alpha_{i-1} \rightarrow \boldsymbol{t}_{i-1}^* = \boldsymbol{t}\left(\theta_i, \phi_i\right)$$

Therefore, $\boldsymbol{t}$ is continuous at survey points.

Done proof, the tangent direction $\boldsymbol{t}$ is continuous everywhere along the well trajectory.

2.2. Local Coordinate

Drilling information can be conveniently manifested and comprehended under the local coordinate. According to the minimum curvature method, the adjacent survey points are assumed to lie on the same arc; therefore, there is a unique unit vector that is perpendicular to this arc. The established local coordinate takes this vector as the binormal direction to determine the coordinate orientation, as illustrated in Figure 2-2.

At nodes j and j+1, the tangent directions $\boldsymbol{t}_j$ and $\boldsymbol{t}_{j+1}$ can be obtained from Eq. (2.7). The binormal direction $\boldsymbol{b}_j$ at node j is perpendicular to $\boldsymbol{t}_j$ and $\boldsymbol{t}_{j+1}$; therefore, it can be determined by

$$\boldsymbol{b}_j = \frac{\boldsymbol{t}_j \times \boldsymbol{t}_{j+1}}{\left\| \boldsymbol{t}_j \times \boldsymbol{t}_{j+1} \right\|_2} = \frac{\boldsymbol{t}_j \times \boldsymbol{t}_{j+1}}{\sin\left(\alpha_j\right)} \tag{2.9}$$

where α_j is the extended angle between nodes j and j+1. The normal direction $\boldsymbol{n}_j$ is perpendicular to tangent direction $\boldsymbol{t}_j$ and binormal direction $\boldsymbol{b}_j$, given by

$$\boldsymbol{n}_j = \boldsymbol{b}_j \times \boldsymbol{t}_j \tag{2.10}$$

where $\boldsymbol{n}_j$ points to the center of the arc connected by nodes j and j+1.

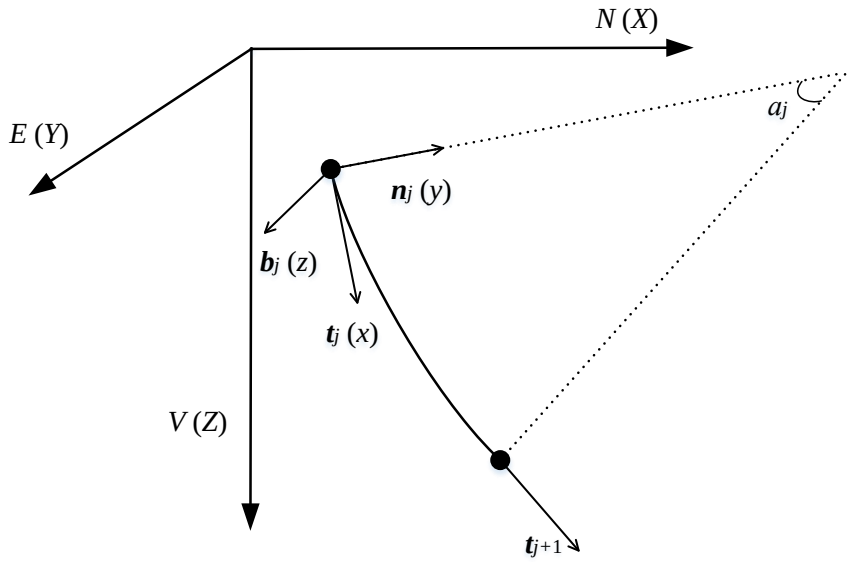

Figure 2-2. Global and local coordinates

Vectors can be transformed from the local coordinate *xyz* to the global coordinate *XYZ* using a three-dimensional rotation matrix $[T_r]^{\mathrm{T}}$ ($[T_r]^{\mathrm{T}} = [T_r]^{-1}$), given by

$$[T_r] = \begin{bmatrix} \cos(x,X) & \cos(x,Y) & \cos(x,Z) \\ \cos(y,X) & \cos(y,Y) & \cos(y,Z) \\ \cos(z,X) & \cos(z,Y) & \cos(z,Z) \end{bmatrix} \tag{2.11}$$

where $\cos(x,X)$ is the cosine between the local x direction and the global X direction, the same is applied to other terms. Defining the north, east, and vertical directions as the global X axis, Y axis, and Z axis and defining the tangent, normal, and binormal directions as the local x axis, y axis, and z axis, $[T_r]$ can be rewritten as

$$[T_r] = \begin{bmatrix} \boldsymbol{t}^{\mathrm{T}} \\ \boldsymbol{n}^{\mathrm{T}} \\ \boldsymbol{b}^{\mathrm{T}} \end{bmatrix} \tag{2.12}$$

where $\boldsymbol{t}^{\mathrm{T}}$, $\boldsymbol{n}^{\mathrm{T}}$, and $\boldsymbol{b}^{\mathrm{T}}$ are the row vectors of $\boldsymbol{t}$, $\boldsymbol{n}$, and $\boldsymbol{b}$, respectively. $[T_r]$ can also be obtained from Rodrigues' formula [76][77] and the third-node method. The latter method determines the orientation of a beam using an additional node outside that beam. The large lateral displacement of directional drill-string makes it possible to find such third node without causing singularity.

2.3. Simulation and Verification

In order to validate the minimum curvature method, a three-dimensional well is created and sampled with an interval of 100 ft. Then the sampled measured depth, inclination, and azimuth are fed into Eqs. (2.1) and (2.8) to obtain the NEV coordinates of the survey points and the continuous well trajectory. The result is illustrated in Figure 2-3.

The deflection of the trajectory obtained by the minimum curvature method from the original trajectory is illustrated in Figure 2-4. This error is very negligible considering the well geometric size. This result verifies the application of the minimum curvature method to generate a continuous well trajectory.

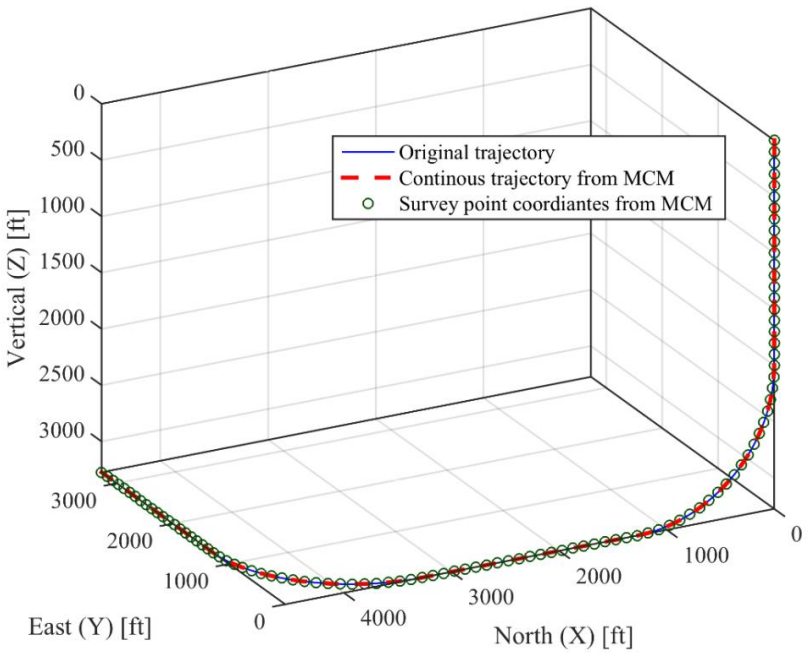

Figure 2-3. Comparison between original trajectory and trajectory calculated from minimum curvature method (MCM)

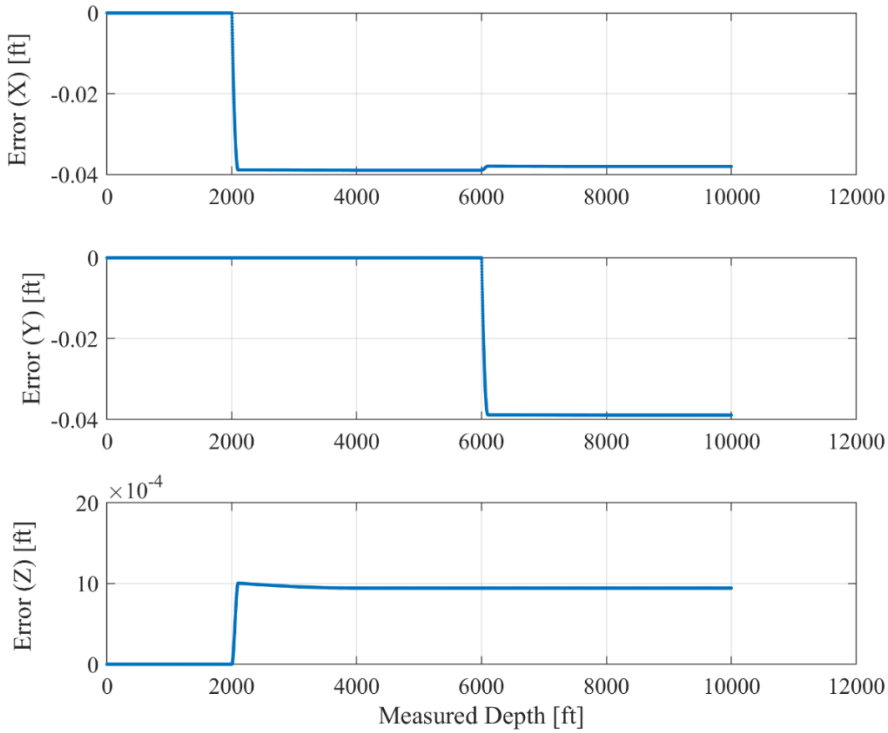

Figure 2-4. Error of the calculated trajectory

For better visualization, a three-view diagram is also provided. Figure 2-5 and Figure 2-6 give an example of a three-dimensional well trajectory obtained using the minimum curvature method and the corresponding three-view diagram. The survey data are provided in Table 2-1.

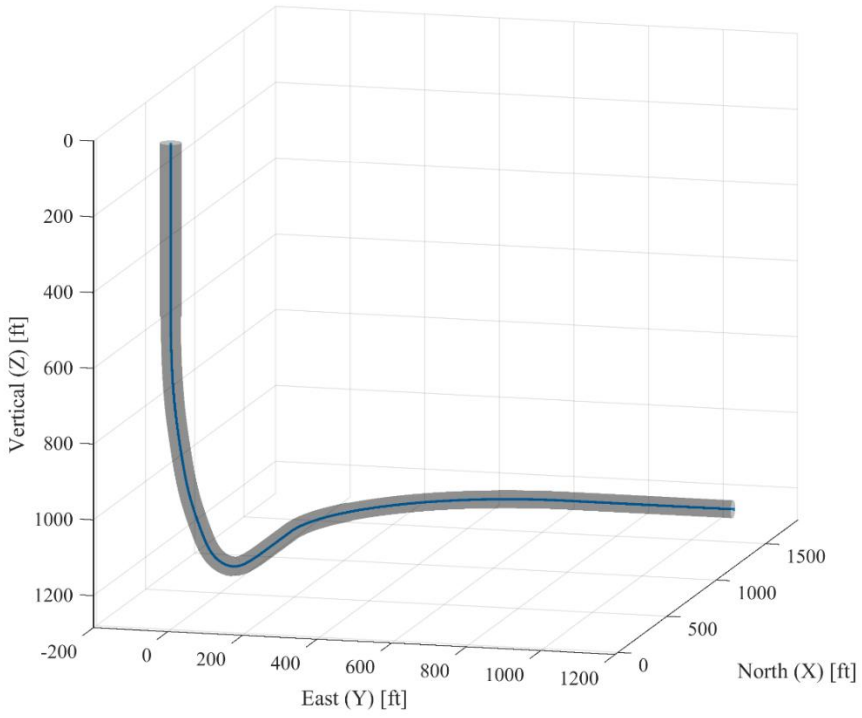

Figure 2-5. Three-dimensional well trajectory

In field, DLS, *build rate* (inclination change per 100 ft), and *walk rate* (azimuth change per 100 ft) are commonly used to interpret well deflecting rate. Using the same survey data, these parameters are calculated against measured depth. The result is illustrated in Figure 2-7.

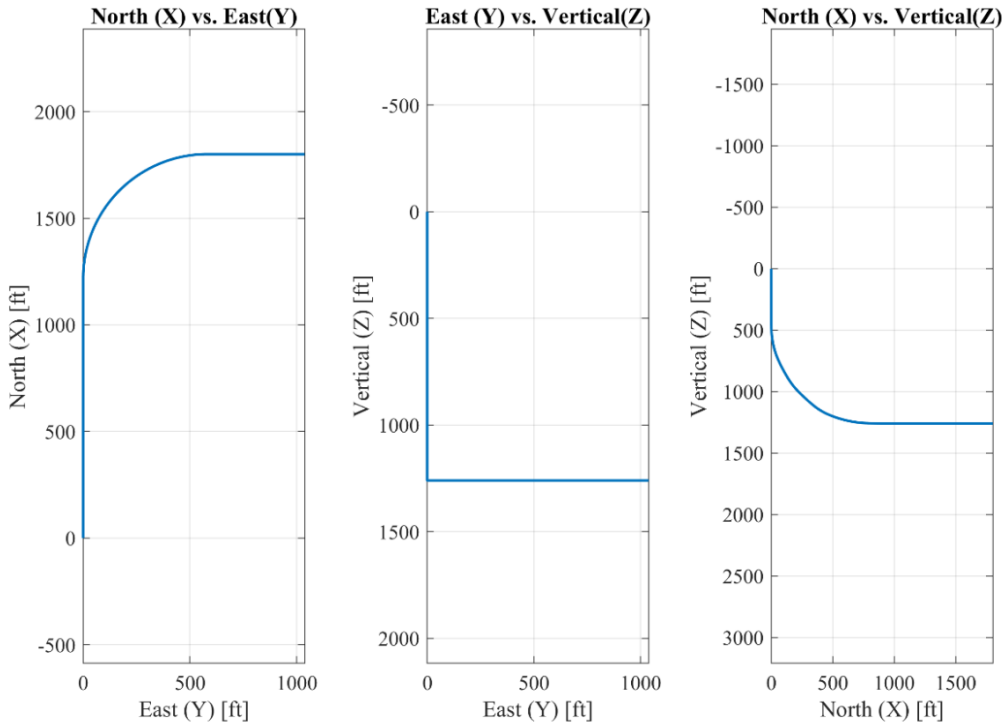

Figure 2-6. Three-view diagram of well trajectory

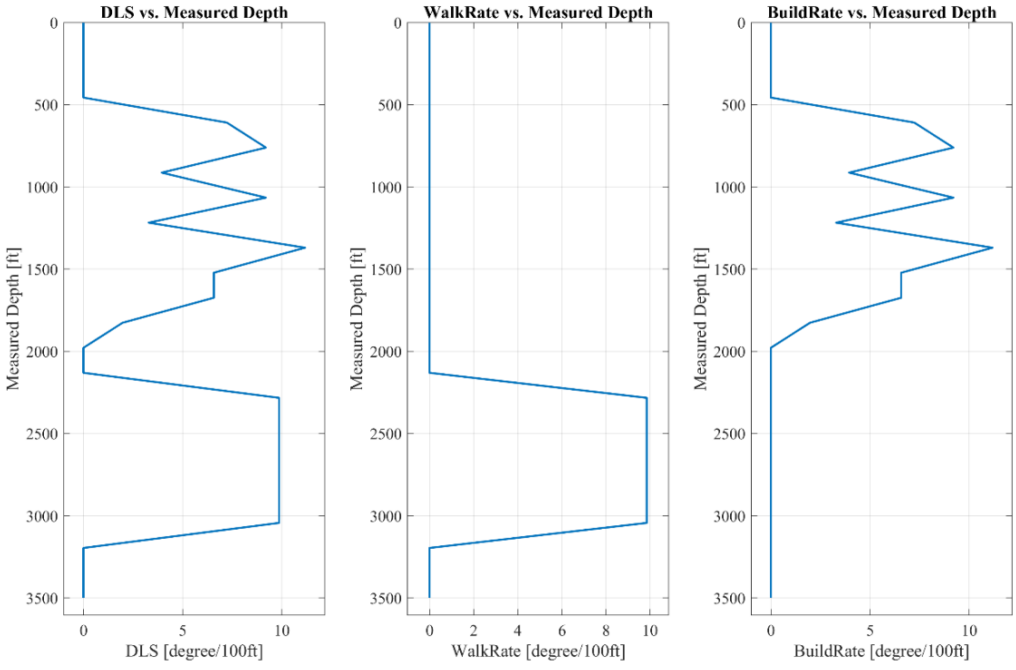

Figure 2-7. DLS, walk rate, and build rate against measured depth

Measured depth [ft]	Inclination [°]	Azimuth [°]	Measured depth [ft]	Inclination [°]	Azimuth [°]
0	0	0	1826	90	0
152	0	0	1978	90	0
304	0	0	2130	90	0
456	0	0	2283	90	15
608	11	0	2435	90	30
760	25	0	2587	90	45
913	31	0	2739	90	60
1065	45	0	2891	90	75
1217	50	0	3044	90	90
1370	67	0	3196	90	90
1522	77	0	3348	90	90
1674	87	0	3500	90	90

Table 2-1. Survey data of the test well

2.4. Summary

Drill-string displacements can be conveniently described with reference to well central axis; therefore, knowing the well trajectory is essential in analyzing drill-string dynamics. However, no such sensor exists that can measure the continuous well trajectory. This chapter discusses the minimum curvature method which can obtain the continuous well trajectory from discrete survey measurements. It is proved that the obtained trajectory is not only continuous but also smooth (derivative is continuous). The simulation results indicate a high accuracy of using the minimum curvature method to get the well trajectory. In addition, the DLS, walk rate, and build rate, which are commonly used by drilling industry to represent well geometries, can be conveniently represented using the minimum curvature method.

Chapter 3. DRILL-STRING FINITE ELEMENT MODEL

The FEM can solve one-dimensional wave equations with high-fidelity, weak-form solutions. Though more computationally intensive, the FEM models can easily incorporate comprehensive boundary conditions and reproduce realistic drilling scenarios. Through meshing along drill-string axial direction, the six DOF dynamics of the entire drill-string can be obtained. In this chapter, three methods are used to develop the dynamic FEM models, in which Section 3.1 implements the Lagrangian method to develop a dynamic FEM equation for vertical drilling; Section 3.2 develops a dynamic model for directional drilling using the principle of virtual work; and Section 3.3 models directional drilling dynamic based on the curved beam theorem, where the assumed strain field method is applied for finite element approximation. Considering the length-to-thickness ratio of a drill-string is very high, the Euler-Bernoulli beam, which neglects the shear deformations, can accurately model drill-string mechanics and is used throughout this chapter.

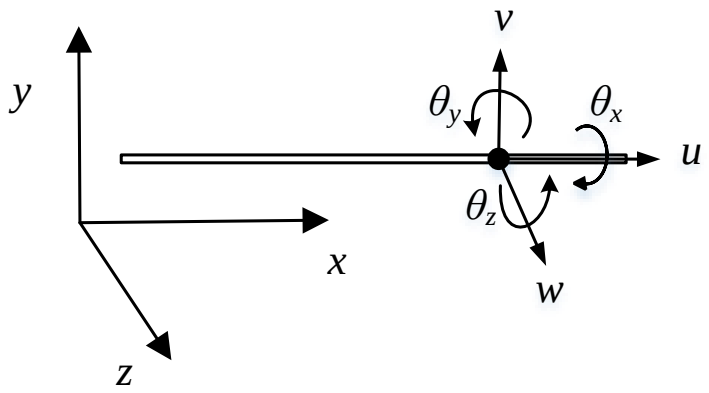

Figure 3-1. Straight Euler-Bernoulli beam

Part of this chapter was published in: 1. Feng, T., et al. "A Finite Element Method with Full Bit-Force Modeling to Analyze Drillstring Vibration." *Journal of Dynamic Systems, Measurement, and Control* 139.9 (2017): 091016; 2. Feng, T., et. al. "Dynamic Modeling of Directional Drillstring: A Linearized Model Considering Well Profile." *Journal of Dynamic Systems, Measurement, and Contro*l 140.6 (2018): 061005; 3. Feng, T., Bakshi, S. Gu, Q. Chen, D. "A Finite Element Modeling Framework for Curved Beam Dynamics Considering Nonlinearities and Contacts". *Journal of Computational and Nonlinear Dynamics*. doi: 10.1115/1.4043452.
The author contributes to develop the finite element model for drill-string

Figure 3-1 illustrates a straight Euler-Bernoulli beam. The bending angles yield:

$$\theta_y = -\frac{dw}{dx} \tag{3.1}$$

$$\theta_z = \frac{dv}{dx} \tag{3.2}$$

where θ_y and θ_z are bending angles around y and z axes, respectively. The strain-displacement relations yield:

$$\varepsilon_x = \frac{du}{dx} + \frac{1}{2}\left(\frac{du}{dx}\right)^2 + \frac{1}{2}\left(\frac{dv}{dx}\right)^2 + \frac{1}{2}\left(\frac{dw}{dx}\right)^2 \tag{3.3}$$

$$\tau_x = \frac{d\theta_x}{dx} \tag{3.4}$$

$$\kappa_y = \frac{d\theta_y}{dx} \tag{3.5}$$

$$\kappa_z = \frac{d\theta_z}{dx} \tag{3.6}$$

where ε_x is the axial strain; κ_y and κ_z are bending curvatures in x and y directions, respectively; and τ_x is the shear strain caused by beam twist.

To obtain the dynamic equation for the entire system, the drill-string is firstly meshed along axial direction. For each element, a local dynamic equation is established. Finally, the system dynamic equation is obtained by combing all local elements under the

global coordinate. The interactions between drill-string and wellbore as well as the interactions between bit and wellbore are applied as boundary condition.

3.1. Lagrangian Method

3.1.1. Drill-string Discretization and Beam Element

Figure 3-2 illustrates the meshing scheme and beam element of a vertical drill-string.

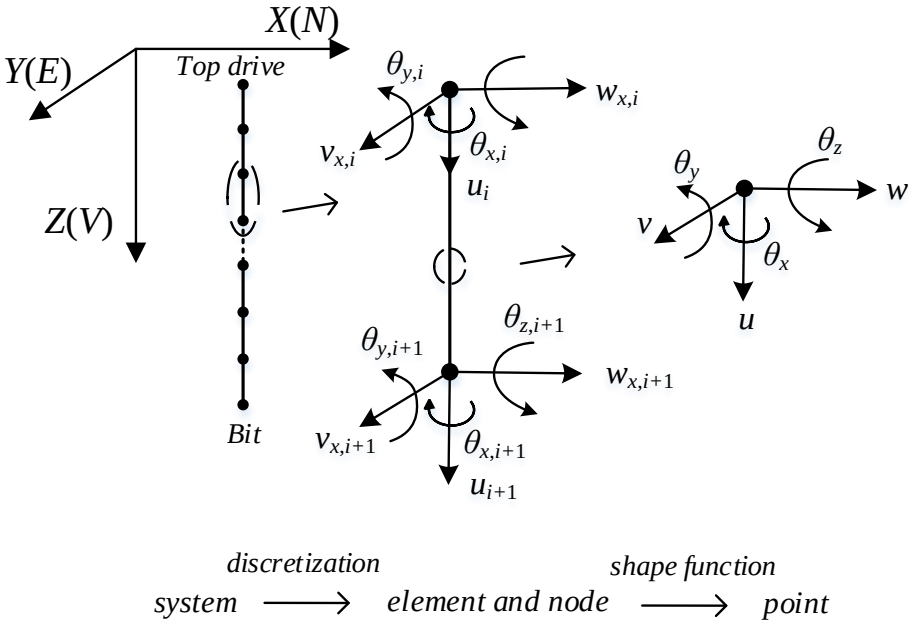

Figure 3-2. Vertical drill-string finite element discretization and beam element

As illustrated in Figure 3-2, the position of each element is determined by two adjacent nodes with six DOF per node. Accordingly, twelve parameters are needed to describe the element displacement vector $\boldsymbol{u_e}$, given by

$$\boldsymbol{u_e} = \begin{bmatrix} u_i & v_i & w_i & \theta_{x,i} & \theta_{y,i} & \theta_{z,i} & u_{i+1} & v_{i+1} & w_i & \theta_{x,i+1} & \theta_{x,i+1} & \theta_{x,i+1} \end{bmatrix}^{\mathrm{T}} \qquad (3.7)$$

where $[\cdot]^{\mathrm{T}}$ is matrix transpose; u_i, v_i, and w_i represent the displacements of node i along local x_i, y_i, and z_i directions, respectively; $\theta_{x,i}$, $\theta_{y,i}$, and $\theta_{z,i}$ represent the local rotations of node i along x_i, y_i, and z_i axes, respectively. Using shape function matrix $[N]^{\mathrm{T}}$ (dimension 6×12), displacement vector $\boldsymbol{u}$, equals to $\left[u\ v\ w\ \theta_x\ \theta_y\ \theta_z\right]^{\mathrm{T}}$, can be determined using

$$\boldsymbol{u} = \left[N\right]^{\mathrm{T}} \boldsymbol{u_e} = \begin{bmatrix} \boldsymbol{N_u} & \boldsymbol{N_v} & \boldsymbol{N_w} & \boldsymbol{N_{\theta x}} & \boldsymbol{N_{\theta y}} & \boldsymbol{N_{\theta z}} \end{bmatrix}^{\mathrm{T}} \boldsymbol{u_e} \tag{3.8}$$

where $\boldsymbol{N_u}$, $\boldsymbol{N_v}$, $\boldsymbol{N_w}$, $\boldsymbol{N_{\theta_x}}$, $\boldsymbol{N_{\theta_y}}$, and $\boldsymbol{N_{\theta_z}}$ are vectors composed by shape functions. Because the highest order of the governing partial differential equations is second order (to describe the bending dynamics), a cubic polynomial Hermite interpolation is used to construct the shape function matrix.

3.1.2. Stiffness Matrix

The local dynamic equation is derived with the extended Hamilton's principle, given by

$$\delta \int_{t_1}^{t_2} \left(V - T - W\right) dt = 0 \tag{3.9}$$

where V is the strain energy; T is the kinetic energy; and W is the work done by external force. The stiffness matrix is derived from strain energy manipulation. The strain energy of a Euler-Bernoulli beam yields:

$$
\begin{aligned}
V &= \frac{1}{2}\int_0^{l_e}\left[\boldsymbol{\varepsilon}^{\mathrm{T}}\mathrm{diag}\left(\begin{bmatrix} EA & GI_\rho & EI & EI \end{bmatrix}\right)\boldsymbol{\varepsilon}\right]dx \\
&= \int_0^{l_e}\left(\frac{EA}{2}\varepsilon_x^2 + \frac{GI_\rho}{2}\tau_x^2 + \frac{EI}{2}\kappa_y^2 + \frac{EI}{2}\kappa_z^2\right)dx
\end{aligned}
\tag{3.10}
$$

where $\boldsymbol{\varepsilon}$, equals to $\begin{bmatrix}\varepsilon_x & \tau_x & \kappa_y & \kappa_z\end{bmatrix}^{\mathrm{T}}$, is the strain vector; $\boldsymbol{f_{int}}$ is the internal force vector; l_e is the length of the element; E is the Young's modulus of the material; G is the shear modulus; A is the cross-sectional area; I is the bending moment; I_ρ is the torsional moment; ε_x, τ_x, κ_y and κ_z are given in Eqs. (3.3) through (3.6). The first term of the right side is the axial strain energy, the second term is the torsional strain energy and the last two terms are the bending strain energy. The shear deformation is ignored according to Euler-Bernoulli beam assumption.

Substituting Eq. (3.8) into Eq. (3.10), the partial derivative of the strain energy V with respect to $\boldsymbol{u_e}$ is given by

$$
\begin{aligned}
\frac{\partial V}{\partial \boldsymbol{u_e}} &= \int_0^{l_e}\left[\left(EA\boldsymbol{N}_{\boldsymbol{u}}'\boldsymbol{N}_{\boldsymbol{u}}'^{\mathrm{T}} + GI_\rho\boldsymbol{N}_{\theta_x}'\boldsymbol{N}_{\theta_x}'^{\mathrm{T}} + EI\boldsymbol{N}_{\theta_y}'\boldsymbol{N}_{\theta_y}'^{\mathrm{T}} + EI\boldsymbol{N}_{\theta_z}'\boldsymbol{N}_{\theta_z}'^{\mathrm{T}}\right)\boldsymbol{u_e}\right]dx \\
&\quad + F_x\int_0^{l_e}\left[\left(\boldsymbol{N}_{\boldsymbol{u}}'\boldsymbol{N}_{\boldsymbol{u}}'^{\mathrm{T}} + \boldsymbol{N}_{\boldsymbol{v}}'\boldsymbol{N}_{\boldsymbol{v}}'^{\mathrm{T}} + \boldsymbol{N}_{\boldsymbol{w}}'\boldsymbol{N}_{\boldsymbol{w}}'^{\mathrm{T}}\right)\boldsymbol{u_e}\right]dx
\end{aligned}
\tag{3.11}
$$

where $[\cdot]'$is the derivative with respect to x; F_x is the axial internal force of the element. The first term of Eq. (3.11) is linear with displacement $\boldsymbol{u_e}$. The coefficient matrix is therefore the linear stiffness matrix $\left[k_{e,l}\right]$, where

$$
\left[k_{e,l}\right] = \int_0^{l_e}\left(EA\boldsymbol{N}_{\boldsymbol{u}}'\boldsymbol{N}_{\boldsymbol{u}}'^{\mathrm{T}} + GI_\rho\boldsymbol{N}_{\theta_x}'\boldsymbol{N}_{\theta_x}'^{\mathrm{T}} + EI\boldsymbol{N}_{\theta_y}'\boldsymbol{N}_{\theta_y}'^{\mathrm{T}} + EI\boldsymbol{N}_{\theta_z}'\boldsymbol{N}_{\theta_z}'^{\mathrm{T}}\right)dx \tag{3.12}
$$

The second term of Eq. (3.11) is dependent on beam axial internal force F_x. The corresponding nonlinear stiffness matrix $\left[k_{e,n}\right]$ is given by

$$\left[k_{e,n}\right] = F_x \int_0^{l_e} \left(\boldsymbol{N}_u' \boldsymbol{N}_u'^{\mathrm{T}} + \boldsymbol{N}_v' \boldsymbol{N}_v'^{\mathrm{T}} + \boldsymbol{N}_w' \boldsymbol{N}_w'^{\mathrm{T}} \right) dx \tag{3.13}$$

The final element stiffness matrix $[k_e]$ can be obtained by adding $\left[k_{e,l}\right]$ and $\left[k_{e,n}\right]$:

$$\left[k_e\right] = \left[k_{e,l}\right] + \left[k_{e,n}\right] \tag{3.14}$$

3.1.3. Mass and Damping Matrices

The mass matrix is derived from kinetic energy *T*, which is expressed as

$$\begin{aligned} T &= \frac{1}{2} \int_0^{l_e} \left[\dot{\boldsymbol{u}}^{\mathrm{T}} \mathrm{diag}\left(\begin{bmatrix} \rho A & \rho A & \rho A & \rho I_\rho & 0 & 0 \end{bmatrix} \right) \dot{\boldsymbol{u}} \right] dx \\ &= \int_0^{l_e} \frac{\rho}{2} \left[A\left(\dot{u}^2 + \dot{v}^2 + \dot{w}^2 \right) + I_\rho \dot{\theta}_x^2 \right] dx \end{aligned} \tag{3.15}$$

where $[\dot{\cdot}]$ is the derivative with respect to time; the first three terms of the right side of Eq. (3.15) represent the translational kinetic energy and the fourth term indicates the rotational kinetic energy. The bending kinetic energy is ignored according to Euler-Bernoulli beam assumption. Substituting Eq. (3.8) into Eq. (3.15), the derivative of kinetic energy is given by

$$\frac{d}{dt} \frac{\partial T}{\partial \dot{\boldsymbol{u}}_e} = \int_0^{l_e} \rho \left[A\left(\boldsymbol{N}_u \boldsymbol{N}_u^{\mathrm{T}} + \boldsymbol{N}_v \boldsymbol{N}_v^{\mathrm{T}} + \boldsymbol{N}_w \boldsymbol{N}_w^{\mathrm{T}} \right) + I_\rho \boldsymbol{N}_{\theta_x} \boldsymbol{N}_{\theta_x}^{\mathrm{T}} \right] \ddot{\boldsymbol{u}}_e dx \tag{3.16}$$

Because the derivative of kinetic energy is proportional to acceleration $\ddot{\boldsymbol{u}}_e$, the coefficient of acceleration is the local mass matrix, $[m_e]$, where

$$[m_e] = \int_0^{l_e} \rho \left[A\left(\boldsymbol{N}_u \boldsymbol{N}_u^{\mathrm{T}} + \boldsymbol{N}_v \boldsymbol{N}_v^{\mathrm{T}} + \boldsymbol{N}_w \boldsymbol{N}_w^{\mathrm{T}} \right) + I_\rho \boldsymbol{N}_{\theta_x} \boldsymbol{N}_{\theta_x}^{\mathrm{T}} \right] dx \tag{3.17}$$

Rayleigh damping [78] is applied to obtain the damping matrix $[d_e]$

$$[d_e] = \alpha [k_{e,l}] + \beta [m_e] \tag{3.18}$$

where α and β are given constants. Finally, the local dynamic equation can be rewritten as

$$[k_e]\boldsymbol{u_e} + [d_e]\dot{\boldsymbol{u}}_{\boldsymbol{e}} + [m_e]\ddot{\boldsymbol{u}}_{\boldsymbol{e}} = \boldsymbol{f_e} \tag{3.19}$$

where $\dot{\boldsymbol{u}}_{\boldsymbol{e}}$ and $\ddot{\boldsymbol{u}}_{\boldsymbol{e}}$ are velocity vector and acceleration vector of the beam element, respectively; and $\boldsymbol{f_e}$ is the external force under the local coordinate. This section is published in [26], which can be referred for further study.

3.2. Principle of Virtual Work

In Section 3.1, a dynamic equation is established for vertical drilling using the Lagrangian method. Vertical drilling can be categorized as a small displacement problem in which the geometry nonlinearity can be neglected. However, the displacement of directional drill-string is large where both elastic deformation and rigid body translation and rotation contribute to the final displacement. The common practice to deal with geometry nonlinearity caused by large displacement is through iterative method [79], which is computationally expensive. In this case, the three-dimensional well trajectory is obtained beforehand and the drill-string strain remains small which is up bounded by the

available DLS. Accordingly, a linear form can be kept after eliminating the translational motions.

3.2.1. Drill-string Discretization

Setting well central axis as reference, the directional drill-string is discretized as Figure 3-3, where *X*, *Y*, and *Z* are the axes of the global coordinate. They coincide with the north, east, and vertical directions of the NEV coordinate, respectively; x_i, y_i, and z_i are the axes of the i^{th} local coordinate; *u*, *v*, and *w* are the displacements of a given element point in x_i, y_i, and z_i directions, respectively; θ_x, θ_y, and θ_z are the angular displacements of that point in x_i, y_i, and z_i directions, respectively; $[T_r]$ is the rotation matrix and $[N]^{\text{T}}$ is the shape function matrix defined in Eq. (3.8).

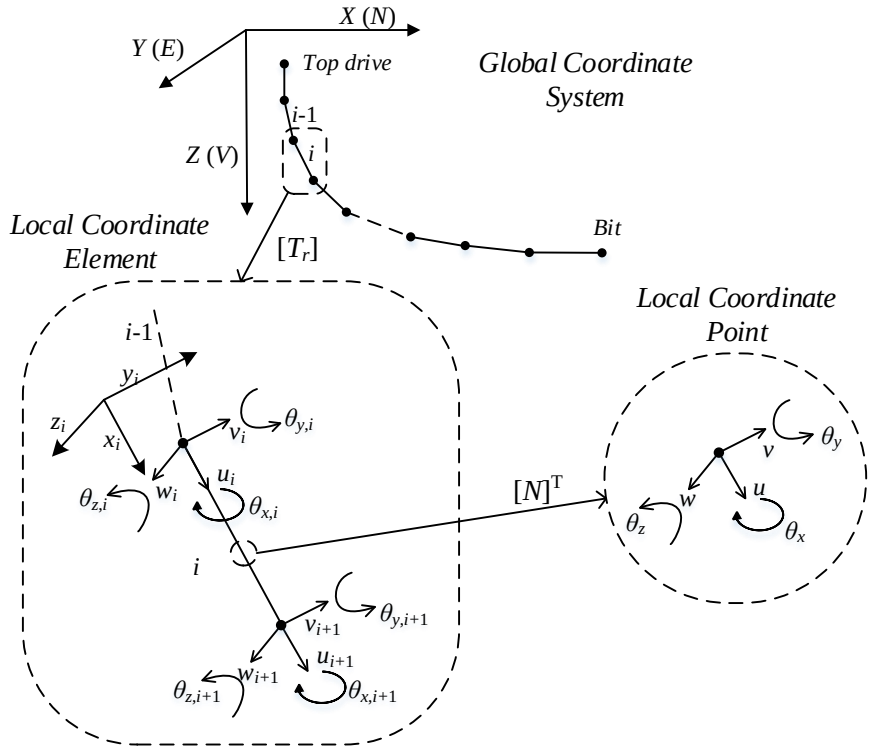

Figure 3-3. Directional drill-string finite element discretization and beam element

3.2.2. Virtual Work of Internal Force

This research assumes that the overall displacement of a drill-string is contributed by two components: an initial displacement from straight state to the position coincident with the central axis of the well and a second displacement within the wellbore wall driven by the unbalanced force [42]. Corresponding to the aforementioned two displacements, the resulted internal force $\boldsymbol{f_{int}}$ can be written as

$$\boldsymbol{f_{int}} = \boldsymbol{f_0} + \boldsymbol{f_1} = \begin{bmatrix} F_x & F_y & F_z & T_{\theta_x} & M_{\theta_y} & M_{\theta_z} \end{bmatrix}^{\mathrm{T}} \tag{3.20}$$

where $\boldsymbol{f}_0$ and $\boldsymbol{f}_1$ are caused by the initial displacement and the second displacement, respectively; F_x is the force in axial direction; F_y and F_z are the shear forces in lateral directions; T_{θ_x} is the torsion in axial direction; and M_{θ_y} and M_{θ_z} are the bending moments. The Euler-Bernoulli beam model includes the effect of shear force; however, no deformation is resulted; therefore, no strain energy is produced. In deriving the governing equations, the shear stresses are set to zero to eliminate the associated strain energy. This manipulation can simplify matrix calculation without influencing the ability of the proposed model to calculate shear forces. For the rest of this section, Eq. (3.21) is applied to represent the internal force

$$\boldsymbol{f_{int}} = \boldsymbol{f_0} + \boldsymbol{f_1} = \begin{bmatrix} F_x & T_{\theta_x} & M_{\theta_y} & M_{\theta_z} \end{bmatrix}^{\mathrm{T}} \tag{3.21}$$

The second displacement $\boldsymbol{u}$ is with respect to well central axis and can be represented as

$$\boldsymbol{u} = \begin{bmatrix} u & v & w & \theta_x & \theta_y & \theta_z \end{bmatrix}^{\mathrm{T}} \tag{3.22}$$

where each component of $\boldsymbol{u}$ is defined in Figure 3-3. $\boldsymbol{u}$ is a small displacement and obeys Eqs. (3.1) through (3.6). The internal force caused by $\boldsymbol{u}$ yields:

$$\boldsymbol{f_1} = \mathrm{diag}\left(\begin{bmatrix} EA & GI_\rho & EI & EI \end{bmatrix}\right)\boldsymbol{\varepsilon} \tag{3.23}$$

where $\boldsymbol{\varepsilon}$, equals to $\begin{bmatrix}\varepsilon_x & \tau_x & \kappa_y & \kappa_z\end{bmatrix}^{\mathrm{T}}$, is the strain vector. Assuming a drill-string element in dynamic equilibrium is subject to a small virtual displacement $\delta\boldsymbol{u}$, the virtual work W_{int} done by internal force is given by

$$W_{int} = \int_0^{l_e}\left(\delta\boldsymbol{\varepsilon}^{\mathrm{T}}\,\boldsymbol{f_{int}}\right)dx = \int_0^{l_e}\left(\delta\boldsymbol{\varepsilon}^{\mathrm{T}}\,\boldsymbol{f}_0\right)dx + \int_0^{l_e}\left(\delta\boldsymbol{\varepsilon}^{\mathrm{T}}\,\boldsymbol{f}_1\right)dx \tag{3.24}$$

The high order terms are ignored to calculate the virtual work done by $\boldsymbol{f_0}$, where

$$\int_0^{l_e}\left(\delta\boldsymbol{\varepsilon}^{\mathrm{T}}\,\boldsymbol{f_0}\right)dx = \delta\boldsymbol{u_e}^{\mathrm{T}}\int_0^{l_e}\left(\left[N\right]'\,\boldsymbol{f_0}\right)dx \tag{3.25}$$

$$\boldsymbol{f_0} = \mathrm{diag}\left(\begin{bmatrix} EA & GI_\rho & EI & EI \end{bmatrix}\right)\boldsymbol{\varepsilon_0} \tag{3.26}$$

Substituting Eq. (3.8) into Eq. (3.23), the virtual work done by $\boldsymbol{f_1}$ can be expressed as

$$\begin{aligned}\int_0^{l_e}\left(\delta\boldsymbol{\varepsilon}^{\mathrm{T}}\,\boldsymbol{f}_1\right)dx = \delta\boldsymbol{u_e}^{\mathrm{T}}\int_0^{l_e}\left[\left(EA\boldsymbol{N}_{\boldsymbol{u}}'\boldsymbol{N}_{\boldsymbol{u}}'^{\mathrm{T}} + GI_\rho\boldsymbol{N}_{\boldsymbol{\theta}_x}'\boldsymbol{N}_{\boldsymbol{\theta}_x}'^{\mathrm{T}} + EI\boldsymbol{N}_{\boldsymbol{\theta}_y}'\boldsymbol{N}_{\boldsymbol{\theta}_y}'^{\mathrm{T}} + EI\boldsymbol{N}_{\boldsymbol{\theta}_z}'\boldsymbol{N}_{\boldsymbol{\theta}_z}'^{\mathrm{T}}\right)\boldsymbol{u_e}\right]dx \\ + \delta\boldsymbol{u_e}^{\mathrm{T}}F_x\int_0^{l_e}\left[\left(\boldsymbol{N}_{\boldsymbol{u}}'\boldsymbol{N}_{\boldsymbol{u}}'^{\mathrm{T}} + \boldsymbol{N}_{\boldsymbol{v}}'\boldsymbol{N}_{\boldsymbol{v}}'^{\mathrm{T}} + \boldsymbol{N}_{\boldsymbol{w}}'\boldsymbol{N}_{\boldsymbol{w}}'^{\mathrm{T}}\right)\boldsymbol{u_e}\right]dx\end{aligned} \tag{3.27}$$

where F_x is the axial internal force of the element.

3.2.3. Virtual Work of External Force

The inertial force $\boldsymbol{f_{ine}}$ is considered when calculating the external force; therefore, the virtual work of the general external force can be expressed as

$$\begin{aligned} W_{ext} &= \int_0^{l_e} \delta \boldsymbol{u}^{\mathrm{T}} \left(\boldsymbol{f_{ext}} - \boldsymbol{f_{ine}} \right) dx = \int_0^{l_e} \left(\delta \boldsymbol{u}^{\mathrm{T}} \boldsymbol{f_{ext}} \right) dx - \int_0^{l_e} \left(\delta \boldsymbol{u}^{\mathrm{T}} [\mathrm{P}] \ddot{\boldsymbol{u}} \right) dx \\ &= \delta \boldsymbol{u_e}^{\mathrm{T}} \int_0^{l_e} \left([N] \boldsymbol{f_{ext}} \right) dx - \delta \boldsymbol{u_e}^{\mathrm{T}} \left(\int_0^{l_e} \left([N][\mathrm{P}][N]^{\mathrm{T}} \right) dx \right) \ddot{\boldsymbol{u}}_{\boldsymbol{e}} \end{aligned} \tag{3.28}$$

$$[\mathrm{P}] = \mathrm{diag}\left(\begin{bmatrix} \rho A & \rho A & \rho A & \rho I_\rho & 0 & 0 \end{bmatrix} \right) \tag{3.29}$$

where $\boldsymbol{f_{ext}}$ is the distribution of external force (if an external force $\boldsymbol{f_c}$ is centralized, its distribution is $\boldsymbol{f_c}(x)\delta(x)$ where $\delta(x)$ is the Dirac delta function) and ρ is the body density of the material. The bending kinetic energy is ignored according to Euler-Bernoulli beam assumption.

3.2.4. Dynamic Equation

According to the principle of virtual work, the virtual work of external force W_{ext} is equal to the virtual work of internal force W_{int}. Dividing $\delta \boldsymbol{u_e}^{\mathrm{T}}$ from the right side of Eqs. (3.24) and (3.28) produces

$$\left(\begin{bmatrix} k_{e,l} \end{bmatrix} + \begin{bmatrix} k_{e,n} \end{bmatrix} \right) \boldsymbol{u_e} + \begin{bmatrix} m_e \end{bmatrix} \ddot{\boldsymbol{u}}_{\boldsymbol{e}} = \boldsymbol{f_e} - \boldsymbol{r_e} \tag{3.30}$$

with

$$\begin{bmatrix} k_{e,l} \end{bmatrix} = \int_0^{l_e} \left(EA \boldsymbol{N}'_{\boldsymbol{u}} \boldsymbol{N}'^{\mathrm{T}}_{\boldsymbol{u}} + GI_\rho \boldsymbol{N}'_{\boldsymbol{\theta}_x} \boldsymbol{N}'^{\mathrm{T}}_{\boldsymbol{\theta}_x} + EI \boldsymbol{N}'_{\boldsymbol{\theta}_y} \boldsymbol{N}'^{\mathrm{T}}_{\boldsymbol{\theta}_y} + EI \boldsymbol{N}'_{\boldsymbol{\theta}_z} \boldsymbol{N}'^{\mathrm{T}}_{\boldsymbol{\theta}_z} \right) dx \tag{3.31}$$

$$\left[k_{e,n}\right] = F_x \int_0^{l_e} \left(\boldsymbol{N}_{\boldsymbol{u}}' \boldsymbol{N}_{\boldsymbol{u}}'^{\mathrm{T}} + \boldsymbol{N}_{\boldsymbol{v}}' \boldsymbol{N}_{\boldsymbol{v}}'^{\mathrm{T}} + \boldsymbol{N}_{\boldsymbol{w}}' \boldsymbol{N}_{\boldsymbol{w}}'^{\mathrm{T}} \right) dx \tag{3.32}$$

$$\left[m_e\right] = \int_0^{l_e} \left(\left[N\right]\left[\mathrm{P}\right]\left[N\right]^{\mathrm{T}} \right) dx \tag{3.33}$$

$$\boldsymbol{f_e} = \int_0^{l_e} \left(\left[N\right] \boldsymbol{f_{ext}} \right) dx \tag{3.34}$$

$$\boldsymbol{r_e} = \int_0^{l_e} \left(\left[N\right]' \boldsymbol{f_0} \right) dx \tag{3.35}$$

where $\boldsymbol{f_e}$ is the equivalent nodal force of external excitation and $\boldsymbol{r_e}$ is the equivalent nodal force of initial displacement; $\left[k_{e,l}\right]$, $\left[k_{e,n}\right]$, and $[m_e]$ hold the same formulation as Eqs. (3.12), (3.13), and (3.17). Similar to Eq. (3.18), a Rayleigh damping is added to stabilize the dynamic system and Eq. (3.30) is transformed to

$$\left(\left[k_{e,l}\right] + \left[k_{e,n}\right]\right)\boldsymbol{u_e} + \left[d_e\right]\dot{\boldsymbol{u}}_{\boldsymbol{e}} + \left[m_e\right]\ddot{\boldsymbol{u}}_{\boldsymbol{e}} = \boldsymbol{f_e} - \boldsymbol{r}_e \tag{3.36}$$

Based on the preceding analysis, a dynamic equation is established for the beam element where the large displacement occurring during directional drilling is taken into consideration. This section is published in [80], which can be referred for further study.

3.3. Assumed Strain Field Method

Based on the review in Section 1.4, a variety of FEM models have been proposed to analyze the static and dynamic responses of drilling tools. In Sections 3.1 and 3.2, FEM equations are also established for drilling dynamics. The above approaches use straight beam elements to approximate the drill-pipe and BHA. This approximation

works well for quasi-vertical wells even with limited element numbers. However, when it comes to unconventional drilling where large curvature occurs, it will require fine-grid meshing to obtain an accurate approximation. In order to improve the modeling accuracy with fewer elements and computational cost, the curved beam element is investigated to model directional drilling. Based on the assumption of the minimum curvature method, the directional well trajectory is connected by circular arcs. Accordingly, meshing the curved drill-string with curved beam elements can also contribute to eliminate the discretization error.

According to Section 3.2, formulating directional drilling dynamics is converted into a small displacement problem by linearizing the system dynamics around the well central axis. Under the assumption of small displacements, this section derives a finite element based on the curved Euler-Bernoulli beam and the assumed strain field method is applied to obtain the shape functions, which provides better performance than conventional polynomial functions [81][82]. Compared to the geometrically exact beam [83][84], the Euler-Bernoulli beam (also the Timoshenko beam) is more efficient for small displacement problems since the finite rotations can be ignored. The numerical discretization and the implementation of Euler-Bernoulli beam elements (also the Timoshenko beam elements) are also more straightforward [85]. Compared to existing elements [86]-[90], the developed finite element is more generic as it analyzes both in-plane and out-of-plane dynamics of curved beams. In addition, the nonlinear geometric stiffness is derived, which enables the stability analysis of compressed curved structures.

Integrating the geometric stiffness, the contact model and the numerical method with the curved beam element, the post-buckling behavior of curved structures can be predicted.

3.3.1. Curved Beam Theorem

Figure 3-4 illustrates a curved beam element, where *u*, *v*, and *w* are nodal displacements in local *x*, *y*, and *z* directions, respectively; θ_x, θ_y, and θ_z are rotations in *x*, *y*, and *z* directions, respectively; *R* is the radius of the curve; *s* denotes the curved beam length; φ, equals to s/R, is the extended angle.

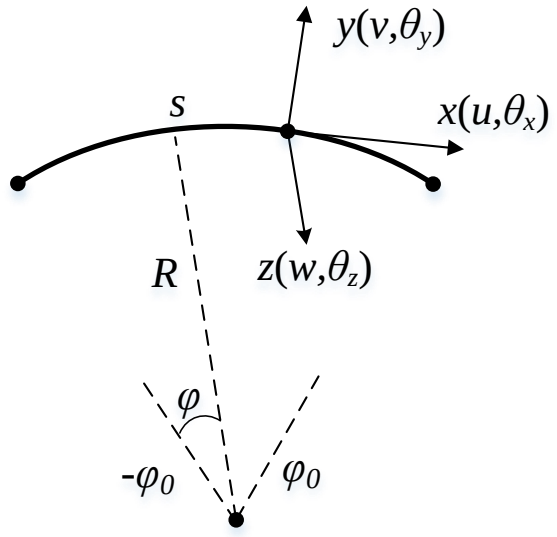

Figure 3-4. Curved Euler-Bernoulli beam

Since the length-to-thickness ratio of the drill-string is very high, the Euler-Bernoulli beam assumption is applied, where the in-plane and out-plane bending angles yield:

$$\theta_y = -\frac{dw}{ds} \tag{3.37}$$

$$\theta_z = \frac{dv}{ds} - \frac{u}{R} \tag{3.38}$$

The strain-displacement relations yield:

$$\varepsilon_{x,l} = \frac{du}{ds} + \frac{v}{R} \tag{3.39}$$

$$\kappa_y = \frac{d\theta_y}{ds} - \frac{\theta_x}{R} \tag{3.40}$$

$$\kappa_z = \frac{d\theta_z}{ds} \tag{3.41}$$

$$\tau_x = \frac{d\theta_x}{ds} + \frac{\theta_y}{R} \tag{3.42}$$

where $\varepsilon_{x,l}$ is the axial strain considering only the linear terms; κ_y and κ_z are the out-of-plane and in-plane bending curvatures; and τ_x is the torsional shear strain. The higher order terms of the axial strain will be discussed later in Section 3.3.3.

3.3.2. Curved Beam Finite Element

The assumed strain field method is applied to obtain the shape functions. In [91], a constant strain and constant curvature field, and a constant strain and linear curvature field are applied to develop the curved beam elements. It is seen that the constant strain and linear curvature field generates a more accurate result, whereas a higher order strain field can lead to singularity of the shape functions. Therefore, a constant strain and linear curvature field is assumed in this paper, where the axial strain $\varepsilon_{x,l}$ and torsional shear

strain τ_x are constant, and the bending curvatures κ_y and κ_z change linearly with φ, given by

$$\varepsilon_{x,l} = a_4 + a_5 \tag{3.43}$$

$$\tau_x = b_6 \tag{3.44}$$

$$\kappa_y = Rb_4\varphi + b_5 \tag{3.45}$$

$$\kappa_z = -a_6\varphi/R - a_5/R \tag{3.46}$$

where a_4, a_5, a_6, b_4, b_5, and b_6 are constant coefficients. Substituting Eqs.(3.37), (3.38) and (3.43)-(3.46) into Eqs. (3.39)-(3.42) and replacing s with $R\varphi$, we have

$$\begin{cases} \dfrac{du}{Rd\varphi} + \dfrac{v}{R} = a_4 + a_5 \\ \dfrac{d\theta_x}{Rd\varphi} - \dfrac{dw}{R^2 d\varphi} = b_6 \\ -\dfrac{d^2 w}{R^2 d\varphi^2} - \dfrac{\theta_x}{R} = Rb_4\varphi + b_5 \\ \dfrac{d^2 v}{Rd\varphi^2} - \dfrac{du}{Rd\varphi} = -a_6\varphi - a_5 \end{cases} \tag{3.47}$$

Solving the ordinary differential equations with respect to φ in Eq. (3.47), the displacements and rotations can be represented as

$$\boldsymbol{u} = \left[A(\varphi) \right] \boldsymbol{a} \tag{3.48}$$

$$\left[A(\varphi)\right] =$$

$$\begin{bmatrix} -R\sin(\varphi) & R\cos(\varphi) & R & 0 & R\varphi & \frac{R\varphi^2}{2} & 0 & 0 & 0 & 0 & 0 & 0 \\ R\cos(\varphi) & R\sin(\varphi) & 0 & R & 0 & -R\varphi & 0 & 0 & 0 & 0 & 0 & 0 \\ 0 & 0 & 0 & 0 & 0 & 0 & -R\sin(\varphi) & R\cos(\varphi) & 1 & -R^3\varphi & 0 & -R^2\varphi \\ 0 & 0 & 0 & 0 & 0 & 0 & -\sin(\varphi) & \cos(\varphi) & 0 & -R^2\varphi & -R & 0 \\ 0 & 0 & 0 & 0 & 0 & 0 & \cos(\varphi) & \sin(\varphi) & 0 & R^2 & 0 & R \\ 0 & 0 & -1 & 0 & -\varphi & -1-\frac{\varphi^2}{2} & 0 & 0 & 0 & 0 & 0 & 0 \end{bmatrix} \tag{3.49}$$

$$\boldsymbol{a} = \begin{bmatrix} a_1 & a_2 & a_3 & a_4 & a_5 & a_6 & b_1 & b_2 & b_3 & b_4 & b_5 & b_6 \end{bmatrix}^{\mathrm{T}} \tag{3.50}$$

where a_1, a_2, a_3, b_1, b_2, and b_3 are constant coefficients, derived by solving Eq. (3.47). The assumed strain field is chosen according to Eqs. (3.43)-(3.46) so that the obtained coefficient matrix $[A(\varphi)]$ has consistent units. Eq. (3.48) holds everywhere within that element including the two end points. Assuming the curved beam element ranges from $-\varphi_0$ to φ_0 as illustrated in Figure 3-4, the end node displacements can be written as

$$\begin{bmatrix} \boldsymbol{u}_{\boldsymbol{e},1} \\ \boldsymbol{u}_{\boldsymbol{e},2} \end{bmatrix} = \begin{bmatrix} A(-\varphi_0) \\ A(\varphi_0) \end{bmatrix} \boldsymbol{a} \tag{3.51}$$

where $\boldsymbol{u}_{\boldsymbol{e},1}$ and $\boldsymbol{u}_{\boldsymbol{e},2}$ are displacement vectors at two end nodes. Combining Eq. (3.48) and Eq. (3.51), the shape function $[N_c]$ for curved beam element can be obtained

$$\boldsymbol{u} = \left[N_c\right]\boldsymbol{u}_{\boldsymbol{e}} = \left[A(\varphi)\right] \begin{bmatrix} A(-\varphi_0) \\ A(\varphi_0) \end{bmatrix}^{-1} \begin{bmatrix} \boldsymbol{u}_{\boldsymbol{e},1} \\ \boldsymbol{u}_{\boldsymbol{e},2} \end{bmatrix} \tag{3.52}$$

with

$$\left[N_c\right]=\left[A(\varphi)\right]\begin{bmatrix}A(-\varphi_0)\\A(\varphi_0)\end{bmatrix}^{-1} \tag{3.53}$$

In Eq. (3.53), the shape function $[N_c]$ becomes singular in the case of straight beam element; therefore, using curved beam element only is not sufficient to model the whole directional drill-string. In this research, a hybrid model which integrates the curved beam element and the straight beam element is applied for drilling dynamics calculation.

Substituting Eq. (3.54) into Eqs. (3.55)-(3.56), the element strain vector $\boldsymbol{\varepsilon}$ can be obtained as

$$\boldsymbol{\varepsilon}=\begin{bmatrix}\varepsilon_{x,l} & \kappa_z & \tau_x & \kappa_y\end{bmatrix}^{\mathrm{T}}=\left[B(\varphi)\right]\boldsymbol{u_e} \tag{3.57}$$

where

$$\left[B(\varphi)\right]=\begin{bmatrix}0&0&0&1&1&0&0&0&0&0&0&0\\0&0&0&0&-\frac{1}{R}&-\frac{\varphi}{R}&0&0&0&0&0&0\\0&0&0&0&0&0&0&0&0&0&0&1\\0&0&0&0&0&0&0&0&0&R\varphi&1&0\end{bmatrix}\begin{bmatrix}\left[A(-\varphi_0)\right]\\\left[A(\varphi_0)\right]\end{bmatrix}^{-1} \tag{3.58}$$

With $[N_c]$ and $[B(\varphi)]$ as defined earlier, the stiffness and mass matrices can be derived using the Lagrangian method. The linear stiffness matrix $\left[k_{l,e}\right]$ of the curved beam element is given by

$$\left[k_{l,e}\right]=\int_{-\varphi_0}^{\varphi_0}\left[B(\varphi)\right]^{\mathrm{T}}\left[\Lambda_E\right]\left[B(\varphi)\right]Rd\varphi \tag{3.59}$$

where $[\Lambda_E]$ is equal to $\mathrm{diag}\left(\left[EA\ \ EI\ \ GI_\rho\ \ EI\right]\right)$, E is the Young's modulus, G is the shear modulus, I is the second moment of area in the flexural direction, and I_ρ is the second

moment of area in torsional direction. The mass matrix $[m_e]$ of the curved beam element is given by

$$[m_e] = \int_{-\varphi_0}^{\varphi_0} [N_c(\varphi)]^{\mathrm{T}} [\Lambda_\rho] [N_c(\varphi)] R d\varphi \tag{3.60}$$

where $[\Lambda_\rho]$ is equal to diag$([\rho A \;\; \rho A \;\; \rho A \;\; \rho I_\rho \;\; \rho I \;\; \rho I])$, and ρ is the material density. The Rayleigh damping is applied to get the damping matrix $[d_e]$.

3.3.3. Geometric Stiffness Matrix of Curved Beam

In most cases, the linear stiffness matrix is sufficient for both static and dynamic analyses. However, when the beam is under a compression force that is larger than its buckling threshold, the effect of higher order terms becomes significant, and should be included in the stiffness matrix. Considering the effect of second order terms, the axial strain of a curved beam yields

$$\varepsilon_x = \varepsilon_{x,l} + \varepsilon_{x,n} = \frac{du}{ds} + \frac{v}{R} + \frac{1}{2}\left[\left(\frac{dv}{ds} - \frac{u}{R}\right)^2 + \left(\frac{du}{ds} + \frac{v}{R}\right)^2 + \left(\frac{dw}{ds}\right)^2\right] \tag{3.61}$$

where $\varepsilon_{x,l}$ is the linear term of the axial strain, as given in Eq. (3.43); and $\varepsilon_{x,n}$ is the second order term of the axial strain. Since $\varepsilon_{x,l}$ is the dominant term in ε_x and ${\varepsilon_{x,n}}^2 \ll 2\varepsilon_{x,l}\varepsilon_{x,n}$, the strain energy U_n due to $\varepsilon_{x,n}$ can be obtained by neglecting the fourth order term ${\varepsilon_{x,n}}^2$, given by

$$U_n = F_x \int_{-\varphi_0}^{\varphi_0} \left[\left(\frac{dv}{ds} - \frac{u}{R}\right)^2 + \left(\frac{du}{ds} + \frac{v}{R}\right)^2 + \left(\frac{dw}{ds}\right)^2\right] R d\varphi \tag{3.62}$$

where F_x is the axial internal force. Substituting Eq. (3.52) into Eq. (3.62) and taking the partial derivative of U_n with respective to $\boldsymbol{u_e}$, the geometric stiffness matrix $\left[k_{n,e}\right]$ of the element can be obtained as

$$\frac{\partial U_n}{\partial \boldsymbol{u_e}} = \left(F_x \int_{-\varphi_0}^{\varphi_0} \boldsymbol{V}(\varphi)^{\mathrm{T}} \boldsymbol{V}(\varphi) R d\varphi \right) \boldsymbol{u_e} = \left[k_{n,e}(\boldsymbol{u_e}) \right] \boldsymbol{u_e} \tag{3.63}$$

with

$$\left[k_{n,e} \right] = F_x \int_{-\varphi_0}^{\varphi_0} \boldsymbol{V}(\varphi)^{\mathrm{T}} \boldsymbol{V}(\varphi) R d\varphi \tag{3.64}$$

$$\boldsymbol{V}(\varphi) = \begin{bmatrix} 0 & 0 & 0 & 1 & 1 & 0 & 0 & 0 & 0 & 0 & 0 & 0 \\ 0 & 0 & 0 & 0 & -\frac{1}{R} & -\frac{\varphi}{R} & 0 & 0 & 0 & 0 & 0 & 0 \\ 0 & 0 & 0 & 0 & 0 & 0 & 0 & 0 & 0 & R\varphi & 1 & 0 \end{bmatrix} \begin{bmatrix} \left[A(-\varphi_0) \right] \\ \left[A(\varphi_0) \right] \end{bmatrix}^{-1} \tag{3.65}$$

With the geometric stiffness matrix, the buckling behavior and stability of curved structures can be analyzed. The geometric stiffness matrix is nonlinear since it is dependent on the axial internal force F_x. In Section 4.2, numerical methods are discussed to solve the nonlinear static and dynamic problems. The development of the curved beam element and corresponding numerical analyses can be found in reference [92][93].

3.4. System Dynamics Under Global Coordinate

3.4.1. Matrix Rotation and Combination

In Sections 3.1, 3.2 and 3.3, dynamic equations are established for local beam elements. The global dynamic equation for the entire system can be obtained by combining the local stiffness, mass, and damping matrices. A rotation matrix is created earlier in Section 2.2 to transform vectors from local coordinates to the global coordinate, given by

$$\begin{bmatrix} a_X \\ a_Y \\ a_Z \end{bmatrix} = \left[T_r\right]^{\mathrm{T}} \begin{bmatrix} a_x \\ a_y \\ a_z \end{bmatrix} \tag{3.66}$$

where a_x, a_y, and a_z are vector components in local *x*, *y*, and *z* directions; a_X, a_Y, and a_Z are vector components in global *X*, *Y*, and *Z* directions.

The global element mass matrix $[M_e]$ (dimension 12×12) can be transformed from $[m_e]$ through

$$\left[M_e\right] = \begin{bmatrix} \left[T_{r,1}\right] & [0] & [0] & [0] \\ [0] & \left[T_{r,1}\right] & [0] & [0] \\ [0] & [0] & \left[T_{r,2}\right] & [0] \\ [0] & [0] & [0] & \left[T_{r,2}\right] \end{bmatrix}^{\mathrm{T}} \left[m_e\right] \begin{bmatrix} \left[T_{r,1}\right] & [0] & [0] & [0] \\ [0] & \left[T_{r,1}\right] & [0] & [0] \\ [0] & [0] & \left[T_{r,2}\right] & [0] \\ [0] & [0] & [0] & \left[T_{r,2}\right] \end{bmatrix} \tag{3.67}$$

where $\left[T_{r,1}\right]$ and $\left[T_{r,2}\right]$ (dimension 3×3) are rotation matrices of the two end nodes. The global linear stiffness matrix for element $\left[K_{e,l}\right]$, nonlinear stiffness matrix for element $\left[K_{e,n}\right]$, and the global damping matrix for element $[D_e]$ can be obtained from their local counterparts using the same approach.

By assembling the global element matrices, the global mass matrix for system $[M]$, linear stiffness matrix for system $[K_l]$, nonlinear stiffness matrix for system $[K_n]$,

and damping matrix for system $[D]$ can be obtained. For $[M]$, for example, the assembling process is given by

$$[M]=\begin{bmatrix} [M_e]^1_{11} & [M_e]^1_{12} & [0] & \cdots & [0] & [0] & [0] \\ [M_e]^1_{21} & [M_e]^1_{22}+[M_e]^2_{11} & [M_e]^2_{12} & \cdots & [0] & [0] & [0] \\ [0] & [M_e]^2_{21} & [M_e]^2_{22} & \cdots & [0] & [0] & [0] \\ \vdots & \vdots & \vdots & \ddots & \vdots & \vdots & \vdots \\ [0] & [0] & [0] & \cdots & [M_e]^{N-2}_{22}+[M_e]^{N-1}_{11} & [M_e]^{N-1}_{12} & [0] \\ [0] & [0] & [0] & \cdots & [M_e]^{N-1}_{21} & [M_e]^{N-1}_{22}+[M_e]^{N}_{11} & [M_e]^{N}_{12} \\ [0] & [0] & [0] & \cdots & [0] & [M_e]^{N}_{21} & [M_e]^{N}_{22} \end{bmatrix} \tag{3.68}$$

with

$$[M_e]^i=\begin{bmatrix} [M_e]^i_{11} & [M_e]^i_{12} \\ [M_e]^i_{21} & [M_e]^i_{22} \end{bmatrix} \tag{3.69}$$

where the superscript *i* denotes the element number; and *N* is the number of elements.

Finally, the system dynamic equation can be expressed as

$$\left([K_l]+[K_n]\right)\boldsymbol{U}+[D]\dot{\boldsymbol{U}}+[M]\ddot{\boldsymbol{U}}=\boldsymbol{F}-\boldsymbol{R} \tag{3.70}$$

where $\boldsymbol{U}$, $\dot{\boldsymbol{U}}$, and $\ddot{\boldsymbol{U}}$ are system displacement vector, velocity vector, and acceleration vector, respectively; $\boldsymbol{F}$ and $\boldsymbol{R}$ are the external force vector and the initial force vector, which are transformed from $\boldsymbol{f_e}$ and $\boldsymbol{r_e}$ in Eq. (3.36). In this research, the gravity, drill-string wellbore interaction, top drive force, and bit force are considered by the external force vector.

3.4.2. Free Vibration and Eigenvalue Problem

After obtaining the mass and stiffness matrices of a structure, the features of this structure can be determined. For a thin beam under compression, it buckles if the axial load exceeds the buckling threshold. In FEM, buckling failure is characterized by zero and negative eigenvalues of the stiffness matrix. The linear stiffness matrix $[K_l]$ is positive definite. However, the nonlinear geometric stiffness matrix $[K_n]$ can have negative eigenvalues under compression loads. The minimum axial force which results to a zero eigenvalue is the buckling threshold. Higher than that value results to a buckling failure.

The natural frequencies and vibration modes of a system can also be determined from the stiffness and mass matrices. For an undamped free vibration system, we have

$$[K]\boldsymbol{U} + [M]\ddot{\boldsymbol{U}} = 0 \tag{3.71}$$

The natural frequency ω_i and vibration mode $\boldsymbol{\phi_i}$ yield:

$$\left(-\omega_i^2[M] + [K]\right)\boldsymbol{\phi}_i = 0 \tag{3.72}$$

Based on Eq. (3.72), the square of natural frequencies are the eigenvalues of $[M]^{-1}[K]$ and the corresponding eigenvectors are the vibration modes. The undamped free vibration can be expressed by the combination of vibration modes, given by

$$\boldsymbol{U}(t) = \alpha_1\boldsymbol{\phi}_1 e^{i\omega_1 t} + \alpha_2\boldsymbol{\phi}_2 e^{i\omega_2 t} + \cdots \alpha_{n-1}\boldsymbol{\phi}_{n-1} e^{i\omega_{n-1} t} + \alpha_n\boldsymbol{\phi}_n e^{i\omega_n t} \tag{3.73}$$

where α_1 to α_n are coefficients; i is the imaginary number. Let λ_i, equals to ω_i^2, be the i^{th} eigenvalue of $[M]^{-1}[K]$. If λ_i is positive, $\pm\omega_i$ are real numbers and the corresponding vibrations are stable. If λ_i is negative, $\pm\omega_i$ are imaginary and one of $e^{i\omega_i t}$ and $e^{-i\omega_i t}$ is unstable. If λ_i is a complex number, its conjugate $\overline{\lambda_i}$ is also complex. The square roots of λ_i and $\overline{\lambda_i}$ are in the format of $\pm a_i \pm ib_i$, where two of them are unstable. Therefore, for a dynamic system to be stable, the eigenvalues of $[M]^{-1}[K]$ must be positive. Since $[M]$ is usually positive definite, the eigenvalues of $[K]$ need to be positive for a system to be stable. In this problem, $[K]$ has zero or negative eigenvalues when the beam buckles and the dynamic system loses stability. However, realistic drilling scenarios are much more complex than beam free vibration. In next chapter, boundary conditions of realistic drilling scenarios are developed and incorporated into the FEM modeling framework. The corresponding numerical methods are also studied. It is shown that, unlike free vibration, the drilling dynamics can keep stable when buckling happens because of the support from wellbore.

3.4.3. Steady State Dynamics

The dynamic equation considering external force yields

$$[K]\boldsymbol{U} + [D]\dot{\boldsymbol{U}} + [M]\ddot{\boldsymbol{U}} = \boldsymbol{F} \tag{3.74}$$

where $\boldsymbol{F}$ is the external force. In steady state, the vibration frequency of the structure equals to the frequency of external excitation. In drilling scenario, as the BHA rotates, it receives a periodical excitation at a radial frequency of ω. Therefore, during steady state,

the excitation force can be expressed as $\|\boldsymbol{F}\|e^{i\omega}$. Decomposing the vibration frequency ω and the vibration magnitude $\boldsymbol{\Phi}$, yields

$$-\omega^2[M]\boldsymbol{\Phi}e^{i\omega}+[K]\boldsymbol{\Phi}e^{i\omega}+i\omega[D]\boldsymbol{\Phi}e^{i\omega}=\|\boldsymbol{F}\|e^{i\omega} \tag{3.75}$$

And the vibration magnitude $\boldsymbol{\Phi}$ can be obtained from

$$\boldsymbol{\Phi}=\left(-\omega^2[M]+[K]+i\omega[D]\right)^{-1}\|\boldsymbol{F}\| \tag{3.76}$$

With Eq. (3.76), the BHA vibration mode shape under a given RPM can be obtained.

3.5. Simulation and Verification

In this section, case studies are conducted to verify the proposed FEM models. Section 3.5.1 studies the vibration of a straight cantilever, which verifies the FEM model proposed in Section 3.1. Section 3.5.2 simulates two large displacement cases to verify the method proposed in Section 3.2. The curved beam element developed in Section 3.3 is simulated in Section 3.5.3.

3.5.1. Vibration of a Straight Cantilever

In this section, the proposed model is applied to analyze the axial, torsional, and lateral dynamics of a straight cantilever. The beam parameters are listed in Table 3-1. Based on Section 3.4.2, the numerical natural frequencies and vibration modes are calculated, where the vibration modes are illustrated in Figure 3-5, and the natural frequencies are compared with analytical solutions in Table 3-1. According to Table 3-1

and Figure 3-5, the numerical natural frequencies and vibration modes match the analytical solutions well in all directions.

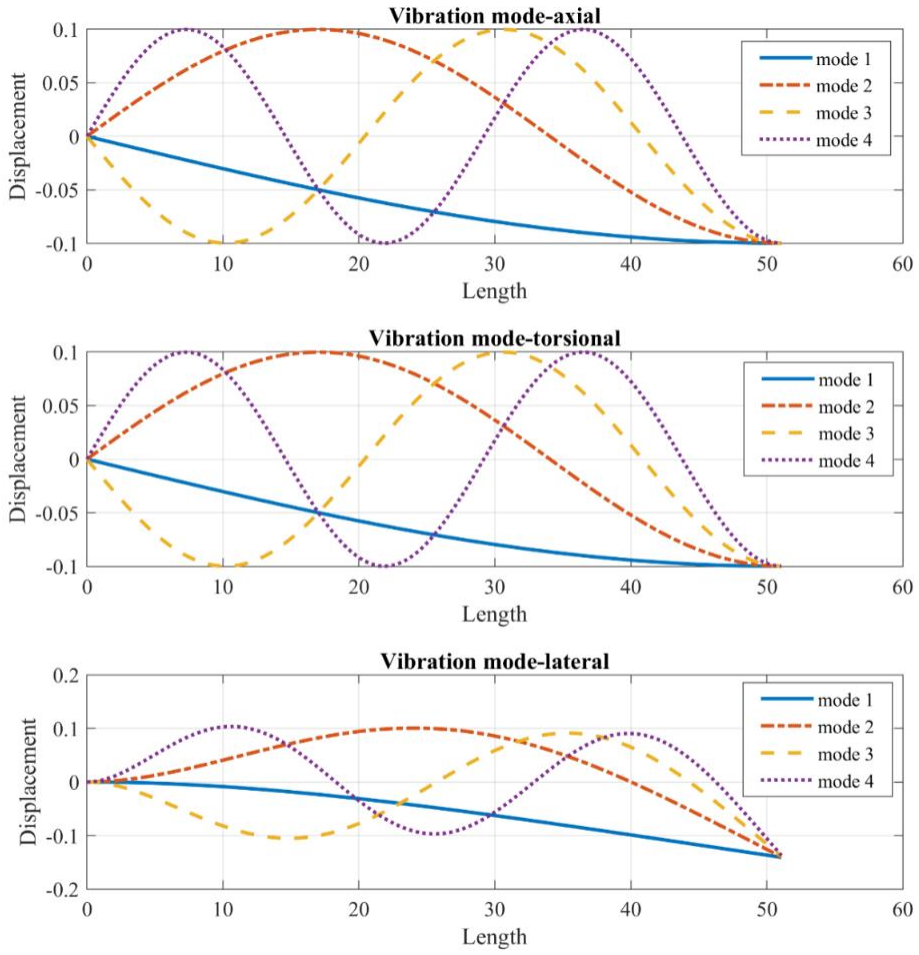

Figure 3-5. Vibration modes in axial, torsional, and lateral directions

Parameter	Value
Inner radius	0.0714 [m]
Outer radius	0.1715 [m]
Length	51.07 [m]
Density	7830 [kg/m^3]
Young's	206.8 [GPa]
Poisson ratio	0.3

Table 3-1. Straight cantilever data

Natural frequency		Analytical	Numerical
Axial	1st	158.0696	158.0700
	2nd	474.2089	474.2198
	3rd	790.3481	790.3988
	4th	1106.4873	1106.6266
Torsional	1st	98.0306	98.0309
	2nd	294.0918	294.0987
	3rd	490.1531	490.1846
	4th	686.2143	686.3007
Bending	1st	0.3216	0.3217
	2nd	2.0158	2.0159
	3rd	5.6450	5.6446
	4th	11.0621	11.0612

Table 3-2. Natural frequencies, numerical vs. analytical

3.5.2. Large Displacement Simulation

In this section, two case studies are conducted to verify the proposed method in dealing with large bending problems. Drill-string bending can be considerable during directional drilling; therefore, geometry nonlinearities should be considered. Based on Section 3.2.2, the dynamic problem is linearized around the well central axis.

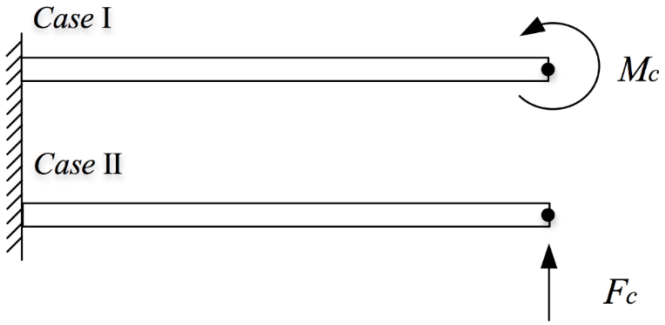

Figure 3-6. Case studies, M_c is centralized moment and F_c is centralized force

As illustrated in Figure 3-6, in the first case, a centralized moment M_c is applied on the free end of a cantilever, formulated by

$$M_c = n\frac{2\pi EI}{L} \tag{3.77}$$

where n is a coefficient ranging from 0 to 1; and I and L are the second moment of area and the beam length, respectively. External force M_c is sufficient to induce large bending to the beam. Given the reference displacement, the initial internal force $\boldsymbol{R}$ is calculated using Eq. (3.36), and then Eq. (3.70) is implemented to determine the subsequent deformation, which should be very small (zero, ideally). Because the external force M_c is static, the displacement can stabilize to a fixed value. Adding this value to initial displacement, the overall displacement is obtained as illustrated in Figure 3-7.

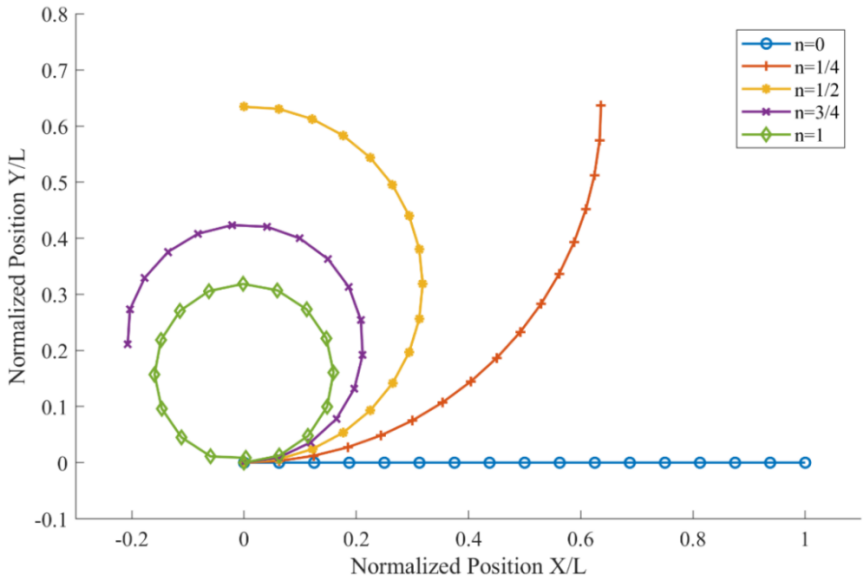

Figure 3-7. The large bending of a thin beam under centralized moment M_c

As illustrated in Figure 3-6, in the second case, a centralized force F_c is applied on the free end of a cantilever, where

$$F_c = n\frac{\pi^2 EI}{4L^2} \tag{3.78}$$

With known F_c and given reference, a small displacement is obtained from Eq. (3.36) when reaching dynamic equilibrium, with the results illustrated in Figure 3-8. The obtained results in Figure 3-7 and Figure 3-8 are verified by comparing with [94]. According to the preceding case studies, the proposed model can accurately capture the beam dynamics and the nonlinear behaviors caused by large bending, which makes it suitable to solve the directional drilling problem.

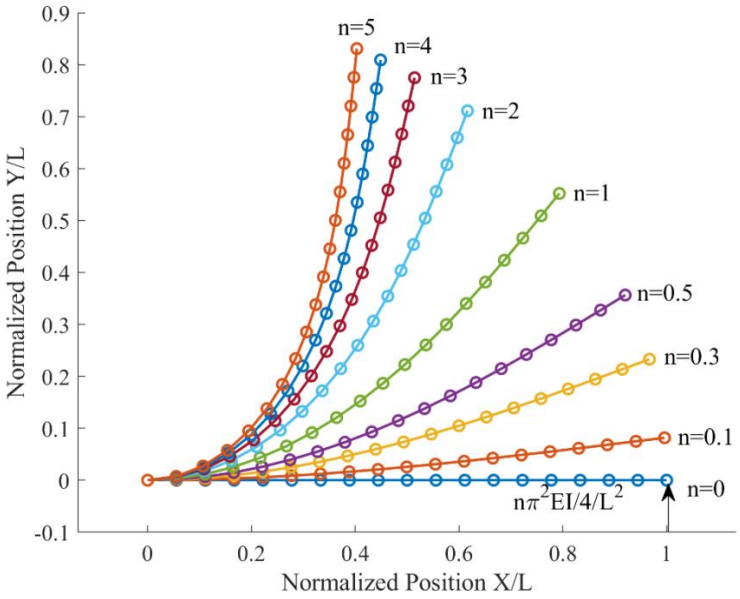

Figure 3-8. The large bending of a thin beam under centralized force F_c

3.5.3. Curved Beam Element

In this section, simulations and case studies are conducted to verify and validate the developed curved beam element. In the first simulation, results from static analysis on a curved structure are shown, and the result from the curved beam method is compared with the analytical solution as well as the result from the straight beam method. In the second simulation, the dynamic performance of the curved beam element is verified

through natural frequency calculations. In the third simulation, the nonlinear geometric stiffness matrix derived in this paper is included to calculate the structure deformations.

3.5.3.1. Static Analysis

As illustrated in Figure 3-9, a half circle is analyzed where the left end is clamped, and the right end is loaded. The parameters of the half circle are listed in Table 1, where R is the radius of the half circle; A is the cross-sectional area; I is the second moment of area in flexural direction; I_ρ is the second moment of area in torsional direction; E is the Young's modulus; G is the shear modulus; and ρ is the material density.

Translational forces $[F_X \ F_Y \ F_Z]^{\mathrm{T}}$ $(= [10^4 \ 10^4 \ 10^4]^{\mathrm{T}})$ are applied on the right end of the circle and the displacements in three directions $[\delta_X \ \delta_Y \ \delta_Z]^{\mathrm{T}}$ are obtained analytically using Castigliano's method [95], given by

$$\begin{bmatrix} \delta_X \\ \delta_Y \\ \delta_Z \end{bmatrix} = \begin{bmatrix} \frac{\pi R^3}{2EI} & \frac{2R^3}{EI} & 0 \\ \frac{2R^3}{EI} & \frac{3\pi R^3}{2EI} & 0 \\ 0 & 0 & \frac{\pi R^3}{2EI} + \frac{3\pi R^3}{2GI_\rho} \end{bmatrix} \begin{bmatrix} F_X \\ F_Y \\ F_Z \end{bmatrix} \tag{3.79}$$

where F_X, F_Y, and F_z are the translational forces in the X, Y, and Z directions respectively; and δ_X, δ_Y, and δ_Z are the displacements in the X, Y, and Z directions respectively.

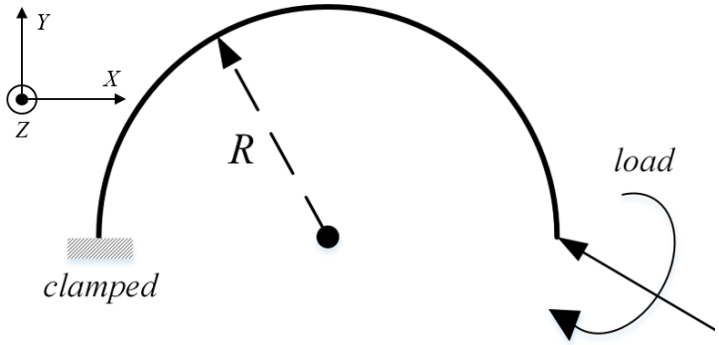

Figure 3-9. Structure for static and dynamic analysis

Parameter	Value
R [m]	20
A [m^2]	1
I [m^4]	0.04
I_o [m^4]	0.08
E [GPa]	220
G [GPa]	91.67
ρ [kg/m^3]	8050

Table 3-3. Simulation parameters

The analytical result is used as a benchmark to evaluate the performance of numerical methods. According to [96], the approximation of this curved structure with straight beam elements can converge to the analytical result if the meshing size is fine enough. In this study, both the proposed curved element and the classic straight element are implemented for analysis. In Table 2, the numerical results with 500 elements are calculated and compared with analytical solution. They all converge to the analytical values, which verifies the proposed curved beam element and the conclusion from [96]. The displacement of the continuous structure is also obtained. As illustrated in Figure 3-10, the results of the curved beam element and the straight beam element agree well with each other when meshing with very fine elements.

	Analytical	Curved Element	Straight Element
δ_X [m]	0.03246178	0.03246300	0.03246323
δ_Y [m]	0.06102172	0.06102289	0.06102318
δ_Z [m]	0.06568785	0.06568786	0.06568751

Table 3-4. Comparison with analytical solution

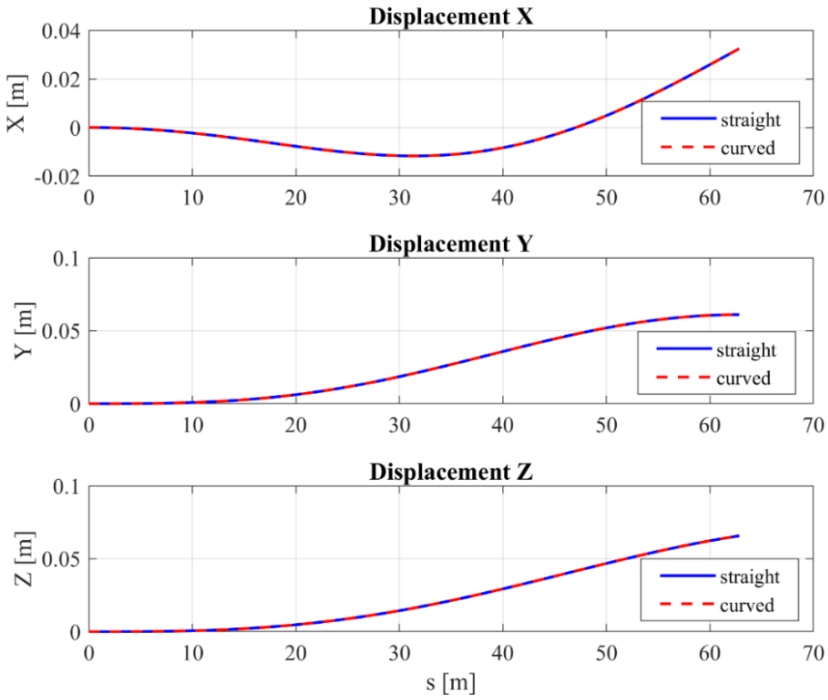

Figure 3-10. Displacement of the continuous structure

To understand the convergence rate of the curved beam element, the structure in Figure 3-9 is meshed with different numbers of elements, ranging from 3 to 30. On the right end of the half circle, external forces $[F_X\ F_Y\ F_Z\ T_X\ M_Y\ M_Z]^{\mathrm{T}}$ ($= [10^4\ 10^4\ 10^4\ 10^4\ 10^4\ 10^4]^{\mathrm{T}}$), including translational forces F_X, F_Y, and F_Z, bending moments M_Y and M_Z, and torsion T_X, are applied. The displacements in X, Y, and Z directions and the rotation in axial direction are calculated. The errors are plotted against the number of elements on a log-log plot and compared with the results of the straight element method. As we can see from Figure 3-11, compared with the straight beam

element, the numerical accuracy is significantly increased when the curved beam element is used. The convergence rate can be determined from the slope of error line. With the straight beam element, the displacements in all directions yield a second-order convergence rate. With the curved beam element, the in-plane displacements can reach a fourth-order convergence rate. In terms of the out-of-plane displacement and rotation, both elements yield the same order of convergence rate, while the relative error of the curved beam element is significantly reduced. When meshing with three straight elements, the error of out-of-plane displacement can be up to 13.73% and the error of rotation can be up to 14.09%. However, when meshing with three curved elements, the error of out-of-plane displacement and the error of rotation are reduced to 2.31% and 0.38%, respectively.

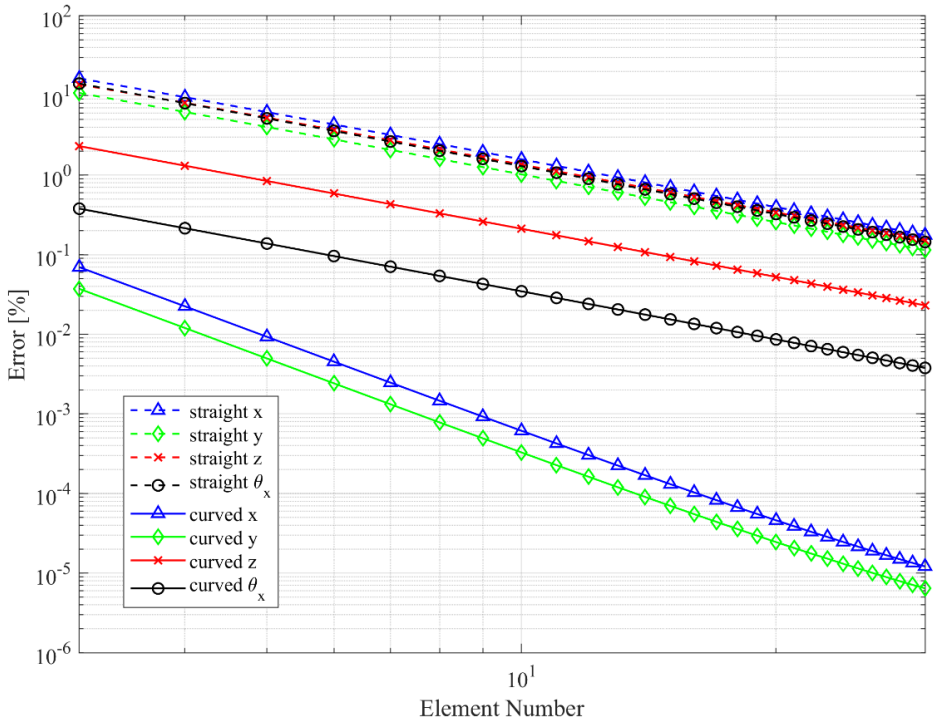

Figure 3-11. Error comparison of static simulation

3.5.3.2. Dynamic Analysis

The preceding case study verifies the static response of the curved beam element by comparing with analytical solutions and indicates a higher accuracy of the curved beam element compared to the straight beam element. In this case, the dynamic responses of the elements are tested via natural frequency. For a finite element model, the structure natural frequencies can be calculated by

$$\boldsymbol{\omega} = \sqrt{\text{eig}\left(\left[M\right]^{-1}\left[K\right]\right)} \tag{3.80}$$

where $\boldsymbol{\omega}$ represents the structure natural frequencies (in rad/s); and $\text{eig}(\cdot)$ calculates the eigenvalues of a matrix.

For the half circle illustrated in Figure 3-9, the first five natural frequencies are calculated using both the curved beam element and the straight beam element. The root mean squared errors (RMSE) are calculated under different meshing sizes and the results are compared in Table 3. The numerical errors of the straight beam element and the curved beam element decrease with the same slope as the number of elements increases. With five elements, the RMSE of the straight beam element is 4.889% and the RMSE of the curved beam element is only 0.755%, which indicates a better dynamic response of the curved beam element.

Element NO.	5	10	15	20	25	30
Straight element	4.889%	1.240%	0.550%	0.308%	0.196%	0.135%
Curved element	0.755%	0.185%	0.082%	0.046%	0.029%	0.020%

Table 3-5. Error comparison of natural frequency

3.5.3.3. Geometric Stiffness

In this simulation, the geometric stiffness developed in Section 3.3.3 is included for analysis. The structure is illustrated in Figure 3-13, where the two end points are clamped, and the midpoint is loaded. The parameters are listed in Table 3-6. The loading forces $[F_X \ F_Y \ F_Z \ T_X \ M_Y \ M_Z]^{\mathrm{T}}$ are selected as $4 \times [10^5 \ -10^5 \ 10^5 \ 10^5 \ 10^5 \ 10^5]^{\mathrm{T}}$, where the compression force causes the beam's first natural frequency to reduce by 5%. The displacement of the midpoint is calculated under different numbers of elements, ranging from 4 to 40. The numerical errors of the curved beam element and the straight beam element are illustrated in Figure 3-13 using a log-log plot. According to the simulation results, the in-plane displacements of the curved beam element yield a higher convergence rate than the straight beam element. Although the out-of-plane displacement and rotation of the curved beam element yield the same convergence rate as the straight beam element, the relative error of curved beam element is significantly reduced. With four straight elements, the errors of out-of-plane displacement and rotation are 2.09% and 4.43%, respectively; and with four curved elements, the errors of out-of-plane displacement and rotation are reduced to 1.16% and 0.58%, respectively.

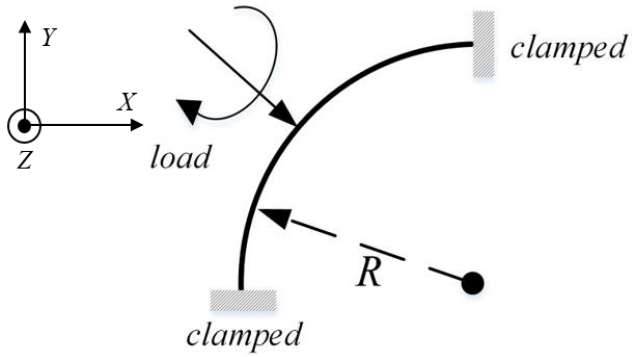

Figure 3-12. Structure for geometric stiffness

Parameter	Value
R [m]	20
A [m^2]	0.1
I [m^4]	10^{-3}
I_o [m^4]	2×10^{-3}
E [GPa]	220
G [GPa]	91.67

Table 3-6. Simulation parameters

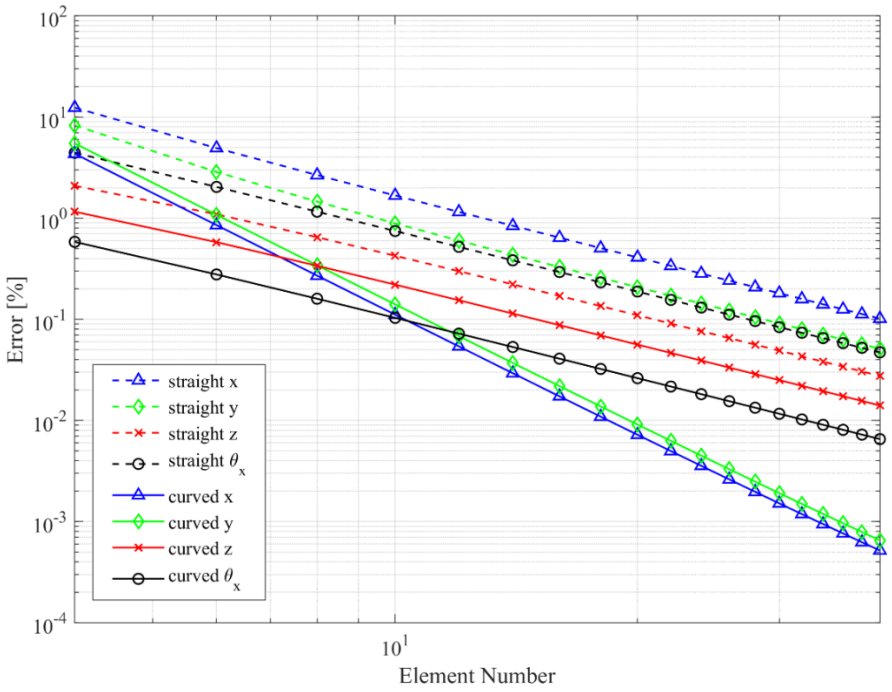

Figure 3-13. Error comparison by including geometric stiffness

3.6. Summary

In this chapter, three finite element methods are developed to model the drill-string dynamics. With the assumption of small displacement and small deformation, the Lagrangian method is firstly implemented to develop a dynamic FEM model suitable for vertical drilling simulation. This model is verified by comparing against analytical solutions when analyzing a straight cantilever. However, the assumption of small

displacement is violated in directional drilling scenarios. Based on the principle of virtual work, a second FEM model is developed which linearizes the drill-string dynamics around the central axis of a directional well. The developed method is applied to solve large displacement problems and agrees well with existing methods. In traditional finite element models, a directional drill-string is approximated with a serial of straight elements. However, the coupling mechanism among different degrees of freedoms is not considered by the straight beam elements. Meanwhile, the straight beam approximation introduces additional discretization error; therefore, a very fine meshing is necessary to guarantee the numerical accuracy for the straight beam method, which leads to a low computational efficiency. To deal with this problem, a six DOF curved beam element is derived using the assumed strain field method. According to the simulation results, the developed curved beam element achieves higher accuracy than the straight beam element in both static and dynamic analyses. As a result, compared with the straight beam elements, fewer curved beam elements can be used to achieve the same accuracy, which reduces the computational cost.

Chapter 4. BOUNDARY CONDITION AND NUMERICAL METHOD

This chapter introduces the boundary conditions for directional drilling as well as the numerical methods to solve the proposed FEM problem. The boundary conditions at the upper end of a drill-string are determined by the draw-works and the top drive. The draw-works is used to hoist the drill-string and move it up and down. And the top drive is fixed on the rig and creates torque to drive the drilling system. Many top drive controllers have been proposed to suppress the stick-slip vibrations [66]-[74]. Among these top drive controllers, the soft torque method [71][72] and the soft speed method [73][74] are most well-known and have achieved commercialization. In this section, these two methods are incorporated into the developed FEM model as top drive boundary conditions. The boundary conditions at the lower end of a drill-string are determined by the forces on bit. In this section, a comprehensive bit force model is developed, which fully considers the influence of the BHA eccentricity, mud damping, bit-rock interactions in axial, lateral, and torsional directions, and their coupling mechanisms. Depending on the ways of being imposed, boundary conditions are classified into essential boundary condition and natural boundary condition. The former one is explicitly imposed onto the solution. While the latter one is satisfied automatically when a solution is obtained.

4.1. Boundary Condition

4.1.1. Top Drive and Draw-works

Part of this chapter was published in 1. Feng, T., et al. "A Finite Element Method with Full Bit-Force Modeling to Analyze Drillstring Vibration." *Journal of Dynamic Systems, Measurement, and Control* 139.9 (2017): 091016; 2. Feng, T., Bakshi, S. Gu, Q. Chen, D. "A Finite Element Modeling Framework for Curved Beam Dynamics Considering Nonlinearities and Contacts". *Journal of Computational and Nonlinear Dynamics*. doi: 10.1115/1.4043452.
The author contributes to develop the boundary conditions for drill-string/bit and wellbore interaction

Drill-string is clamped at the top drive; therefore, the lateral displacements and bending angles of the corresponding node are zero. This can be imposed by deleting the corresponding columns and rows of the dynamic equation. The drill-string is connected to the rig using a draw-works and the resultant force called hook load, sets the upper axial boundary condition. In the developed drill-string model, the users can directly set the hook load or provide a desirable WOB and the hook load can be back calculated through static analysis.

The rotation of the drill-string is driven by the top drive. Many top drive controllers have been proposed to suppress stick-slip vibrations. When integrated with the proposed FEM model, the control output sets the upper torsional boundary condition. In this chapter, the speed Proportional-Integral (PI) controller, the soft speed controller, and the soft torque controller are developed and simulated. The speed PI controller can be formulated by

$$T_d = K_P(\Omega_0 - \omega_{TD}(t)) + K_I \int_0^t (\Omega_0 - \omega_{TD}(\tau))d\tau \tag{4.1}$$

where T_d is the driving torque; K_P is the proportional gain; K_I is the integral gain; Ω_0 is the set point of rotary speed; and $\omega_{TD}(t)$ is rotary speed of the top drive.

4.1.1.1. Soft Speed Control

The soft speed controller keeps the form of a speed PI controller. But the proportional gain and integral gain are carefully selected to damp out torsional vibrations at desired frequencies [73]. With given K_P and K_I, the reflection rate at surface can be determined by [73]

$$r_d = \frac{K_P - \varsigma + i \cdot (2\pi f \cdot J_d - \frac{K_I}{2\pi f})}{K_P + \varsigma + i \cdot (2\pi f \cdot J_d - \frac{K_I}{2\pi f})} \tag{4.2}$$

where r_d is the reflection rate; ς is the system impedance; i is the imaginary number; f is the vibration frequency; J_d is the rotary inertia of the top drive. It is incorporated into the FEM model as a lumped inertia, given by

$$M_{TD} = \begin{bmatrix} \rho l_e I_\rho / 3 + J_d & \rho l_e I_\rho / 6 \\ \rho l_e I_\rho / 6 & \rho l_e I_\rho / 3 \end{bmatrix} \tag{4.3}$$

where M_{TD} is the mass matrix of the element adjacent to the top drive; l_e is the length of the element. The six DOF element has a dimension of 12×12. In Eq. (4.3), only the torsional direction is provided, where the entries [1 1], [1 2], [2 1] and [2 2] correspond to [4 4], [4 10], [10 4] and [10 10] of the full element.

Assuming the stick-slip vibration frequency is f_n, the reflection rate is minimized by choosing

$$K_I = J_d \left(2\pi f_n\right)^2 \tag{4.4}$$

And the corresponding reflection rate is

$$\left|r_d\right|_{\min} = \frac{\left|K_P - \varsigma\right|}{K_P + \varsigma} \tag{4.5}$$

The reflection rate r_d can be further modified through tuning K_P. A small r_d can effectively reduce BHA stick-slip. However, the speed fluctuation at surface can grow up

as a side effect. Accordingly, a certain level of reflection rate needs to be maintained to keep top drive speed constant.

4.1.1.2. Soft Torque Control

The underlying idea of the soft torque method is to control top drive torque to make it work as an energy absorber for torsional waves [70]. This can be achieved by feeding surface torque fluctuation back into a speed PI controller, given by [70][71]

$$T_d = K_P(\Omega_0 - \omega_{TD}(t) - H_0 T_f) + K_I \int_0^t (\Omega_0 - \omega_{TD}(\tau) - H_0 T_f) d\tau \tag{4.6}$$

where H_0 is a tunable parameter to get desirable system damping; and T_f is torque fluctuation at the top drive. T_f can be obtained by filtering the torque signal using a high-pass filter, given by

$$T_f = \frac{i \cdot f}{i \cdot f + f_0} T_s \tag{4.7}$$

where i is the imaginary number; f is the frequency; f_0 is the cutting off frequency; and T_s is the torque signal measured at surface. Figure 4-1 compares the output torques of a speed PI controller and a soft torque control. The blue line is the top drive torque of a speed PI controller. When torsional waves hit the top drive, the torque changes significantly to keep the top drive speed constant, which exacerbates the stick-slip vibration. The green line illustrates the fluctuation of the driving torque, which is calculated using Eq. (4.7). The red line is the driving torque of a soft torque controller. It reacts less significantly when torsional waves hit the top drive and therefore damps out these waves. By tuning H_0 in Eq. (4.6), the reflection rate of torsional waves can be

adjusted. A lower reflection rate is more effective in mitigating the stick-slip vibration. As an additional benefit, a smooth bit rotation can also result in a reduction of the axial and lateral vibrations [70].

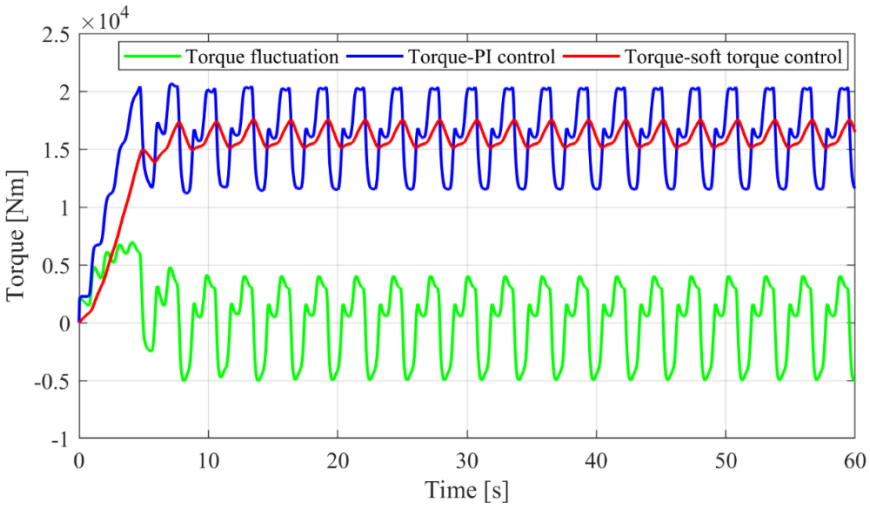

Figure 4-1. Top drive torque of speed PI controller and soft torque controller

4.1.2. Interaction Between the Drill-string and Wellbore

When a drill-string curves inside a directional well, the outer shell of the drill-pipe can contact the wellbore and the reactive force keeps the drill-string inside the wellbore. Assuming the cross section of the well is circular, the boundary of the wellbore can be determined with known well trajectory and cross-sectional radius. Under the local coordinate frame introduced in Section 2.2, drill-string and wellbore contacts can be easily detected. The contact model is illustrated in Figure 4-2, where the *yz* plane is the cross-section of the drill-string and the *x* axis points towards the tangent direction. After deformation, the circular center moves from *o* to *o'* and the displacements in the *x*, *y* and *z* directions are *u*, *v* and *w*, respectively.

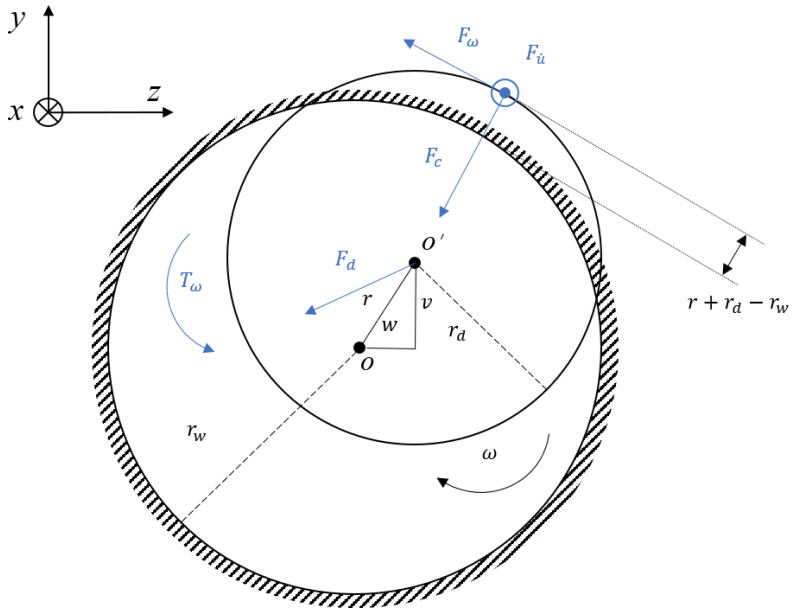

Figure 4-2. Drill-string and wellbore contact model

The penalty method is applied to calculate the contact force [97], where the magnitude of the contact force is proportional to the penetrating depth, given by

$$F_c = \begin{cases} -k_w\left(r + r_d - r_w\right) & , r + r_d > r_w \\ 0 & , \text{otherwise} \end{cases} \tag{4.8}$$

where F_c is the magnitude of the contact force; k_w is the stiffness of the wall; r is the lateral displacement of the node (the displacement in yz plane); r_d is the radius of the beam; and r_w is the radius of the wall. For dynamic analysis, kinetic energy dissipates during contact and a damping force is added to model this process, given by

$$F_d = \begin{cases} -d_w\dot{r} & , r + r_d > r_w \\ 0 & , \text{otherwise} \end{cases} \tag{4.9}$$

where F_d is the magnitude of the damping force; $\dot{r}$ is the node velocity in lateral direction (the velocity in *yz* plane); and d_w is the equivalent damping of the wellbore, which accounts for the energy loss in drill-string and wellbore contact. Drill-string lateral displacement r and velocity $\dot{r}$ are given by

$$\begin{cases} r = \sqrt{\left(v^2 + w^2\right)} \\ \dot{r} = \sqrt{\left(\dot{v}^2 + \dot{w}^2\right)} \end{cases} \tag{4.10}$$

where $\dot{v}$ and $\dot{w}$ are drill-string velocities in local *y* and *z* directions, respectively. The Coulomb model is implemented to describe the friction, where the magnitude of friction is proportional to the normal force and the friction direction is opposite to the velocity. As a result, the friction component in the *yz* plane, F_ω, and the friction component in the *x* direction, $F_{\dot{u}}$, can be represented as

$$F_\omega = F_c \mu \frac{r_d \omega}{\sqrt{\left(r_d \omega\right)^2 + \dot{u}^2} + \xi} \tag{4.11}$$

$$F_{\dot{u}} = F_c \mu \frac{\dot{u}}{\sqrt{\left(r_d \omega\right)^2 + \dot{u}^2} + \xi} \tag{4.12}$$

where F_ω is caused by beam rotation ω; $F_{\dot{u}}$ is caused by beam velocity $\dot{u}$; ω is the beam rotary speed around *x* axis; $\dot{u}$ is the beam velocity in the *x* direction; μ is the friction coefficient; ξ takes a small positive value (equal to 10^{-5} in this research) to avoid singularities in F_ω and $F_{\dot{u}}$. In directional drilling, F_ω contributes to the torsional drilling

friction known as "*torque*", and $F_{\dot{u}}$ contributes to the axial drilling friction known as "*drag*".

Using Eq. (4.13), the contact force and friction force are transformed into the Cartesian coordinate frame defined by the *xyz* axes

$$\begin{cases} F_x = -F_{\dot{u}} \\ F_y = -F_c \cos(\theta_c) - F_d \cos(\theta_d) + F_\omega \sin(\theta_c) \\ F_z = -F_c \sin(\theta_c) - F_d \sin(\theta_d) - F_\omega \cos(\theta_c) \\ T_x = -F_\omega r_d \end{cases} \tag{4.13}$$

$$\begin{cases} \theta_c = \tan^{-1}\left(\dfrac{w}{v}\right) \\ \theta_d = \tan^{-1}\left(\dfrac{\dot{w}}{\dot{v}}\right) \end{cases} \tag{4.14}$$

where F_x, F_y and F_z are the forces in the *x*, *y* and *z* directions respectively; T_x is the torque in the *x* direction; θ_c denotes the displacement direction in the *yz* plane; and θ_d denotes the velocity direction in the *yz* plane.

4.1.3. Bit and Rock Interaction

This section presents a comprehensive bottom-hole boundary condition for PDC bit. It includes bit-rock interactions in axial, torsional, and lateral directions, BHA eccentricity, and mud hydraulic damping.

4.1.3.1. Bit Rock Impact Force

The axial and torsional forces applied on the bit are recognized as the WOB and TOB, respectively. In the work of Detournay and Defourny [98][99], the interaction force

applied on each cutter is decomposed into cutting component and frictional component, which are associated with the penetrating depth per iteration d_x. By integrating the cutter forces over the bit, the WOB and TOB_a (the components caused by WOB) are given by:

$$\begin{cases} WOB = WOC_c + WOC_f \\ WOC_c = \varepsilon r_b \zeta_f d_x \cdot H\left(\omega_b\right) \\ WOB_f = r_b l \sigma \kappa \cdot \min\left(\frac{1}{\kappa}, \frac{d_x}{d^*}\right) \end{cases} \tag{4.15}$$

$$\begin{cases} TOB_a = TOB_{a,f} + TOB_{a,c} \\ TOB_{a,f} = 0.5\mu\gamma_f r_b WOB_f \\ TOB_{a,c} = 0.5\varepsilon r_b^2 d_x \cdot H\left(\omega_b\right) \end{cases} \tag{4.16}$$

$$d_x = 2\pi \dot{u}_b / \omega_b \tag{4.17}$$

where WOB_c and $TOB_{a,c}$ are due to the cutting component of the cutter force; WOB_f and $TOB_{a,f}$ are due to the frictional (or rock compression) component of the cutter force; $\dot{u}_b$ and ω_b are the axial and torsional speeds of the bit, respectively; ε and σ are the intrinsic specific energy and contact strength of the rock, respectively; μ is the frictional coefficient; ζ_f is a bit geometry parameter that determines the friction condition of the cutter; κ and γ_f are bit constants that determine the rate of change of the cutter contact length and the cutter orientation on the bit face, respectively; r_b and l refer to bit radius and cutter wear length, respectively; $H(\cdot)$ is heavy-side function. The physical meaning of ε is the energy consumed to cut a unit volume of rock with ideal cutting. It relies on

not only the rock strength but also field conditions. σ reflects the maximum stress the rock can sustain, ranging from 1 *MPa* to hundreds of *MPa*. l quantifies the cutter bluntness, ranging from 1 mm to tens of mm [99].

The lateral force is analyzed under the polar coordinate (see Figure 4-3). Because the rock is assumed to be isotropic, the cutting process of the bit gauge should be the same as the cutting process of the bit face; therefore, the axial analysis is extended to the lateral direction as follows[26][100]:

$$\begin{cases} F_r^i = F_{r,f}^i + F_{r,c}^i \\ F_{r,f}^i = h_b l \sigma \kappa \cdot \min\left(\frac{1}{\kappa}, \frac{d_l}{d^{**}}\right) \\ F_{r,c}^i = \varepsilon h_b \zeta_g d_l \cdot H\left(\omega_b\right) \end{cases} \tag{4.18}$$

$$\begin{cases} F_\theta^i = F_{\theta,f}^i + F_{\theta,c}^i \\ F_{\theta,f}^i = \mu \gamma_g h_b l \sigma \kappa \cdot \min\left(\frac{1}{\kappa}, \frac{d_l}{d^{**}}\right) \\ F_{\theta,c}^i = \varepsilon h_b d_l \cdot H\left(\omega_b\right) \end{cases} \tag{4.19}$$

$$d_l = 2\pi \sqrt{\dot{v}_b^2 + \dot{w}_b^2} \Big/ \omega_b \tag{4.20}$$

where F_r^i and F_θ^i are the overall bit impact forces in radial and tangent directions, respectively; $F_{r,f}^i$ and $F_{\theta,f}^i$ are the impact forces due to the frictional component; $F_{r,c}^i$ and $F_{\theta,c}^i$ are the impact forces due to the cutting component; ζ_g is a bit geometry parameter that determines the friction condition of the cutter on the gauge and γ_g is a bit constant to determine the cutter orientation on bit gauge; h_b is the effective length of the gauge (the

length covered by cutters); $\dot{v}_b$ and $\dot{w}_b$ are bit velocities in local y and z directions. Eqs. (4.18) through (4.20) are applied only if a bit-rock collision is detected in lateral direction. Otherwise, all lateral bit-rock impact forces are set to zero. When calculating the cutting force F_r^i and F_θ^i, instead of using the averaged value over one revolution [101], an instantaneous force is applied by Eqs. (4.18) and (4.19) to accommodate for the properties of the FEM.

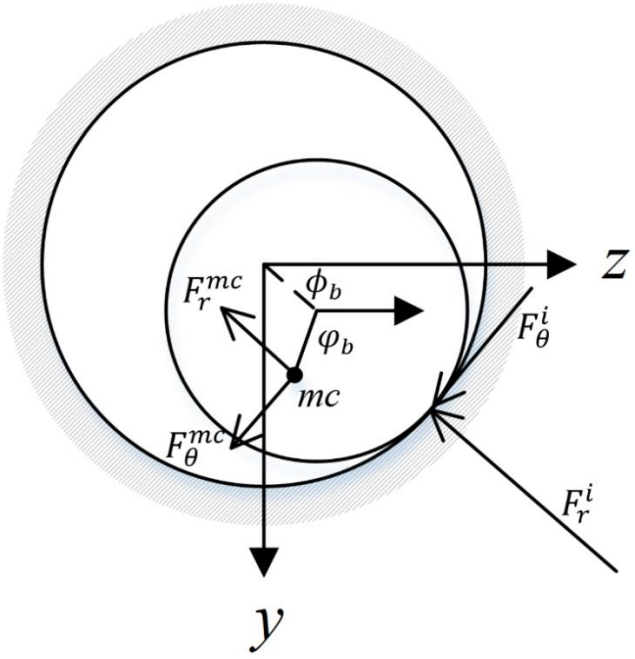

Figure 4-3. Lateral force under polar coordinate

4.1.3.2. BHA Eccentricity

The BHA mass center will deviate from its geometry center. Accordingly, when drill-string rotates, inertial force is produced. This force has not been considered in FEM modeling process; consequently, it is accounted for as an external force, given by

$$\begin{cases} F_r^e = me_0\left[\omega_b^2\cos\left(\phi_b-\varphi_b\right)+\dot{\omega}_b\sin\left(\phi_b-\varphi_b\right)\right] \\ F_\theta^e = me_0\left[\omega_b^2\sin\left(\phi_b-\varphi_b\right)-\dot{\omega}_b\cos\left(\phi_b-\varphi_b\right)\right] \end{cases} \tag{4.21}$$

where F_r^e and F_θ^e are the eccentricity forces of the BHA; m is the BHA mass; e_0 is the deviation of the BHA mass center from the geometry center; $\dot{\omega}_b$ is the bit torsional acceleration; ϕ_b and φ_b denotes the orientation of the bit geometry center and mass center, respectively.

4.1.3.3. Friction in Lateral Direction

This friction is attributed to bit movement or potential movement in lateral direction, which should be distinguished from the frictional component of WOB or other bit-rock impact forces. When bit velocity equals zero and external forces cannot overcome the maximum static friction exerted by WOB, the lateral friction is equal to the sum of the other forces; otherwise, the kinetic friction is applied, which can be expressed as

$$\begin{cases} F_r^{\,f} = -\mu WOB_f\dfrac{\dot{r}_{b,r}}{\sqrt{\dot{r}_{b,r}^2+\dot{r}_{b,\theta}^2}} \\ F_\theta^{\,f} = -\mu WOB_f\dfrac{\dot{r}_{b,\theta}}{\sqrt{\dot{r}_{b,r}^2+\dot{r}_{b,\theta}^2}} \end{cases} \tag{4.22}$$

where F_r^f and F_θ^f are the frictional forces in radial and tangential directions, respectively; $\dot{r}_{b,r}$ and $\dot{r}_{b,\theta}$ are bit velocities in radial and tangent directions, respectively.

4.1.3.4. Mud Damping

When a drill-string moves in viscous drilling mud, the hydraulic damping force can be obtained as [102]

$$\begin{cases} F_r^m = -c_h \sqrt{\dot{r}_{b,r}^2 + \dot{r}_{b,\theta}^2}\, \dot{r}_{b,r} \\ F_\theta^m = -c_h \sqrt{\dot{r}_{b,r}^2 + \dot{r}_{b,\theta}^2}\, \dot{r}_{b,\theta} \end{cases} \tag{4.23}$$

where F_r^m and F_θ^m are mud damping forces in radial and tangential directions, respectively; c_h is the hydrodynamic damping coefficient.

4.1.3.5. Coupling Effect

Because of friction and cutter face inclination, a torsional torque TOB_a given in Eq. (4.16) is produced when the bit is drilling in axial direction. Additionally, the lateral forces also have a moment TOB_l acting on the bit. Accordingly, the final TOB can be represented by

$$TOB = TOB_a + TOB_l + c_v \omega_b \tag{4.24}$$

where c_v is the viscous damping coefficient. The corresponding term accounts for the viscous torque of the mud.

The eccentricity force, mud damping, and lateral friction act on the mass center (*mc* in Figure 4-3) of the BHA, while the bit–rock impact forces act on the collision point; therefore, TOB_l can be written as

$$\begin{cases} TOB_l = F_\theta^{mc} e_0 \cos\left(\phi_b - \varphi_b\right) - F_r^{mc} e_0 \sin\left(\phi_b - \varphi_b\right) + F_\theta^i r_b \\ F_\theta^{mc} = F_\theta^e + F_\theta^m + F_\theta^f \\ F_r^{mc} = F_r^e + F_r^m + F_r^f \end{cases} \tag{4.25}$$

Substituting Eqs. (4.16) and (4.25) into Eq. (4.24), the final TOB can be obtained.

4.2. Numerical Methods

A modeling framework is established combining the six DOF FEM model and the comprehensive boundary condition. This section presents numerical methods to solve the FEM problems. From static analyses, drilling torque and drag can be obtained with average ROP and RPM. In addition, the strain and stress distribution along drill-string and BHA can be obtained to evaluate the structure design. From dynamic analyses, drilling vibrations can be simulated with given operating condition, which provides guidelines for drilling operation.

4.2.1. Static Analysis

For static analysis, drill-string velocity and acceleration are equal to zero. The static equation can be expressed as

$$\left(\left[K_l\right]+\left[K_n\right]\right)\boldsymbol{U} = \boldsymbol{F} - \boldsymbol{R} \tag{4.26}$$

where $\boldsymbol{F}$ and $\boldsymbol{R}$ defined in Eq. (3.70) are external force vector and initial force vector, respectively. Classifying the force vectors into constant component and dependent component, Eq. (4.26) can be rewritten as

$$\left(\left[K_l\right]+\left[K_n\right]\right)\boldsymbol{U}=\boldsymbol{F}_{\text{cons}}+\boldsymbol{F}_{\text{dept}}(\boldsymbol{U}) \tag{4.27}$$

where $\boldsymbol{F}_{\text{cons}}$ is the constant force vector, which includes gravity, hook load, mud buoyancy, and initial force. $\boldsymbol{F}_{\text{dept}}(\boldsymbol{U})$ is the dependent force vector, which includes contact force and friction between drill-string and wellbore. An intuitive way to solve Eq. (4.27) is the fixed-point method, given by

$$\boldsymbol{U}^{i+1}=\left(\left[K_l\right]+\left[K_n\right]\big|_{\boldsymbol{U}=\boldsymbol{U}^i}\right)^{-1}\left[\boldsymbol{F}_{\text{cons}}+\boldsymbol{F}_{\text{dept}}(\boldsymbol{U}^i)\right] \tag{4.28}$$

where the superscript i indicates the iteration number; $\boldsymbol{U}^i$ is the displacement at the i^{th} iteration. The structure displacement is obtained by recursively solving Eq. (4.28) through substituting $\boldsymbol{U}^i$ with $\boldsymbol{U}^{i+1}$ until $\boldsymbol{U}^i$ converges. However, Eq. (4.28) simply takes the contact force $\boldsymbol{F}_{\text{dept}}$ as an external force and does not consider the stiffness from external support; therefore, it diverges when buckling happens.

The recursive form of the Newton-Raphson method [36] is obtained by linearizing $\boldsymbol{F}_{\text{dept}}(\boldsymbol{U})$ around $\boldsymbol{U}^i$, given by

$$\boldsymbol{U}^{i+1}=\boldsymbol{U}^{i}-\left(\left[K_l\right]+\left[K_n\right]\big|_{\boldsymbol{U}=\boldsymbol{U}^i}-\frac{\partial \boldsymbol{F}_{\text{dept}}(\boldsymbol{U})}{\partial \boldsymbol{U}}\bigg|_{\boldsymbol{U}=\boldsymbol{U}^i}\right)^{-1} f_{NR}\left(\boldsymbol{U}^{i}\right) \tag{4.29}$$

$$f_{NR}\left(\boldsymbol{U}^{i}\right)=\left(\left[K_l\right]+\left[K_n\right]\big|_{\boldsymbol{U}=\boldsymbol{U}^i}\right)\boldsymbol{U}^{i}-\boldsymbol{F}_{\text{cons}}-\boldsymbol{F}_{\text{dept}}(\boldsymbol{U}^{i}) \tag{4.30}$$

The nonlinear stiffness $[K_n]$, $f_{NR}(\boldsymbol{U}^{i})$, and the Jacobian of $\boldsymbol{F}_{\text{dept}}(\boldsymbol{U})$ are updated at each iteration. The algorithm stops when the update of $\boldsymbol{U}^{i}$ (defined by $\left\|\boldsymbol{U}^{i+1}-\boldsymbol{U}^{i}\right\|$) is less than a small positive threshold. As we can see from Eq. (4.29), the contact effect is

included in the system stiffness through the term $-\partial \boldsymbol{F}_{\mathbf{dept}}(\boldsymbol{U})/\partial \boldsymbol{U}$. This term can model the increase of system stiffness due to support from the external wall. Even though the structure stiffness $[K_l] + [K_n]$ shows zero or negative eigenvalue and indicates a buckling failure, the eigenvalues of the overall stiffness $[K_l] + [K_n] - \partial \boldsymbol{F}_{\mathbf{dept}}(\boldsymbol{U})/\partial \boldsymbol{U}$ can still be positive. Under this circumstance, the displacement vector $\boldsymbol{U}$ is still able to converge and illustrates the buckling profile.

4.2.2. Dynamic Analysis

Similarly, the force vectors are grouped into constant force $\boldsymbol{F}_{\text{cons}}$ and dependent force $\boldsymbol{F}_{\text{dept}}(\boldsymbol{U}, \dot{\boldsymbol{U}})$ in dynamic analysis, where

$$\left([K_l]+[K_n]\right)\boldsymbol{U}+[D]\dot{\boldsymbol{U}}+[M]\ddot{\boldsymbol{U}}=\boldsymbol{F}_{\text{cons}}+\boldsymbol{F}_{\text{dept}}(\boldsymbol{U},\dot{\boldsymbol{U}}) \tag{4.31}$$

4.2.2.1. Runge-Kutta Method

Taking $\boldsymbol{U}$ and $\dot{\boldsymbol{U}}$ as state variables, Eq. (4.31) can be written as first order differential equation, given by

$$\frac{d}{dt}\begin{bmatrix}\boldsymbol{U}\\ \dot{\boldsymbol{U}}\end{bmatrix}=\begin{bmatrix}[0] & [1]\\ -[M]^{-1}[K] & -[M]^{-1}[D]\end{bmatrix}\begin{bmatrix}\boldsymbol{U}\\ \dot{\boldsymbol{U}}\end{bmatrix}+\begin{bmatrix}\mathbf{0}\\ [M]^{-1}\left(\boldsymbol{F}_{\text{cons}}+\boldsymbol{F}_{\text{dept}}(\boldsymbol{U},\dot{\boldsymbol{U}})\right)\end{bmatrix} \tag{4.32}$$

Based on Eq. (4.32), the state vector $[\boldsymbol{U} \quad \dot{\boldsymbol{U}}]^{\mathrm{T}}$ can be easily updated using Runge-Kutta method. The most widely used Runge-Kutta 4$^{\text{th}}$ order method is formulated in Eq. (4.33)

$$\begin{cases} x_{k+1/2}^{*} = x_k + \dfrac{\Delta t}{2} \cdot f_k \\ x_{k+1/2}^{**} = x_k + \dfrac{\Delta t}{2} \cdot f_{k+1/2}^{*} \\ x_{k+1}^{*} = x_k + \Delta t \cdot f_{k+1/2}^{**} \\ x_{k+1} = x_k + \dfrac{\Delta t}{6}\left[f_k + 2 f_{k+1/2}^{*} + 2 f_{k+1/2}^{**} + f_{k+1}^{*} \right] \end{cases} \tag{4.33}$$

where x is state vector ($[\boldsymbol{U} \quad \dot{\boldsymbol{U}}]^{\mathrm{T}}$ in this case); k is the time step; Δt is the time interval; $f_k = f(x_k, u_k), f_{k+1/2}^{*} = f\left(x_{k+1/2}^{*}, u_k\right),\ f_{k+1/2}^{**} = f\left(x_{k+1/2}^{**}, u_k\right), f_{k+1}^{*} = f(x_{k+1}^{*}, u_k)$ with u_k is the system input at time step k.

4.2.2.2. Central Difference Method

The central difference method approximates the velocity term and the acceleration term using central finite difference, which yields:

$$\dot{\boldsymbol{U}}_{\boldsymbol{k}} = \frac{\boldsymbol{U}_{\boldsymbol{k}+1} - \boldsymbol{U}_{\boldsymbol{k}-1}}{2\Delta t} \tag{4.34}$$

$$\ddot{\boldsymbol{U}}_{\boldsymbol{k}} = \frac{\boldsymbol{U}_{\boldsymbol{k}+1} - 2\boldsymbol{U}_{\boldsymbol{k}} + \boldsymbol{U}_{\boldsymbol{k}-1}}{\left(\Delta t\right)^2} \tag{4.35}$$

where the subscript k denotes the time step; Δt is the time interval. Substituting Eqs. (4.34) and (4.35) back into Eq. (4.31) leads to

$$\left[\hat{K}\right]\boldsymbol{U}_{\boldsymbol{k}+1} = \hat{\boldsymbol{F}} \tag{4.36}$$

with

$$\left[\hat{K}\right] = \frac{1}{\left(\Delta t\right)^2}[M] + \frac{1}{2\Delta t}[D] \tag{4.37}$$

$$\hat{\boldsymbol{F}} = \boldsymbol{F}_{\text{cons}} + \boldsymbol{F}_{\text{dept}}(\boldsymbol{U}_k, \dot{\boldsymbol{U}}_k) - \left([K_l] + [K_n] - \frac{2}{(\Delta t)^2}[M] \right) \boldsymbol{U}_k - \left(\frac{1}{(\Delta t)^2}[M] - \frac{1}{2\Delta t}[D] \right) \boldsymbol{U}_{k-1} \tag{4.38}$$

With Eq. (4.36) and Eqs. (4.34) and (4.35), the system displacement vector, velocity vector, and acceleration vector can be updated at each time step. The central difference method is an explicit method, where the next state is only dependent on current and previous information. To avoid divergence, the time interval Δt must be less than T_0/π, where T_0 is the shortest natural period of the system. In Eq. (4.36), $[\hat{K}]$ is symmetric and positive definite; therefore, using Cholesky decomposition can increase the computational efficiency.

4.2.2.3. Newmark-β Method

The finite difference approximation for Newmark-β method yields:

$$\dot{\boldsymbol{U}}_{k+1} = \dot{\boldsymbol{U}}_k + \Delta t \left[(1-\gamma) \ddot{\boldsymbol{U}}_k + \gamma \ddot{\boldsymbol{U}}_{k+1} \right] \tag{4.39}$$

$$\boldsymbol{U}_{k+1} = \boldsymbol{U}_k + \Delta t \dot{\boldsymbol{U}}_k + (\Delta t)^2 \left[(0.5-\beta) \ddot{\boldsymbol{U}}_k + \beta \ddot{\boldsymbol{U}}_{k+1} \right] \tag{4.40}$$

where γ and β define the acceleration variation over a time interval. For constant acceleration, γ equals to 1/2 and β equals to 1/4. It gives an implicit method, which is unconditionally stable with any Δt. For linear acceleration, γ equals to 1/2 and β equals to 1/6. It gives an explicit method and the stability condition yields $\Delta t < 0.551 T_0$. Reorganizing Eqs. (4.39) and (4.40), the velocity vector and acceleration vector can be expressed as

$$\ddot{\boldsymbol{U}}_{k+1} = \frac{1}{\beta(\Delta t)^2}\left(\boldsymbol{U}_{k+1} - \boldsymbol{U}_k\right) - \frac{1}{\beta\Delta t}\dot{\boldsymbol{U}}_k - \left(\frac{1}{2\beta} - 1\right)\ddot{\boldsymbol{U}}_k \tag{4.41}$$

$$\dot{\boldsymbol{U}}_{k+1} = \frac{\gamma}{\beta\Delta t}\left(\boldsymbol{U}_{k+1} - \boldsymbol{U}_k\right) + \left(1 - \frac{\gamma}{\beta}\right)\dot{\boldsymbol{U}}_k + \Delta t\left(1 - \frac{\gamma}{2\beta}\right)\ddot{\boldsymbol{U}}_k \tag{4.42}$$

Substituting Eqs. (4.41) and (4.42) into Eq. (4.31) yields:

$$\left[\tilde{K}\right]\boldsymbol{U}_{k+1} = \tilde{\boldsymbol{F}} \tag{4.43}$$

with

$$\left[\tilde{K}\right] = \left[K_l\right] + \left[K_n\right] + c_0\left[M\right] + c_1\left[D\right] \tag{4.44}$$

$$\tilde{\boldsymbol{F}} = \boldsymbol{F}_{\text{cons}} + \boldsymbol{F}_{\text{dept}}(\boldsymbol{U}_{k+1}, \dot{\boldsymbol{U}}_{k+1}) + \left[M\right]\left(c_0\boldsymbol{U}_k + c_2\dot{\boldsymbol{U}}_k + c_3\ddot{\boldsymbol{U}}_k\right) + \left[D\right]\left(c_1\boldsymbol{U}_k + c_4\dot{\boldsymbol{U}}_k + c_5\ddot{\boldsymbol{U}}_k\right) \tag{4.45}$$

where $c_0 = \frac{1}{\beta(\Delta t)^2}$, $c_1 = \frac{\gamma}{\beta\Delta t}$, $c_2 = \frac{1}{\beta\Delta t}$, $c_3 = \frac{1}{2\beta} - 1$, $c_4 = \frac{\gamma}{\beta} - 1$, $c_5 = \frac{\Delta t}{2}\left(\frac{\gamma}{\beta} - 2\right)$. Eq. (4.43) is nonlinear and the Newton-Raphson method is implemented to obtain $\boldsymbol{U_{k+1}}$ numerically.

In the proposed FEM model (both straight beam element and curved beam element), the geometric stiffness matrices are included to account for the nonlinear terms of the axial strain, which enables the stability analysis. When a beam is under a compression force that is larger than its buckling threshold, the structure stiffness matrix $[K_l] + [K_n]$ shows zero or negative eigenvalues. According to the analysis in Section 3.4.2, the system becomes unstable under this circumstance. Based on our simulations, the Runge-Kutta method and the central difference method diverge when $[K_l] + [K_n]$ has

zero or negative eigenvalues. However, according to field tests, the drill-string can undertake a significantly higher compression force than the threshold predicted using the eigenvalues of the stiffness matrix because of the support from wellbore wall [103]. In order to accurately describe this phenomenon, a numerical method should be able to model the contact stiffness from wellbore wall. In Eq. (4.29), the contact effect is included in the system stiffness through the term $-\partial \boldsymbol{F}_{\mathbf{dept}}(\boldsymbol{U})/\partial \boldsymbol{U}$. This term models the increase of system stiffness due to support from the external wall. Even though the structure stiffness $[K_l] + [K_n]$ shows zero or negative eigenvalue and indicates a buckling failure, the eigenvalues of the overall stiffness $[K_l] + [K_n] - \partial \boldsymbol{F}_{\mathbf{dept}}(\boldsymbol{U})/\partial \boldsymbol{U}$ can still be positive. Similarly, in Newmark-β method, the contact effect is also included in the system stiffness through $-\partial \boldsymbol{F}_{\mathbf{dept}}(\boldsymbol{U})/\partial \boldsymbol{U}$. Therefore, Newton-Raphson method and Newmark-β method still converge when buckling happens and the post-buckling behaviors of the drill-string can be simulated.

4.3. Simulation and Verification

In Section 3.5, case studies are conducted to verify the developed FEM model. In this section, drill-string/BHA statics and dynamics are simulated using the proposed boundary conditions. The results are compared with commercial software and field observations. The top drive controllers in Section 4.1.1 are also simulated and the results are discussed. Field unit (British unit) is used throughout the simulations.

4.3.1. Static Analysis

4.3.1.1. BHA Strain Stress Distribution

Using the proposed model, static analysis is carried out on a BHA in a directional wellbore, as illustrated in Figure 4-4. The top end of the BHA is fixed (no displacement and rotation); the inclination at bit side is 90 degrees; the build-up rate is 5 degrees per 100 ft; gravity, mud buoyancy, and BHA-wellbore contact force are included in external force. A penalty method is applied to calculate the BHA-wellbore contact force and the results are compared with Ansys in Table 4-1. The shear force, moment, nodal displacement, and bending angle are calculated and compared with Ansys in Figure 4-5. The shear force distribution is also visualized in Figure 4-4 along with BHA geometry. As can be seen from Figure 4-5 and Table 4-1, results of the proposed model agree well with Ansys results. However, the proposed method starts from the central axial of the wellbore and yields a linear formulation; therefore, the computational cost by using the proposed method is significantly reduced compared with Ansys.

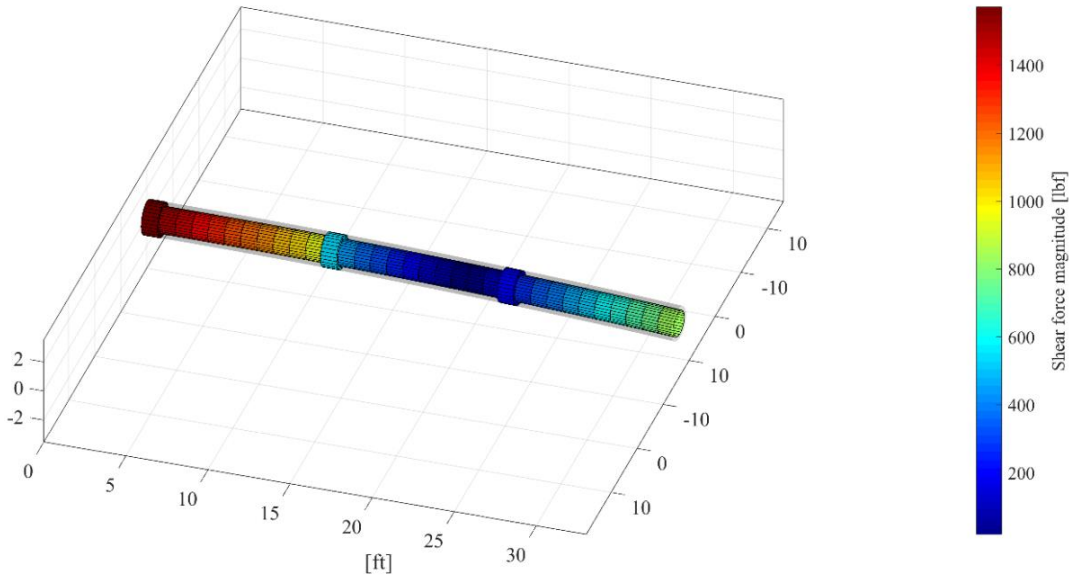

Figure 4-4. BHA geometry and shear force distribution, where the gray color illustrates the wellbore wall

	Proposed model [lbf]	Ansys [lbf]	Error
Bit	1618.0	1613.7	0.27%
First	-332.4	-328.0	1.34%
Second	0	0	0%
Top End	852.6	851.1	0.18%

Table 4-1. Comparison between proposed method and Ansys

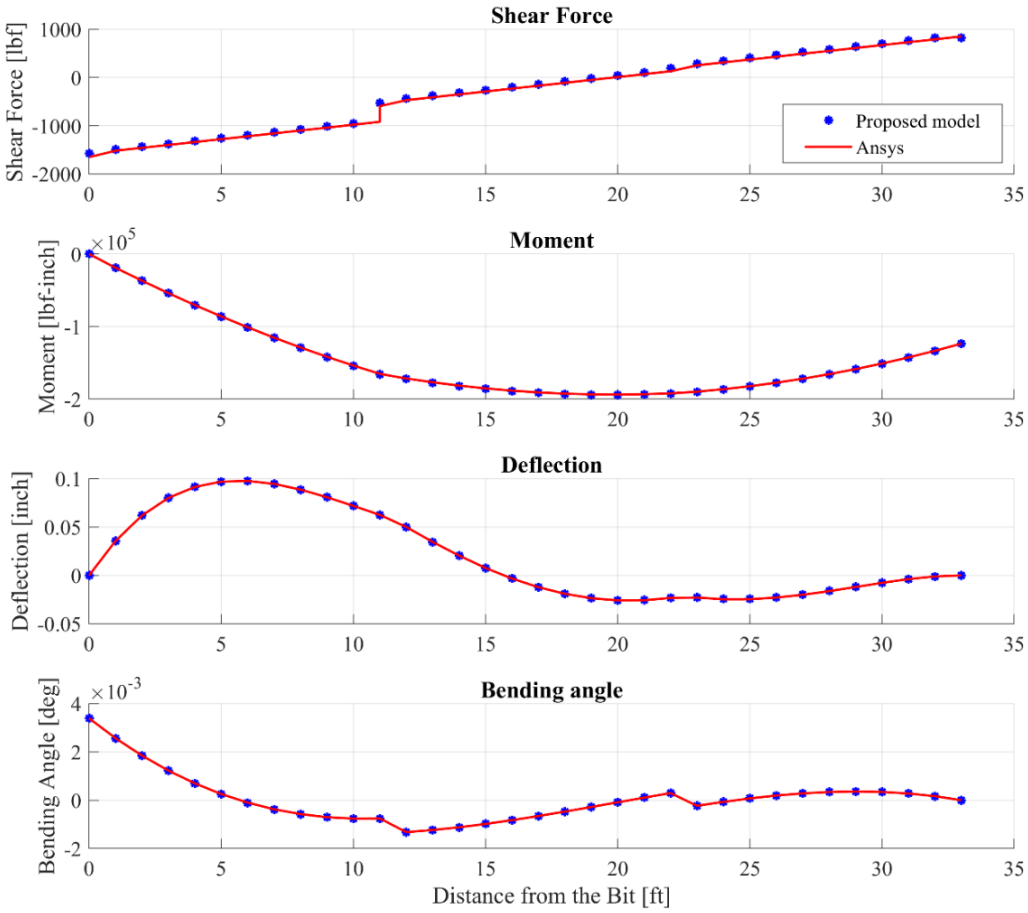

Figure 4-5. Distribution of shear force, moment, displacement, and bending angles along the BHA where the deflection and bending angles are relative to the wellbore

4.3.1.2. Torque and Drag Analysis

The drag and torque of directional drilling is very significant. If not properly evaluated, it can result stuck pipe and cause drill-string failure. In well planning process,

small drag and torque is preferred to reduce the energy consumption. Based on the analysis discussed in Section 4.2.1, torque and drag can be calculated with given drill-string, well trajectory, and operating parameters. The result can be used for well trajectory pre-planning, and real-time drag and torque evaluation. In this simulation, a real drilling case is evaluated. The well trajectory is given in Table 2-1 and illustrated in Figure 2-5. The BHA profile is illustrated in Figure 4-6. Some other parameters for simulation are listed in Table 4-2. The simulation result is illustrated in Figure 4-7, where contact force, drag, and torque are calculated against measured depth.

Parameter	Value
Static WOB	10000 [lbf]
Static TOB	1.27×10^5 [lbf-in]
Average ROP	100 [ft/h]
Average RPM	200 [rpm]
Rock stiffness	500M [lbf/ft]
Friction coefficient	0.6
Well diameter	8.1 [inch]
Note: the input rock stiffness, friction coefficient, and well diameter can change with measured depth. A uniform value is used only in this simulation.	

Table 4-2. Simulation parameter

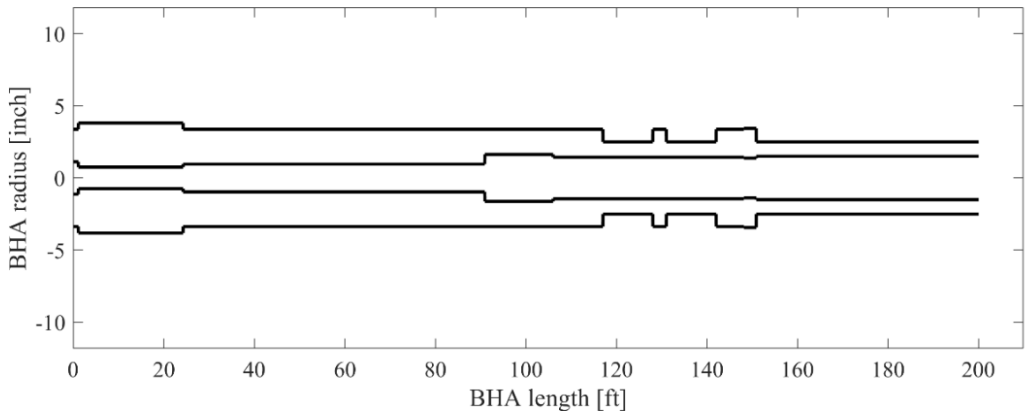

Figure 4-6. BHA geometry

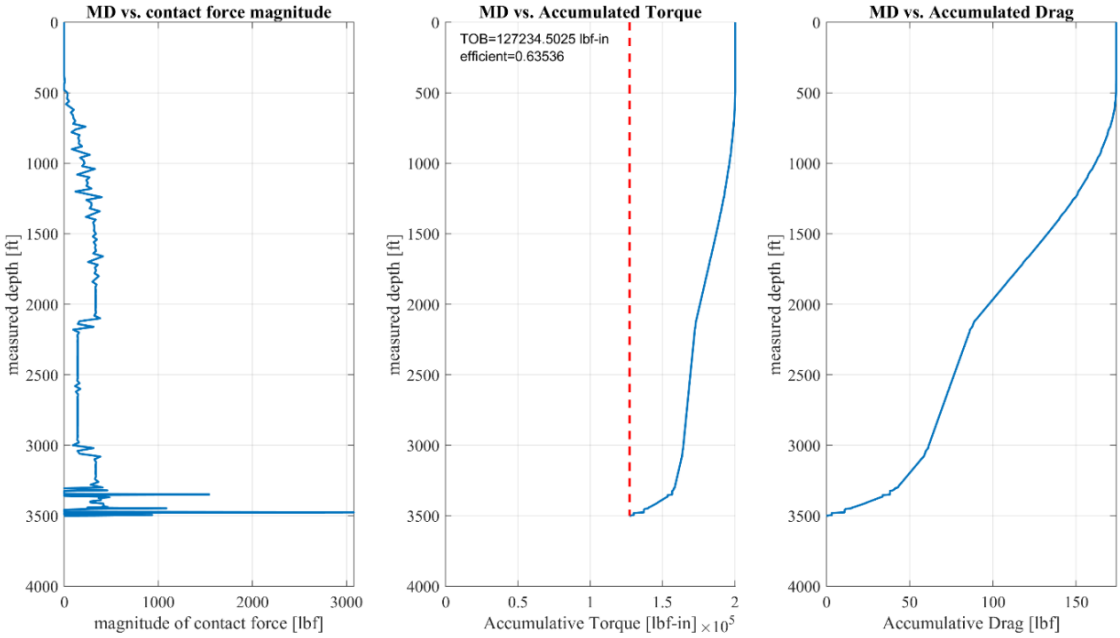

Figure 4-7. Contact force, drag, and torque against well MD

4.3.1.3. Drill-string Stress Distribution

In Section 4.3.1.2, the torque and drag are obtained through static analysis. The stress distribution of the drill-string can also be obtained from the same simulation. Based on the simulation results, proper actions can be taken to avoid stress concentration and prevent drill-string failure. A directional drilling case is simulated, where the well trajectory and the BHA profile are the same as Section 4.3.1.2. The top drive of the drill-string is clamped, the TOB is zero and the WOB is set at 30000 lbf. The gray tube illustrates the boundary of wellbore wall. The linear stiffness (without geometric stiffness matrix $[K_n]$) is first applied for static analysis, and the result is illustrated in Figure 4-8. The simulation converges with both Eq. (4.28) and Eq. (4.29). However, drill-string post-buckling information cannot be obtained with only linear stiffness. In the second simulation, the geometric stiffness is included for static analysis. Eq. (4.28) fails to

converge as the additional stiffness from wellbore support is not properly modeled. Eq. (4.29) converges by involving the stiffness from wellbore support. The drill-string undergoes spiral buckling as illustrated in Figure 4-9. This result agrees well with experiments and field observations [104].

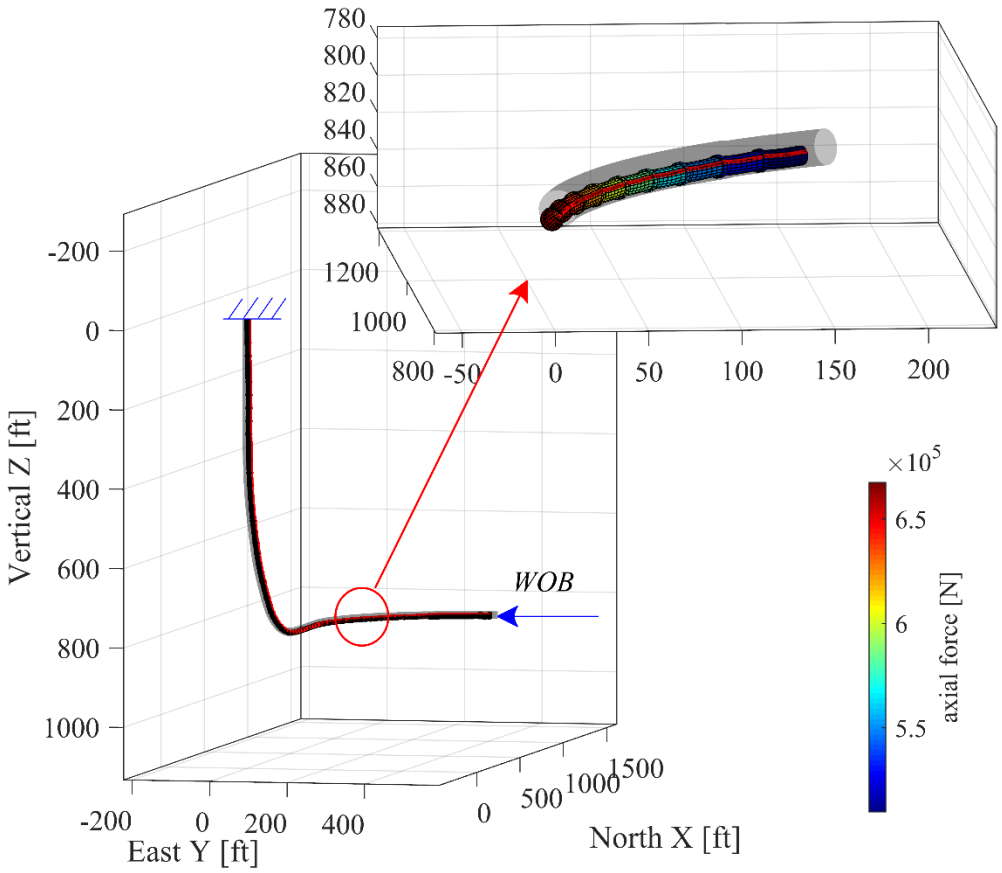

Figure 4-8. Directional drilling simulation with linear stiffness (The diameters of the well and the drillstring are enlarged by 40 times for illustration).

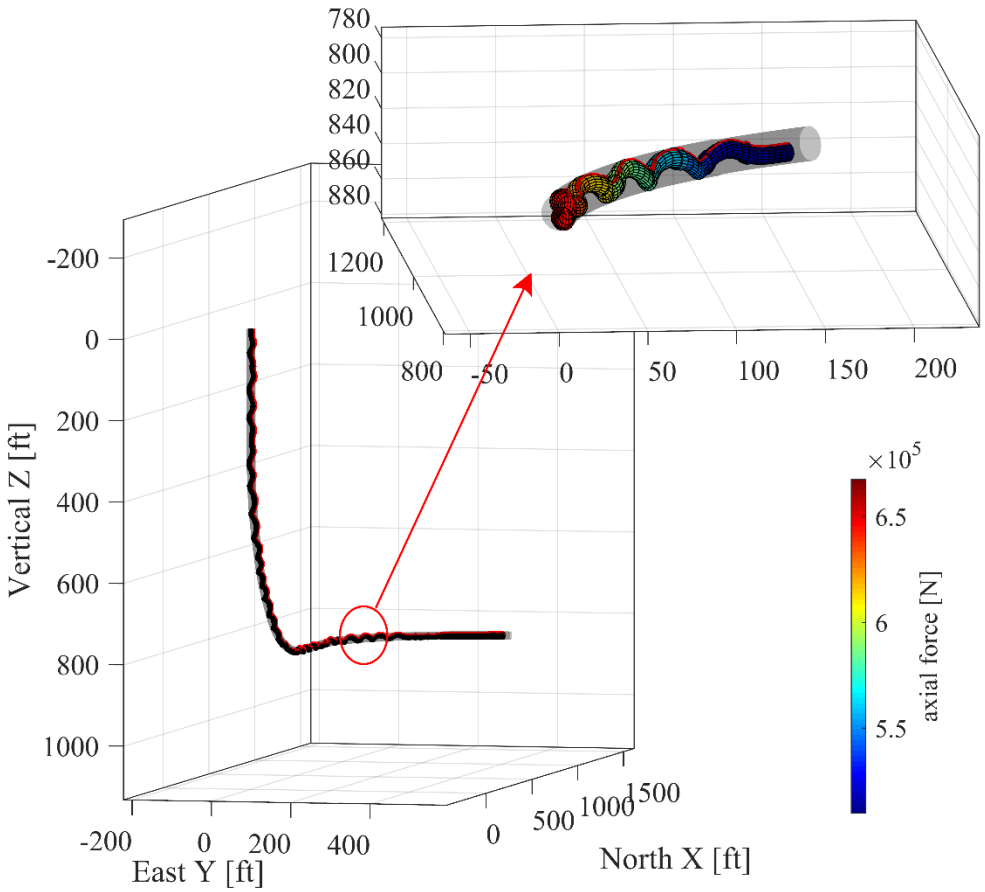

Figure 4-9. Directional drilling simulation with nonlinear stiffness (The diameters of the well and the drill-string are enlarged by 40 times for illustration).

4.3.2. Dynamic Analysis

In this section, realistic drilling scenarios are simulated using the comprehensive boundary condition developed in this chapter. Bit vibrations can manifest in axial, torsional, and lateral directions and cause these phenomena, known as bounce back, stick-slip, and whirl. Usually, these vibrations are related to the applied WOB, rotary speed, and rock properties. For heavy WOB and low rotary speeds, stick-slip is more likely to occur; for high rotary speeds, whirl is prone to dominate [65]; and bounce back rarely occurs for PDC bits. In this section, different scenarios are simulated by changing

the rotary speed, static WOB (through changing hook load), rock stiffness, and BHA eccentricity, and then these vibrations are excited. Three cases are presented and discussed.

4.3.2.1. Normal Operation

Drill-string parameters and rock properties for the first two scenarios are listed in Table 4-3. The directional well trajectory is illustrated in Figure 4-10, where the top drive locates at position $[0\ 0\ 0]^{\mathrm{T}}$ and the bit locates at position $[6016ft\ 1684ft\ 6052ft]^{\mathrm{T}}$. When setting the static WOB and the rotary speed at proper values, the drilling system is able to operate smoothly without manifesting stick-slip or whirl. In the first scenario, the rotary speed is set at 76.4 rpm (8 rad/s) and the drill-string works normally with no detrimental vibrations. Figure 4-11 shows the torsional speeds of the top drive and the bit, and Figure 4-12, shows the bit dynamics in three-dimensional directions. All the results are illustrated under the local coordinate, which takes the well's central axis as the reference.

Drill-string		Bit and rock	
Drill-pipe length	9613 [ft]	Bit diameter	7.87 [inch]
Drill-pipe outer	4 [inch]	Bit gauge	3.93 [inch]
Drill-pipe inner	3.3 [inch]	Rock specific	21755 [psi]
Drill collar	229 [ft]	Rock contact	29007 [psi]
Drill collar outer	7.75 [inch]	Wellbore	8.27 [inch]
Drill collar inner	3 [inch]	Static WOB	20000 [lbf]

Table 4-3. Values of drill-string and well parameters

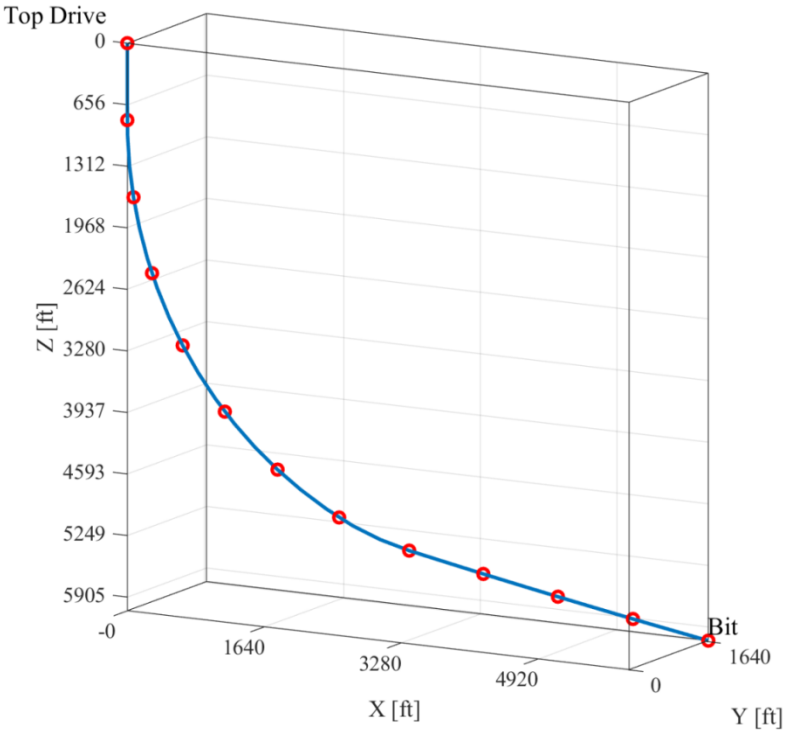

Figure 4-10. Well trajectory under simulation

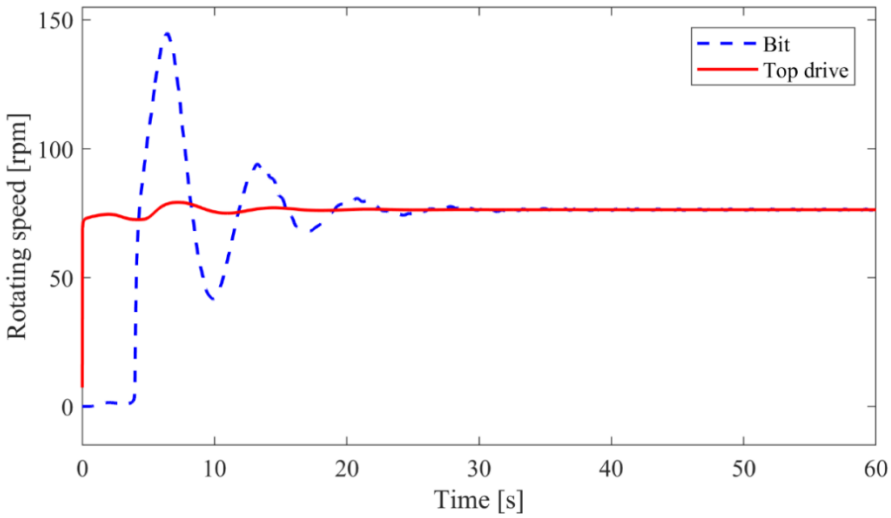

Figure 4-11. Torsional speeds of the top drive and the bit under normal operation

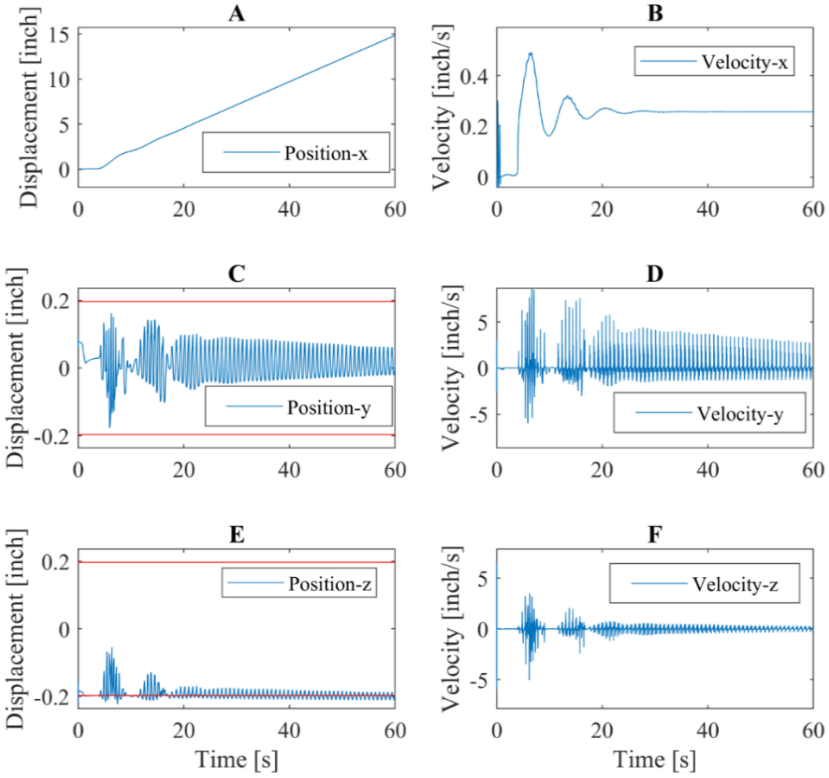

Figure 4-12. Bit dynamics (normal operation) under local coordinate, where A, C, and E are the bit displacements in *x* (axial), *y* (lateral), and *z* (lateral) directions; B, D, and F are bit velocities in *x*, *y*, and *z* directions

As can be concluded from Figure 4-11, when the top drive begins to the bit remains still, restricted by the external torque from the rock. As the phase difference continues to increase, the driving torque finally overcomes the static TOB and the bit begins to rotate. According to the bit-rock interaction law, either by Detournay's experiment model [98][99] or the Karnopp friction model [105], when the rotary speed is low, the TOB can decrease with the increase of bit speed. Consequently, the strain energy stored by the drill-string/BHA can quickly release, which rotates the BHA aggressively and forms an overshoot. After several minor oscillations, the driving torque and the dynamic TOB reach an equilibrium and the bit rotary speed stabilizes to the set point.

Comparing Figure 4-11 and Figure 4-12B, because the bit rotates continuously, it drills down with a relatively constant ROP. In lateral direction, because of the profile of the drill-string, the bit lays down on the wellbore under the influence of gravity. Correspondingly, the displacement can have some offset. According to Table 4-3, the gap between the bit and the wellbore is 0.2 inch, which agrees with the simulated value shown in Figure 4-12C and Figure 4-12E. The simulated displacement is slightly larger than the gap because the bit can occasionally cut into the wellbore, which also results in these high-frequency lateral oscillations illustrated in Figure 4-12C, D, E, and F.

4.3.2.2. Stick-Slip

In the second scenario, a stick-slip vibration is triggered by reducing the rotary speed to 47.7 rpm (5 rad/s) while keeping the other parameters constant, and the corresponding results are illustrated in Figure 4-13 and Figure 4-14. As indicated in Figure 4-13, instead of stabilizing to the set point, the bit rotary speed oscillates periodically between 0 and twice the set point. The stick-slip vibration can decrease the ROP, twist off the connection joint, and damage the drill bit and therefore, has drawn extensive investigations [24][50]. Based on the observation, during stick phase, the driving torque is less than the static TOB and continues to increase with increased phase difference. When the static TOB and driving torque both reach their maximum values, the bit begins to rotate and the TOB quickly drops below the driving torque; then, the bit accelerates and comes to the slip phase. With decreased phase difference, the driving torque falls below the TOB when the bit begins to decelerate and finally stops. Comparing Figure 4-13 and Figure 4-14B, it can be concluded that, during the slip phase,

the bit can crush the rock more aggressively, resulting in an increased ROP; however, during the stick phase, the ROP slows down and even vanishes.

The coupling mechanism between the torsional and lateral vibrations can be distinctly expressed by Figure 4-13 and Figure 4-14C, D, E, and F. During the slip phase, the high rotary speed can induce large inertial forces (e.g., centrifugal force) with the presence of BHA eccentricity. These forces can push the bit gauge to cut into the wellbore (In Figure 4-14E, the blue trajectory can go beyond the red wellbore), which causes high-frequency lateral vibrations through bit-rock interaction. During the stick phase, since the bit is not rotating, the cutting behavior stops as well; therefore, in axial direction, the ROP slows down (Figure 4-14B); and in lateral directions, the bit remains stable without lateral cutting. The severity of lateral vibrations is determined by the formation property. If the rock has large coefficient of restitution, the system will be lightly damped and a severe lateral vibration will occur. Vice versa, if the rock has small coefficient of restitution, the lateral vibration will be less severe. Similar to the last scenario, the bit has an offset of 0.5 mm.

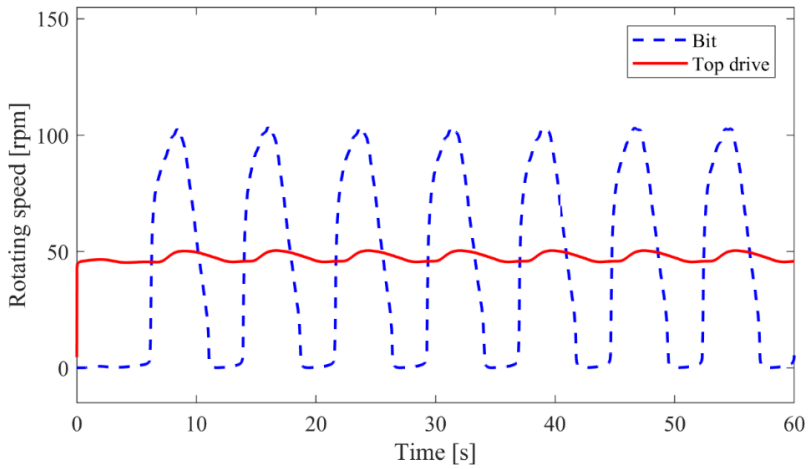

Figure 4-13. Torsional speeds of the top drive and the bit under stick-slip vibration

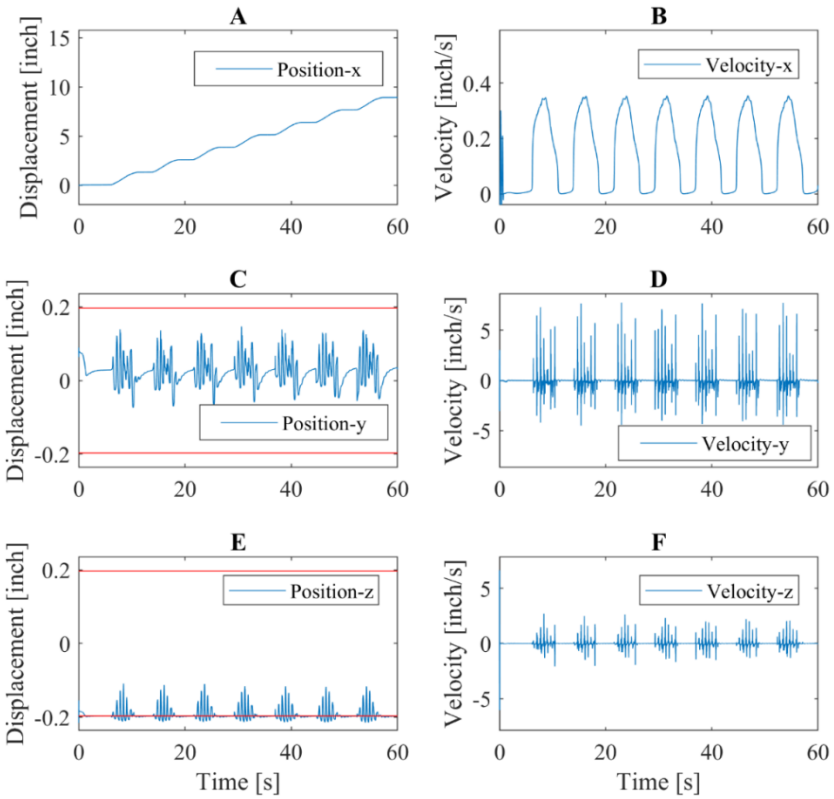

Figure 4-14. Bit dynamics (stick-slip) under local coordinate, where A, C, and E are the bit displacements in *x* (axial), *y* (lateral), and *z* (lateral) directions; B, D, and F are bit velocities in *x*, *y*, and *z* directions

4.3.2.3. Whirl

A vertical well is analyzed to simulate whirl vibration. The eccentricity is increased from 2 mm to 10 mm to trigger a large lateral force. The results are illustrated in Figure 4-15, Figure 4-16, and Figure 4-17, where the bit rolls around the wellbore aggressively. More drilling scenarios are provided in [26][80].

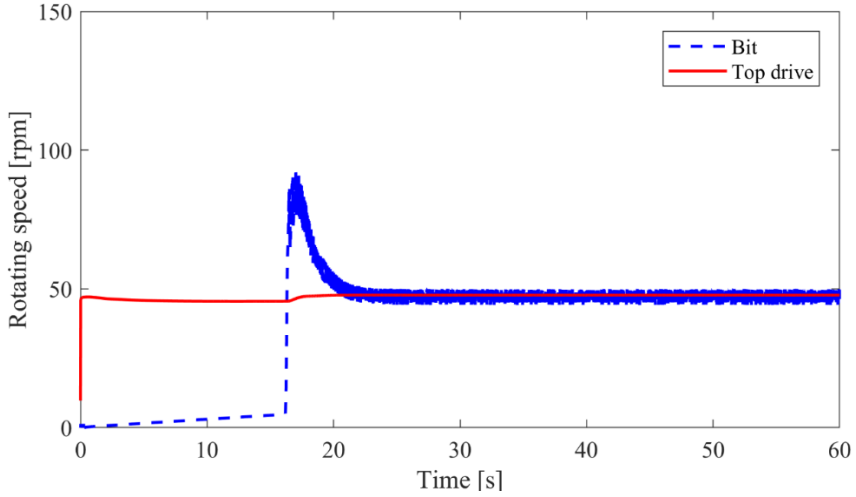

Figure 4-15. Torsional speeds of the top drive and the bit under whirl vibration

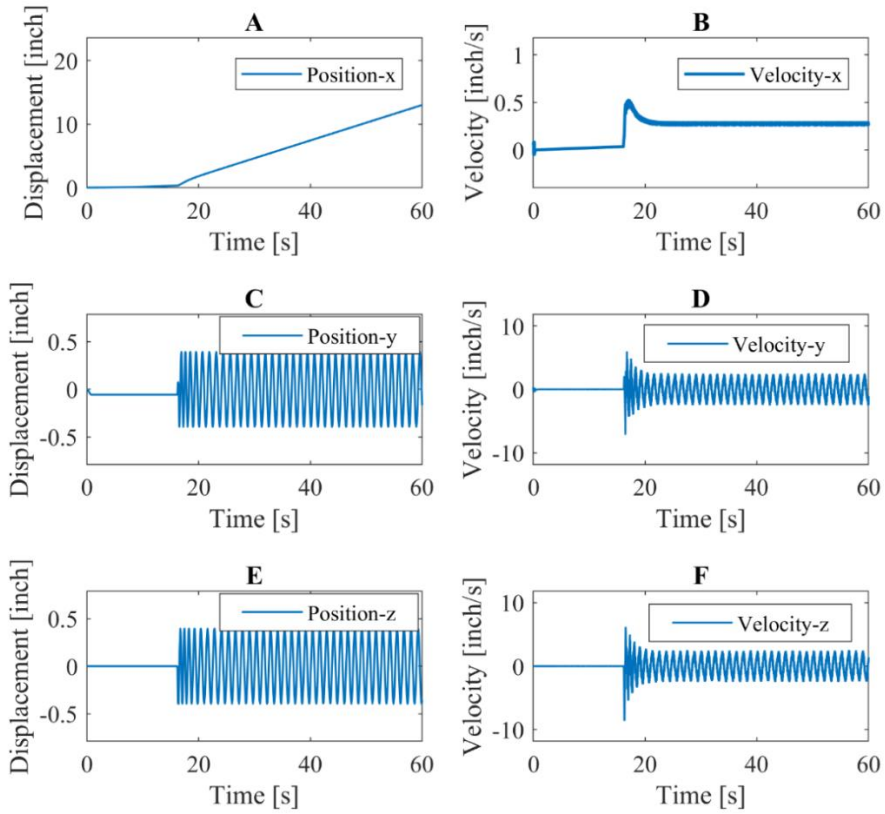

Figure 4-16. Bit dynamics (whirl) under local coordinate, where A, C, and E are the bit displacements in *x* (axial), *y* (lateral), and *z* (lateral) directions; B, D, and F are bit velocities in *x*, *y*, and *z* directions

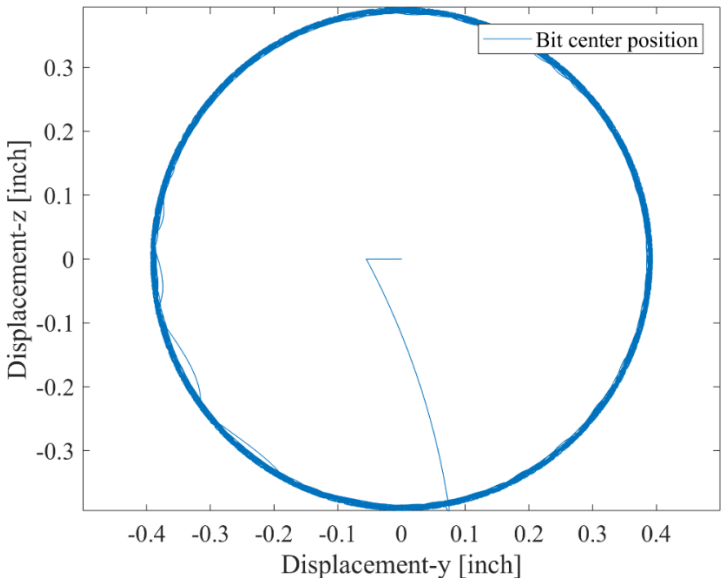

Figure 4-17. Bit center movement

Videos of the proposed drill-string model can be found online.

1. Normal: https://www.youtube.com/watch?time_continue=1&v=ylsuEkWnwfM
2. Stick-slip vibration: https://www.youtube.com/watch?v=VujPR33kyuo
3. Lateral vibration: https://www.youtube.com/watch?v=ZdPEqrgQx84

4.3.3. Stick-Slip Vibration and Top Drive Controllers

In Section 4.1.1, top drive controllers are applied as torsional boundary conditions. Among these controllers, the soft speed controller and the soft torque controller are well accepted and have achieved commercialization. This section studies stick-slip vibrations and compares these controllers in suppressing stick-slip vibrations. In these simulations, the length of the directional drill-string is 2000 ft. The static WOB is 20000 lbf. And the setpoint of the rotary speed is 50 rpm. A regular PI controller is firstly applied, where K_P equals to 15000 and K_I equals to 30000. As illustrated in Figure 4-18, stick-slip happens

under this PI controller, where the bit speed fluctuates between zero and 100 rpm. A fast Fourier transform is conducted on bit speed and top drive torque. The results are illustrated in Figure 4-19. The vibration frequency is at 1.1 Hz, which is the lowest natural frequency of the drill-string (1.1698 Hz). Stick-slip vibration is usually measured from downhole. However, due to the limitation of telemetry system, the information sent up has a very low resolution. According to Figure 4-19, the top drive torque has the same vibration pattern as the bit speed when stick-slip happens. Therefore, it is possible to use top drive torque to indicate stick-slip vibrations. As a benefit, the data resolution will not be limited by telemetry bit rate.

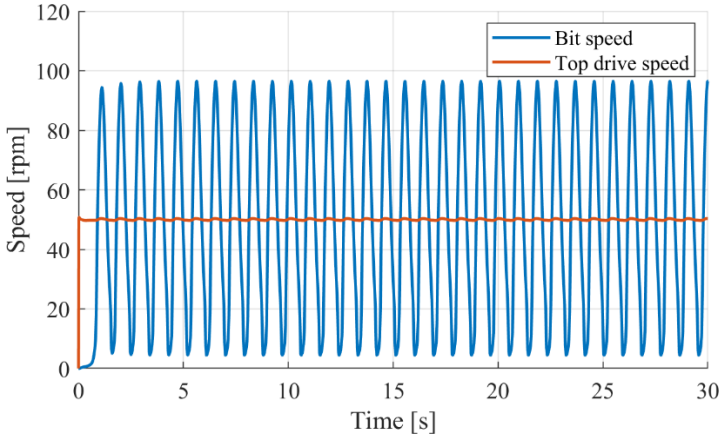

Figure 4-18. Regular PI controller

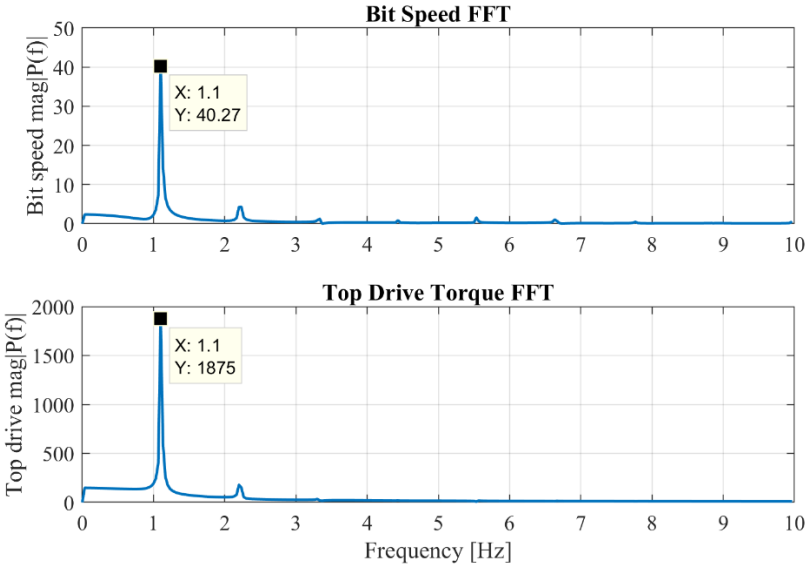

Figure 4-19. FFT of bit speed and top drive torque

The soft speed method is implemented. Taking f_n equal to 1.1 Hz into Eq. (4.4), K_I is calculated which is 1433. In the simulations of Figure 4-20, different values are assigned to the proportional gain K_P. A small K_P results to a small reflection rate; therefore, suppresses stick-slip vibrations more effectively. However, based on the simulation results, when K_P is too small (e.g., 200), the controller is unable to keep top drive speed constant when torsional waves hit the top drive. As a result, both bit speed and top drive speed fluctuate significantly. Setting K_P equal to 300, the top drive speed still has a large fluctuation at the beginning but soon converges to the setpoint. When K_P equals to 1000, the soft speed controller works well, effectively suppressing stick-slip vibrations. A large K_P causes a large reflection rate of torsional waves. In this case, when increasing K_P to 2000, the soft speed controller fails to mitigate stick-slip vibrations.

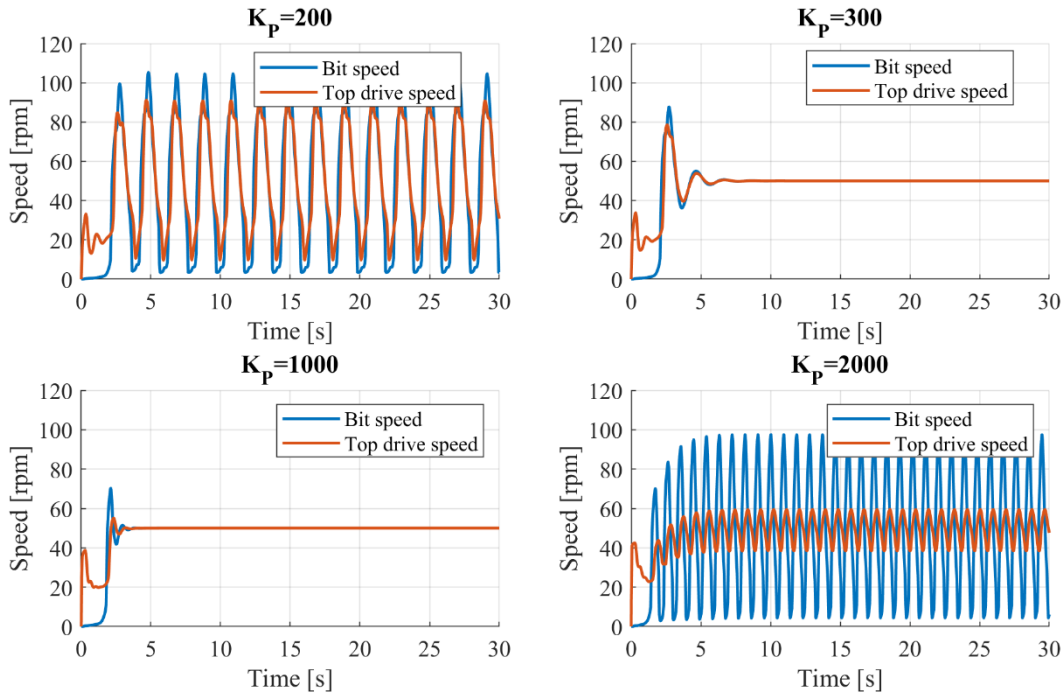

Figure 4-20. Soft speed control

Figure 4-21 shows the simulation results of several soft torque controllers, where K_P equals to 15000 and K_I equals to 30000 (K_P and K_I are the same as the speed PI controller presented earlier). The feedback coefficients (H_0 in Eq. (4.6)) of these soft torque controllers are $10/K_P$, $15/K_P$, $25/K_P$, and $40/K_P$, respectively. With a small H_0, less torque fluctuation is eliminated from top drive torque and it is less likely to suppress the stick-slip vibration. However, if the value of H_0 is too large (e.g., $40/K_P$ in Figure 4-21), it takes long time for the system to reach the setpoint. Therefore, a key point of applying soft torque controller is to tune H_0 based on the severity of stick-slip vibration.

It is well observed that a high WOB can exacerbate stick-slip vibrations. Based on simulations using the proposed FEM modeling framework. When WOB exceeds some threshold, both soft torque method and soft speed method fail to suppress the stick-slip

vibrations. In next chapter, a method is proposed to optimize the BHA structure such that the BHA itself is resilient against vibration.

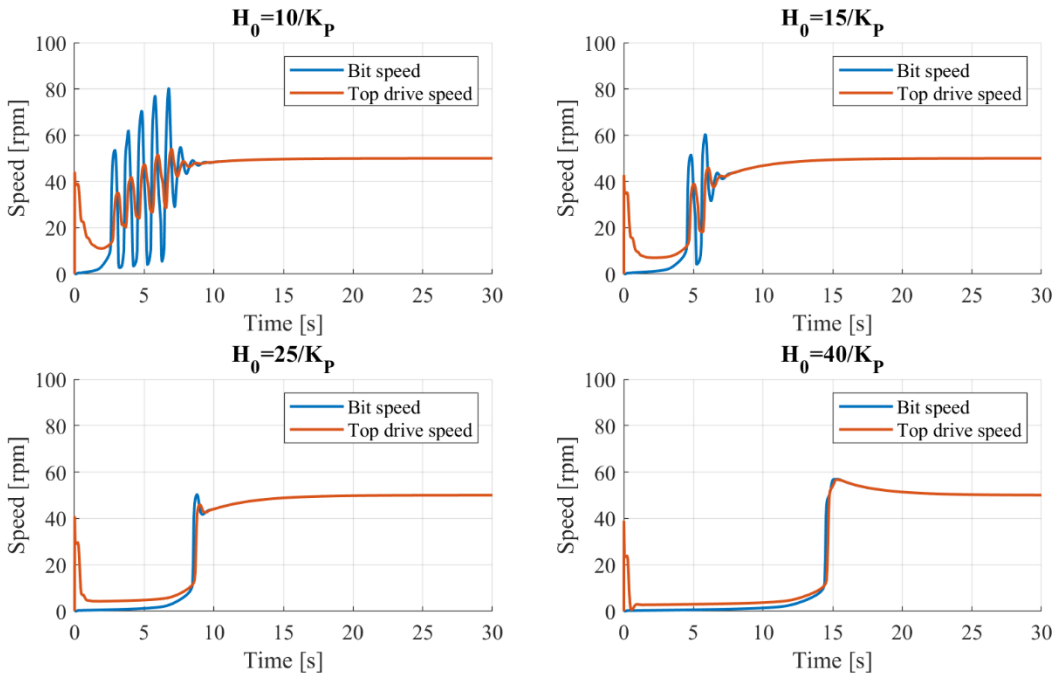

Figure 4-21. Soft torque controllers

4.4. Summary

In this chapter, the boundary conditions for directional drillings are developed, which include models for the top drive and the draw-works, a model for drill-string and wellbore contact, and a model for bit forces. By combining the FEM models and the boundary conditions, a comprehensive modeling framework is established for directional drillings. Numerical methods are also presented for static and dynamic analyses. In developing the finite elements, the higher order terms of the axial strain are included to get the geometric stiffness matrices so the buckling failure can be described. The numerical methods presented in this chapter consider the support from wellbore well and

therefore, can simulate post-buckling profiles of the drill-string when buckling happens. From static analyses, torque and drag can be calculated to prevent drilling failure. The strain and stress distributions along the drill-string can also be obtained to avoid stress concentration. From dynamic analyses, the normal drilling scenarios, the stick-slip vibrations, and the whirling vibrations are simulated using the proposed FEM modeling framework. The top drive controllers also are incorporated as torsional boundary conditions. The guidelines for tuning the control parameters are obtained from dynamic simulations.

Chapter 5. BHA CONFIGURATION OPTIMIZATION

In Chapter 3 and Chapter 4, an FEM modeling framework is established to describe directional drilling dynamics. Top drive controllers are also studied to reduce drilling vibrations. Based on the FEM model, this chapter proposes a framework to optimize the design of the BHA structure such that the BHA itself is resilient against vibration.

5.1. Problem Introduction

Mitigation of drilling vibration has presented significant challenges to the drilling industry. In Section 1.5, passive and active methods are introduced to reduce drilling vibration. The soft speed method and the soft torque method presented in Section 4.1.1 are typical active methods. These top drive controllers rely on surface measurements that normally possess a large time delay. Also, both methods have limited mitigation capabilities. When WOB and TOB exceed some threshold values, these top drive controllers will fail. Also, recent efforts have been made toward developing downhole controllers. However, this task has proven difficult because of the lack of downhole actuators and has found its application limited to just research. One way to overcome these deficiencies occurring in the operation stage is to address the problem during the design stage by optimizing the design of a BHA to minimize undesirable downhole vibrations. Redesigning the BHA structure is a passive method of reducing drilling

Part of this chapter was published in: 1. Feng, T., Bakshi, S. Gu, Q. Chen, D. Design Optimization of Bottom-Hole Assembly to Reduce Drilling Vibration. *Journal of Petroleum Science and Engineering.*
The author contributes to formulate drill-string FEM model and design GA to optimize BHA structure

vibrations. Passive methods and active methods can effect the dynamics independently or they can work simultaneously to reduce drilling vibrations more effectively.

We choose to optimize BHA design rather than the other components as the BHA is the most important drilling device. Several methods have been proposed on BHA design to mitigate drilling vibrations. In [64], Dareing et. al. formulated BHA natural frequencies as functions of BHA length and proposed to increase BHA length to avoid resonance and thus reduce drilling vibrations. However, in order to achieve the desirable natural frequency, the redesigned BHA needs to be much longer than the original design which has the undesirable effect of increasing drilling friction. In [62][63], BHA antistall tools were invented, which use spring or hydraulic oil to damp out the downhole vibrations. However, these antistall tools are expensive and subject to damage under vibration, which limits their application. In a series of work from ExxonMobil [45][46], Bailey et. al. redesigned the BHA structure to reduce drilling vibrations. The BHA lateral dynamics are formulated using a lumped beam model, and the BHA performance is evaluated using indices such as the BHA strain energy and stabilizer side force. According to field tests, BHAs with less strain energy and stabilizer side force show less mechanical specific energy (MSE), higher ROP, and less vibration; therefore, these indices prove to be effective in evaluating BHA dynamic performance. The method developed in [45][46] can provide a comparison mechanism among multiple BHAs. However, it does not deal with the problem of optimizing BHA structure to achieve the best dynamic performance.

This chapter proposes a systematic way of optimizing stabilizer locations along a BHA for vibration mitigation. Firstly, the internal stress of the BHA as well as the contact force of the stabilizers are calculated based on the high-fidelity FEM model. Then, indices, such as the BHA strain energy and the stabilizer side force, are derived to evaluate BHA vibration. The stabilizer positions influence these indices through changing the boundary conditions. Therefore, determining stabilizer positions to reduce drilling vibrations can be formulated as an optimization problem which minimizes BHA indices over the operational range. The cost function is nonconvex within the feasible domain and cannot be expressed explicitly in terms of stabilizer positions. To deal with this problem, the derivative-free genetic algorithm (GA) is selected to solve the nonconvex problem, utilizing parallel computations to expedite the solution process.

5.2. BHA Vibration Index

BHA performance can be quantified using vibration indices, such as the BHA strain energy and the stabilizer side force [45][46]. These indices are calculated under the steady state dynamics of a BHA. Based on statistical studies, it is found that the BHA with less index value exhibits less MSE, higher ROP, and less vibration [46]. For the convenience of comparing BHAs with different length, the normalized BHA strain energy is proposed, given by

$$SE = \frac{1}{L}\sum_{i=1}^{N}\frac{M_i^2 l_i}{2(EI)_i} \tag{5.1}$$

where L is the length of the BHA; N is the number of finite elements to mesh the BHA; l_i is the length of the i^{th} element; and M_i is the bending moment of the i^{th} element. In Eq. (5.1), L, E, and I are determined with given BHA; l_i is determined after meshing the BHA; while the internal bending moment M_i needs to be calculated from the BHA deformation. For a given element, the internal force vector can be obtained by

$$\boldsymbol{f_{int}} = \left(\left[k_{e,l}\right] + \left[k_{e,n}\right]\right)\boldsymbol{u_e} \tag{5.2}$$

where $\boldsymbol{f_{int}}$ is the internal force vector; and $\boldsymbol{u_e}$ is the displacement vector of an element under its local coordinate, which can be transformed from the global coordinate after obtaining the global displacement vector $\boldsymbol{U}$.

The internal axial force, shear force, and bending moment are components of $\boldsymbol{f_{int}}$. The stabilizer side force can be determined from the change of internal shear forces at the stabilizer, given by

$$SF^k = f_{y,i+1}^k - f_{y,i}^k \tag{5.3}$$

where k is the node number; i and $i+1$ are element numbers. In this case, node k is shared by elements i and $i+1$; SF^k is the side force of the stabilizer located at node k; $f_{y,i}^k$ is the internal shear force of node k obtained from element i; and $f_{y,i+1}^k$ is the internal shear force of node k obtained from element $i+1$.

The BHA index values are calculated under different RPM conditions, uniformly distributed within an operating interval (typically 50-200 rpm). The distribution of RPM values can also be user-defined when pre-knowledge of the operating RPM range is

available. To obtain good dynamic performance over the whole operating range, the sum of squares of the index value at each RPM value is calculated as the cost function

$$J = \sum_{i=1}^{W} VI_{\omega_i}{}^2 \tag{5.4}$$

where W is the number of distinct RPM values; and VI_{ω_i} is the index value under ω_i.

The cost function defined in Eq. (5.4) is to be minimized by optimizing the positions of the stabilizers. The mechanism of this optimization is to modify BHA natural frequencies and move them away from the operating RRM to avoid resonance. The stabilizers can modify the natural frequencies of a BHA through changing the contact boundaries. Another method to vary the BHA natural frequency is to increase the BHA length [64]. However, it may cause the BHA to be over-weight. Optimizing stabilizer positions is free from this problem and involves minimal change to the existing BHA structure. The BHA strain energy has the highest covariance with drilling MSE [46]; therefore, is selected by this research as the index value to be minimized. In addition, indices like the BHA strain energy, the stabilizer side force, the transmitted strain energy and the end point curvature are positively correlated with each other. If one index value is minimized, the other index values will decrease simultaneously.

5.3. Genetic Algorithm Optimization

Based on formula in Eq. (5.4), the index value over the whole operating RPM is to be minimized by relocating stabilizer positions, given by

$$\min J = \sum_{i=1}^{W} VI_{\omega_i}(\boldsymbol{s})^2,\ \boldsymbol{s} = [s_1 \quad s_2 \quad \ldots \quad s_l]$$
$$s.t.\ 0 < s_1 < s_2 \cdots < s_{l-1} < s_l < L \tag{5.5}$$

where s_1, s_2, s_{l-1}, and s_l are positions of the first, second, $(l-1)^{th}$, and l^{th} stabilizers, respectively; and L is the length of the BHA.

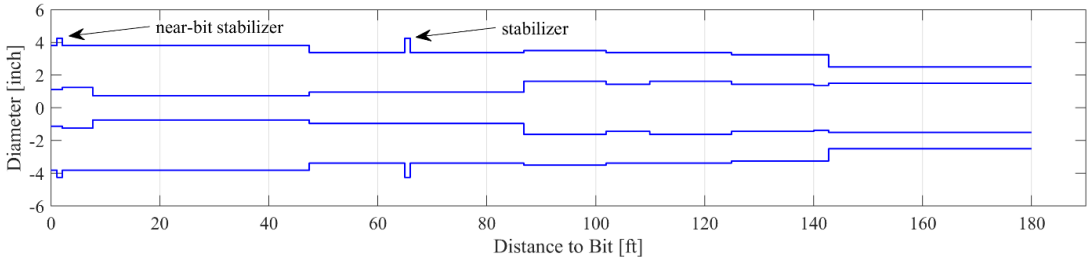

Figure 5-1. BHA for optimization

As an example, the BHA given in Figure 5-1 is studied, where the left end is the bit and the right end is the heavy wall drill-pipe (HWDP, the top of BHA). There are two stabilizers all together. The position of the near-bit stabilizer (the left one) is fixed while the position of the other stabilizer (the right one) can be changed to optimize the dynamic performance of the BHA. New designs are obtained by shifting the right stabilizer in Figure 5-1 from the bit side to the HWDP side along the BHA. The cost function values are calculated at each configuration and the results are illustrated in Figure 5-2, where the *x* axis denotes the distance of the right stabilizer to the bit and the *y* axis shows the natural logarithm (ln) of the cost function for a better comparison.

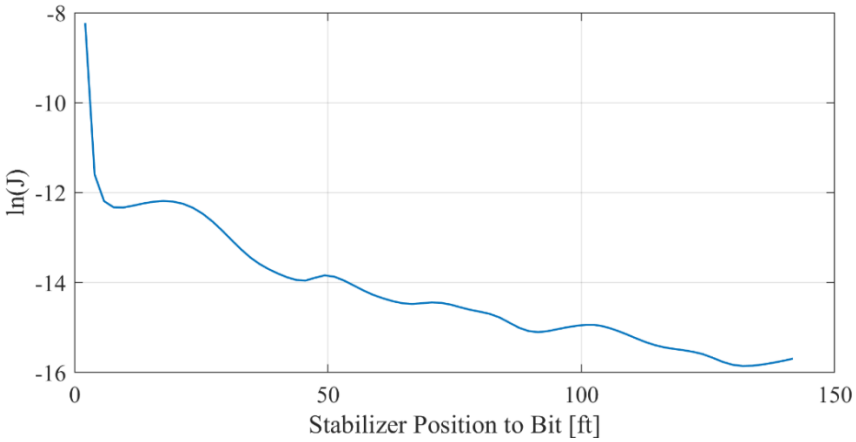

Figure 5-2. Cost function vs. stabilizer position

As can be concluded from Figure 5-2, the cost function is non-convex in the feasible area. In addition, it is almost impossible to write BHA strain energy as explicit functions of the stabilizer positions. Accordingly, derivative-based optimization methods, like the gradient method and Newton's method, cannot handle the proposed problem. Based on Section 5.2, the BHA index values can be conveniently calculated from FEM simulations; therefore, the derivative-free simulation-based optimization methods can be applied to minimize Eq. (5.5). GA [106] is such a method which has been widely used in optimizing mechanical design for vibration suppression.

5.3.1. Genetic Algorithm Introduction

In this chapter, the GA is implemented to determine the stabilizer positions by solving the optimization problem. The GA is a heuristic search method, where the searching process of the optimal solution imitates the biological evolution process [107]. To apply the GA, a population is generated which initializes the searching pool. The individuals inside the population are solutions to the problem. Based on the principle of

"survival of the fittest", a better solution is assigned with a higher probability to be kept. Through conducting fitness selection, crossover, mutation and elitism, the population evolves at each generation and gets closer to the optimal solution. The flow chart of the optimization framework is illustrated in Figure 5-3, which integrates the GA optimization and FEM simulation.

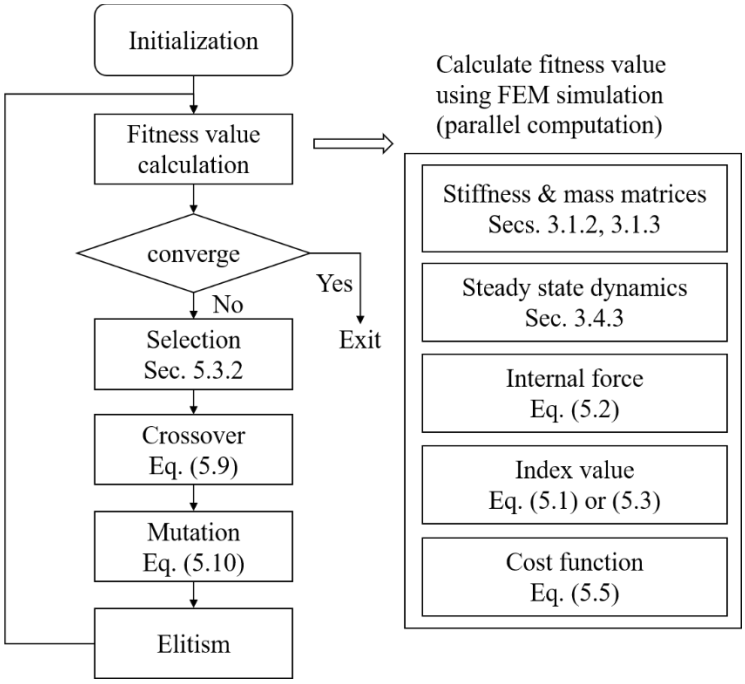

Figure 5-3. Genetic algorithm flow chart

5.3.2. Fitness Function and Selection

The value of the fitness function quantifies the optimality of a solution. An individual is assigned with a high fitness value if it is close to the optimal solution. For maximization problems, the cost function itself can act as the fitness function. While for minimization problems, the inverse of the cost function or the minus of the cost function

can be implemented as the fitness function. In this research, the BHA index value is to be minimized and minus J (given in Eq. (5.5)) is selected as the fitness function.

Individuals with high fitness values should have high probabilities of being kept for future crossover. Based on this idea, different methods were developed to implement selection. In this research, the proportionate selection, rank selection, and the tournament selection are studied. For proportionate selection, the probability of an individual to be selected for crossover is proportional to its fitness value, which yields

$$P_k = \frac{F_k}{\sum_{i=1}^{N_P} F_i} \tag{5.6}$$

where P_k is the probability of individual k to be selected; F_k is the fitness value of individual k; F_i is the fitness value of individual i; and N_P is the population size.

For rank selection, the individuals are sorted from largest to smallest based on fitness value and a probability is assigned based on the rank, given by

$$P_k = \frac{N_P - r_k + 1}{\sum_{i=1}^{N_P} r_i} \tag{5.7}$$

where r_k is the rank of the k^{th} individual; and r_i is the rank of the i^{th} individual.

For tournament selection, n out of N_P individuals are randomly picked with equal chance and the best of these n individuals is finally selected for crossover. This procedure is repeated for N_s times to select N_S individuals for crossover.

All three selection methods are tested and compared. The proportionate selection fails with negative fitness value. It also converges slower than the other two methods as a

good individual cannot distinguish itself when the fitness values are closed to each other. The rank selection and tournament selection work well for all kinds of fitness function. They also indicate higher converging rates compared to the proportionate selection method.

5.3.3. Encoding and Crossover

The encoding procedure represents a solution in the form of a data string called chromosome. Each data inside the chromosome is a gene [108]. For the proposed problem, a chromosome is given by

$$\text{chromosome} = [s_1, s_2, ..., s_{l-1}, s_l] \tag{5.8}$$

where s_1, s_2, s_{l-1}, and s_l are positions of the stabilizers. In this case, we have l stabilizers to be optimized simultaneously. Crossover is conducted between two selected chromosomes. Assume the mating chromosomes are $[x_1, x_2, \dots, x_{l-1}, x_l]$ and $[y_1, y_2, \dots, y_{l-1}, y_l]$, the offspring after crossover can be represented as

$$\begin{aligned} \text{offspring}_1 &= \left[x_1, x_2, ..., x_k, \alpha x_{k+1} + (1-\alpha) y_{k+1}, ..., \alpha x_l + (1-\alpha) y_l \right] \\ \text{offspring}_2 &= \left[y_1, y_2, ..., y_k, (1-\alpha) x_{k+1} + \alpha y_{k+1}, ..., (1-\alpha) x_l + \alpha y_l \right] \end{aligned} \tag{5.9}$$

where point $k \in \{1,2, \dots, l\}$ is randomly selected to break the chromosome; and α follows a uniform distribution between 0 and 1.

5.3.4. Mutation and Elitism

Mutation randomly changes the value of a gene. It can add diversity to the solutions and help the algorithm jump out of local optima [109]. The mutation rate should be low for a steady convergence. Assume gene *k* in chromosome *j* is subject to mutation, the new chromosome yields

$$\begin{aligned} \text{chromosome}_{\text{j}} &= \left[s_1, ..., s_k, ..., s_l \right] \\ \text{chromosome}_{\text{j}}' &= \left[s_1, ..., s_{\min} + \beta \left(s_{\max} - s_{\min} \right), ..., s_l \right] \end{aligned} \tag{5.10}$$

where $\text{chromosome}_{\text{j}}$ is the original chromosome; $\text{chromosome}_{\text{j}}'$ is the chromosome after mutation; s_k is the k^{th} gene, which represents the position of the k^{th} stabilizer in this problem; $s_{\min}$ and $s_{\max}$ are the lower and upper bounds of a feasible solution. In this case, they are the lower and upper ends of the BHA, respectively; and β follows a uniform distribution between 0 and 1.

To increase the convergence rate and algorithm stability, the elitism is applied which preserves the best few solutions at each generation [110]. As a result, the cost function decreases monotonically as the population evolves. Figure 5-4 compares the optimization processes with and without the elitism. As we can see, by involving the elitism, the best individual of the next generation is guaranteed to outperform the previous one. For the BHA structure optimization, a base design is usually provided. In this research, the base design is inputted as an individual of the initial generation; therefore, the redesigned BHA resulting from the GA is guaranteed to outperform the base design even when the GA is stuck in a local optimum.

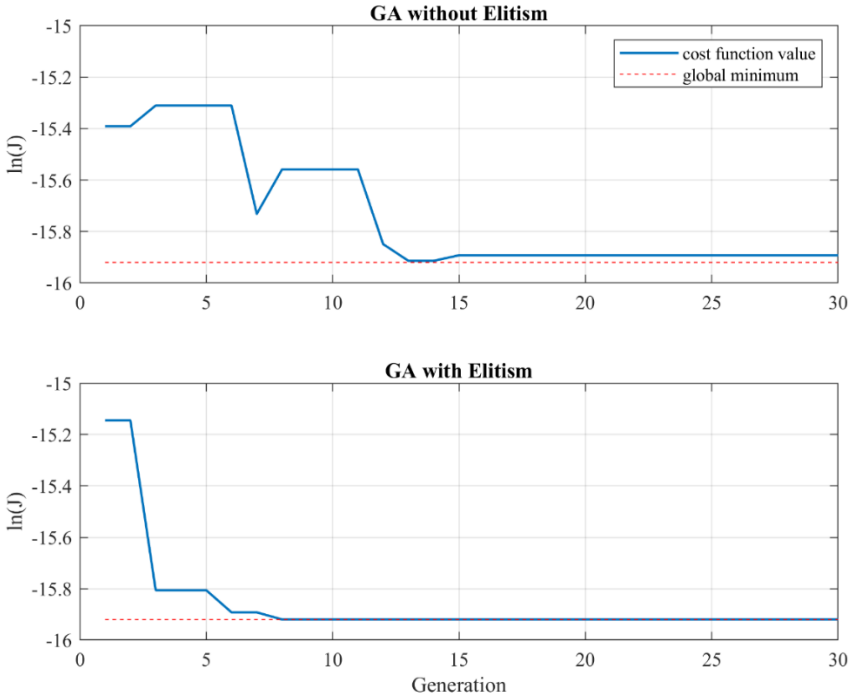

Figure 5-4. Effect of elitism

In the optimization framework illustrated in Figure 5-3, calculating the BHA index value based on the FEM simulation requires the most computational effort. However, FEM simulations can be conducted independently without knowing the previous results; therefore, parallel computation can be achieved, which significantly reduces the computational time.

5.4. Simulation and Verification

In this section, simulations are conducted to verify the proposed optimization framework. First, the BHA model is verified by comparing its solution against current literature. Afterwards, the GA is tested by solving a multi-variable nonconvex

optimization problem. Finally, the proposed method is implemented to redesign a production BHA to achieve the minimum BHA strain energy.

5.4.1. BHA Model Verification

The cost function of the proposed problem is obtained from FEM simulations; therefore, the optimization performance is heavily reliant on the modeling accuracy. In Section 3.5, the FEM model has been verified by comparing against analytical solutions and current literature. In this simulation, the BHA model is compared against reference [45], in which the vibration indices are proposed. The BHA structures can be found in reference [45]-Fig. 4. The WOB is set to 25000 lbf and the rotary speed is set to120 rpm. The results are illustrated in Figure 5-5, with two colors representing two different BHAs. These results agree well with those in reference [45]-Fig. 5.

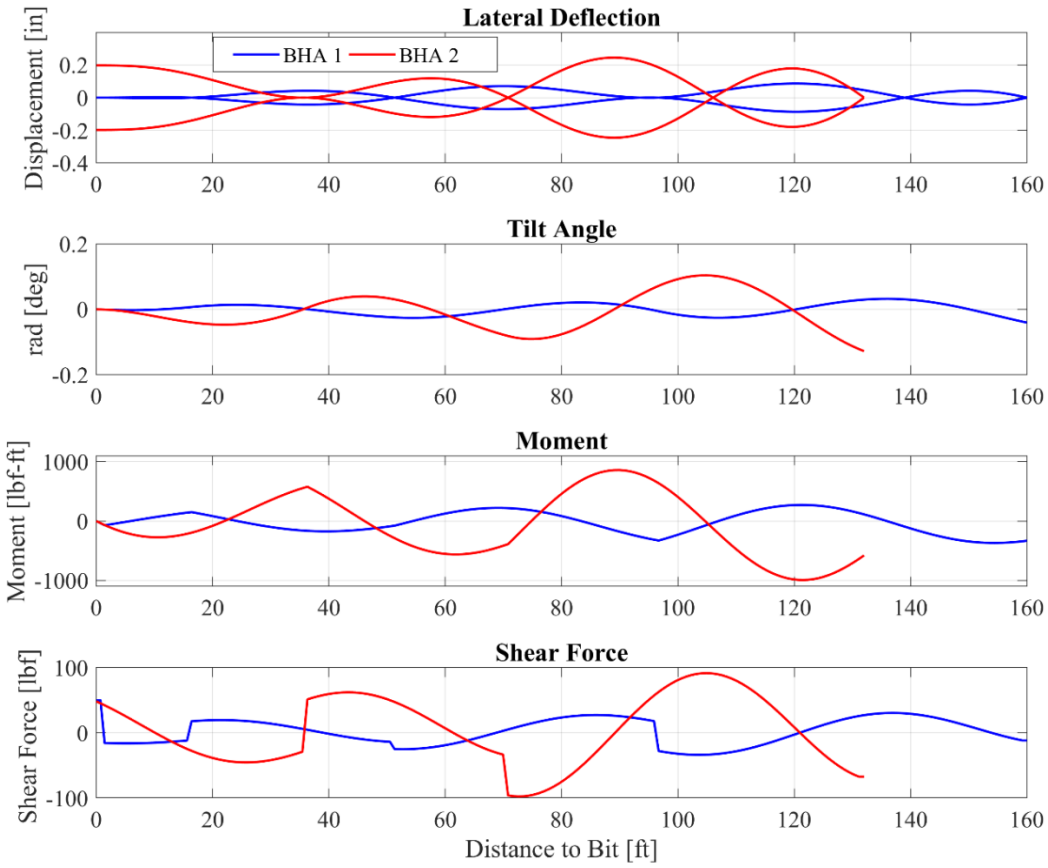

Figure 5-5. BHA vibration mode obtained from FEM simulation

5.4.2. GA Test

The GA developed in this chapter is tested by optimizing a multi-variable non-convex problem, given by

$$\begin{aligned} &\min J = x\cos(x) + 2y\sin(2y) \\ &s.t.\ \ x, y \in [0,10] \end{aligned} \tag{5.11}$$

The cost function over the feasible area is visualized in Figure 5-6, where the global minimum is located at $x = 9.5293$ and $y = 8.6682$ with $J = -26.7849$. Due to the use of *sin* and *cos*, the cost function J periodically oscillates and results in multiple local

minima and maxima. By testing on Eq. (5.11), we explore the capability of the GA to find the global optimum out of the local optima. In this simulation, the population size is configured at 16, the elitism number is configured at 2, and mutation rate is configured at 10%. An evolutionary process is visualized in Figure 5-7, where the arrow shows the evolution direction, the white hexagram represents the best solution of each GA generation and the red star is the global minima. As illustrated in Figure 5-7, the algorithm can quickly converge to global minima within a few generations. To test the robustness of the GA, Monte-Carlo simulations are conducted for 5000 times. For each simulation, the population evolves for 30 generations and the best solution at each generation is recorded for a statistical study (in total 30×5000 data points are recorded). The boxplot of the best solution at each generation is provided in Figure 5-8, where the black bars are the upper and lower limits of the simulation results, the blue box represents the 25^{th} to 75^{th} percentile of the simulation results, and the red bar is the median value of the simulation results. At the 30^{th} generation, the median value of the 5000 simulations is -26.7477 which is only 0.138% off the true minimum value at -26.7849. The 25^{th} percentile and 75^{th} percentile are -26.7813 and -26.5374, which are only 0.013% and 0.924% off the true minimum value, respectively. This test proves the capability of the GA in solving multi-variable nonconvex optimization problems.

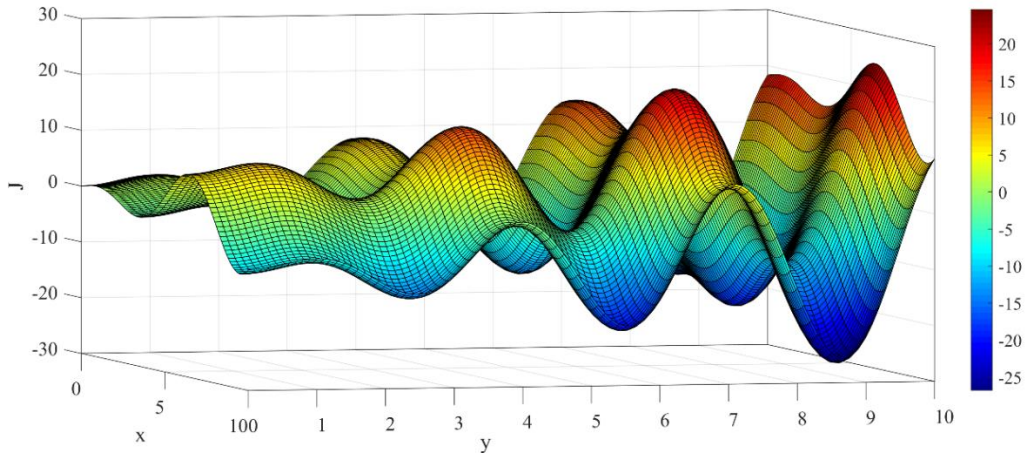

Figure 5-6. Visualization of equation

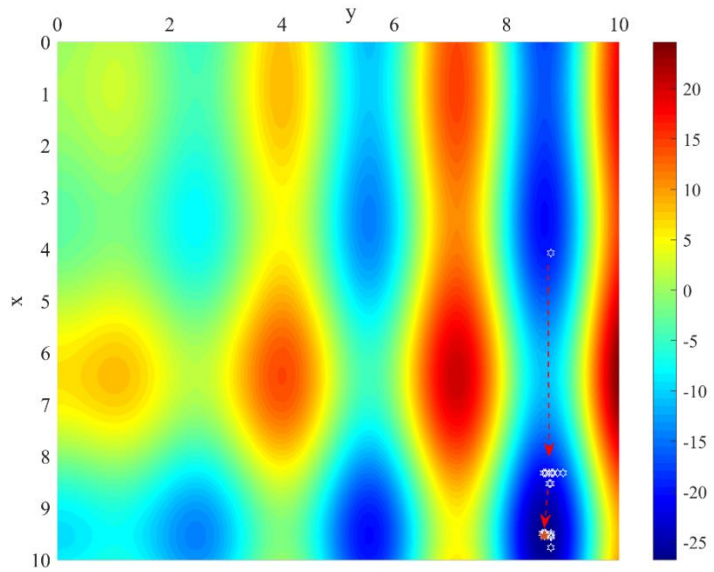

Figure 5-7. Evolutionary process of GA

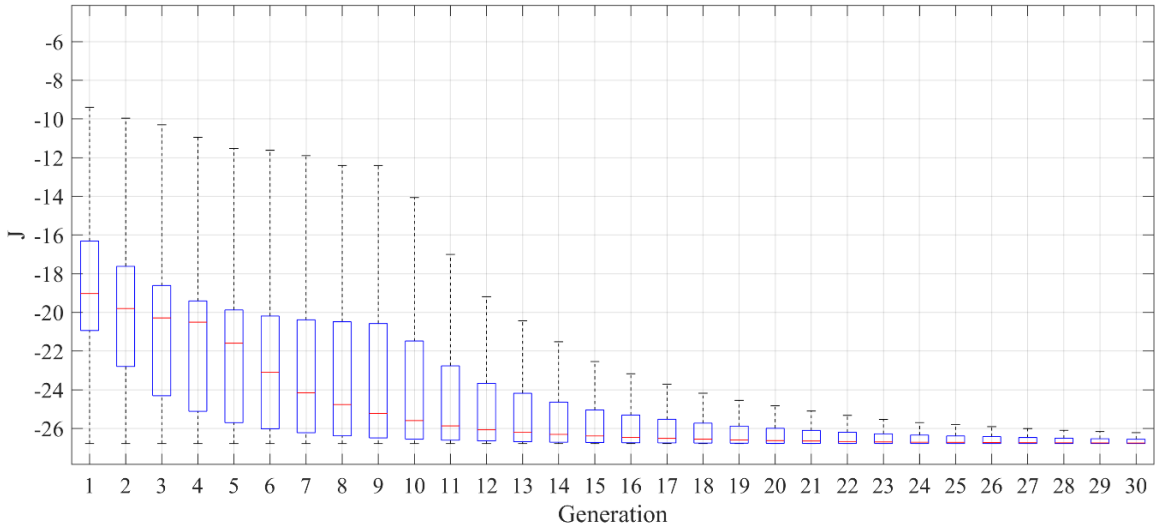

Figure 5-8. Boxplot of the first 30 generations based on 5000 simulations

5.4.3. BHA Optimization

In this section, the stabilizers of a real BHA are optimized using the proposed method. The BHA structure is illustrated in Figure 5-1, where a near-bit stabilizer is fixed at 1.1 ft from the bit. The position of the other stabilizer is subject to optimization. The cost function value versus stabilizer position is obtained through an exhaustive search method, as illustrated in Figure 5-2. According to the results obtained from the exhaustive search, the optimal position is found at 131.8 ft from the bit and the corresponding cost function value is 1.3×10^{-7} ($\ln(1.3 \times 10^{-7}) = -15.85$). The proposed GA is then applied to optimize the stabilizer position, where the population size is configured at 12, the elitism number is configured at 2, and the mutation rate is configured at 20%. The elitism number is set at a small value to ensure the population can evolve at each generation, and the mutation rate is set at a low level to ensure the convergence of the GA. One simulation result is illustrated in Figure 5-9, where the cost

function quickly converges to the global minimum and the optimal BHA design is obtained.

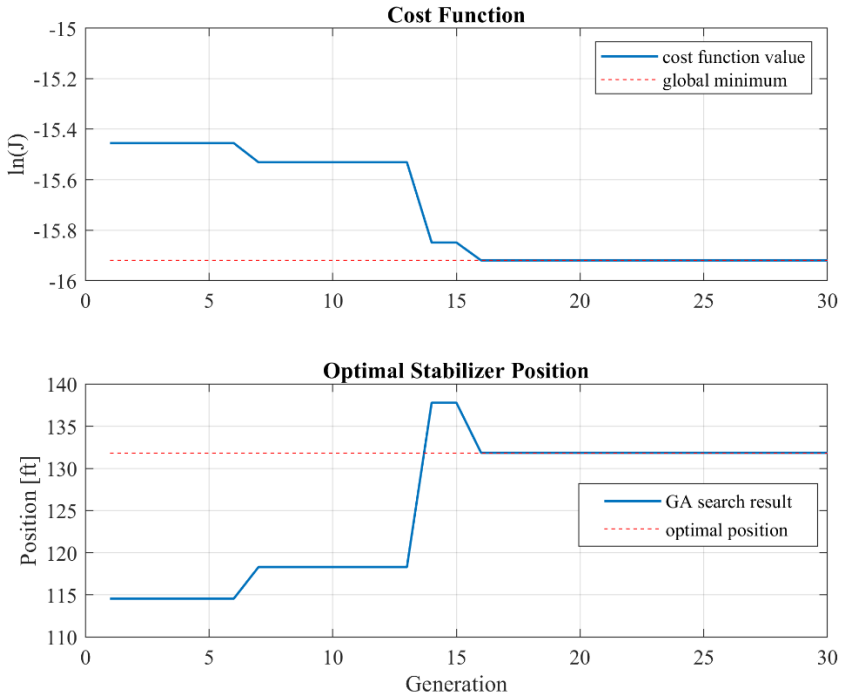

Figure 5-9. GA optimization process

To test the robustness of this algorithm, Monte-Carlo simulations are conducted 100 times. The boxplots of the cost function value and optimized stabilizer position are illustrated in Figure 5-10. At the 15th generation, the stabilizer position converges to the global optimum with only 5 outliers (95% confidence). At the 30th generation, only 3 outliers do not achieve the global optimization. The worst scenario has a cost function value of 1.34×10^{-7}, which is very close to the global minimum of 1.3×10^{-7}. To obtain the optimal position, the exhaustive search needs to run the FEM simulation $\binom{N}{n_s}$ times, where N is the number of finite elements and n_s is the number of stabilizers to be optimized. In this case, the BHA is meshed with 200 elements. The number of FEM

simulations that need to be conducted for exhaustive search is calculated in Table 5-1. With 4 stabilizers, it takes over 6.4×10^7 FEM simulations to find the optimal position. However, using the proposed method, the GA can find the optimal position within 30 generations, which needs only 302 FEM simulations.

Stabilizer Number	1	2	3	4
FEM simulation	200	19900	$O(10^6)$	$>O(10^7)$

Table 5-1. Number of FEM simulations to be conducted for exhaustive search

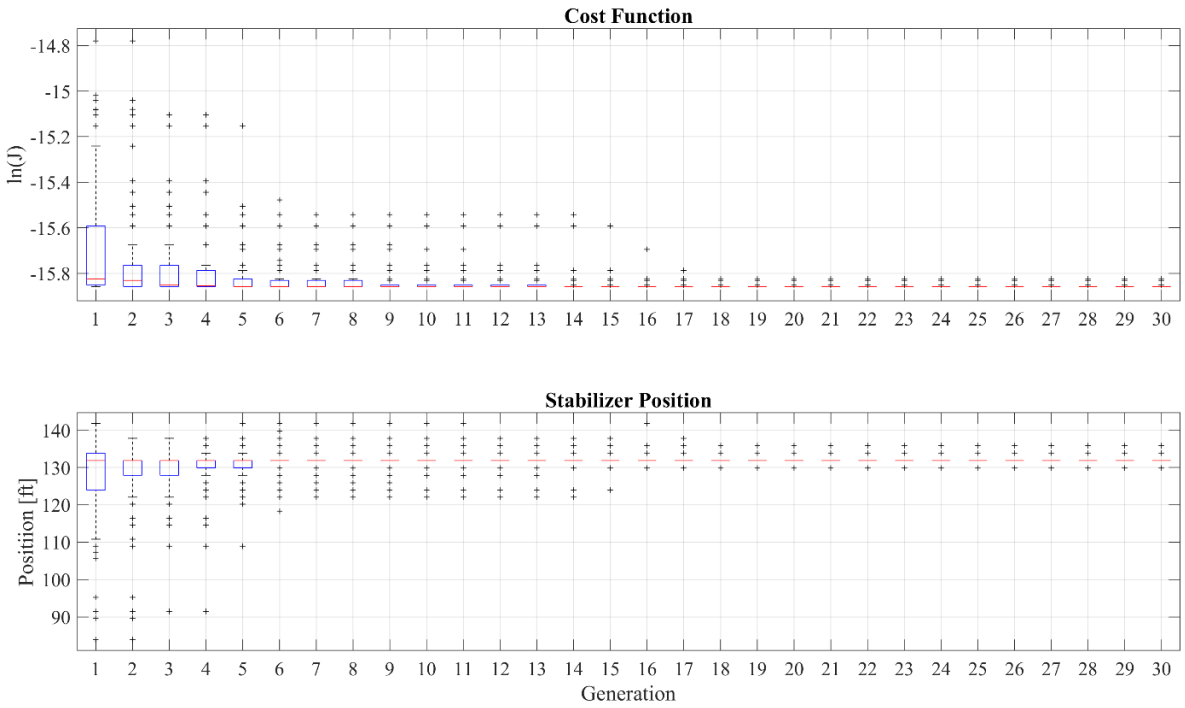

Figure 5-10. Boxplots of the cost function and stabilizer position based on 100 GA simulations

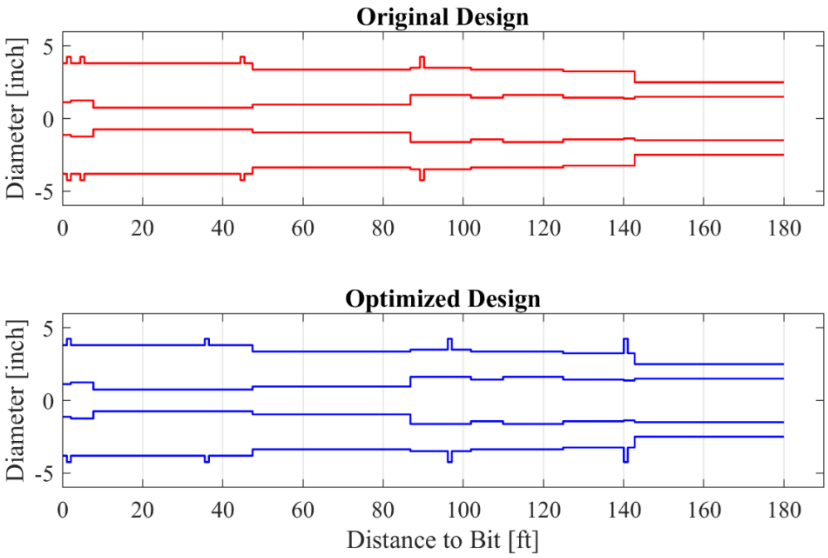

Figure 5-11. Comparison between original BHA and optimized BHA

In another design, there are four stabilizers installed, which are at 1.1 ft, 5.45 ft, 45.4 ft, and 90.2 ft from the bit. Fixing the near-bit stabilizer and optimizing the other three using the developed method, the positions of the stabilizers are reconfigured at 36.52 ft, 97.14 ft, and 141.76 ft from the bit. The structures of the original BHA and the optimized BHA are illustrated in Figure 5-11. In the original design, the left two stabilizers are very close to each other to stabilize the bit vibrations. However, this design causes the remaining part of the BHA subject to severe vibrations and reduces the overall performance of the BHA. The BHA strain energy and the stabilizer side force of the original BHA and the optimized BHA are compared in Figure 5-12, where the dashed lines represent the maximum value of the first three modes, and the solid lines represent the mean value of the first three modes. As can be concluded from this comparison, the index values of the optimized BHA are significantly reduced compared to the original design, indicating a much better dynamic performance.

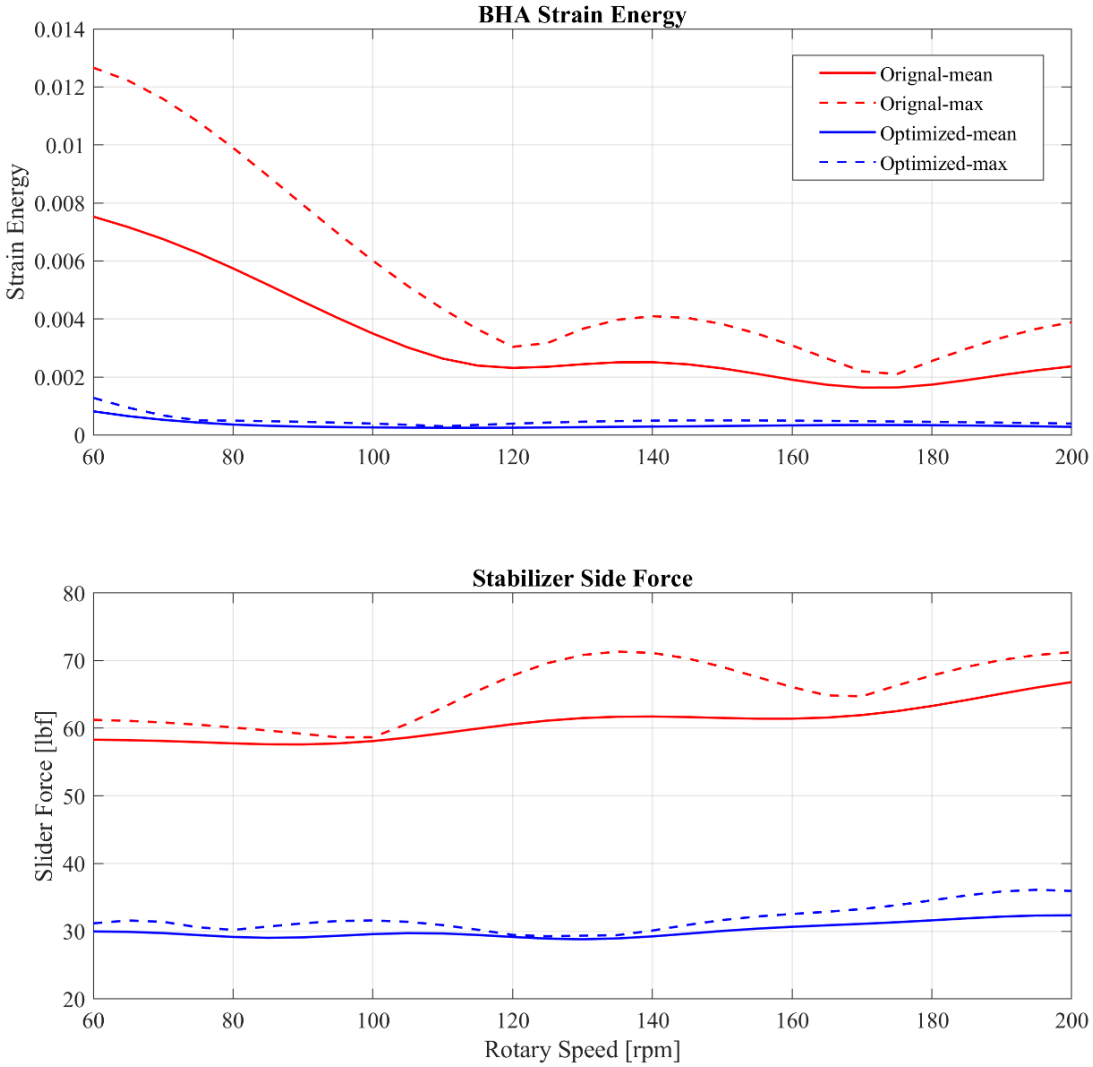

Figure 5-12. Comparison between original BHA and optimized BHA

5.5. Summary

In this chapter, a framework to optimize the BHA structure is proposed to reduce drilling vibrations. Index values, based on FEM simulations, are calculated to quantify the BHA dynamic performance and used to formulate the cost function. The cost function is nonconvex within the feasible domain according to an exhaustive search. In addition, the BHA indices cannot be expressed as explicit functions of the positions of the

stabilizers; therefore, the derivative-free GA is selected to solve the optimization problem. A production BHA is optimized following the steps shown in Figure 5-3. The GA can find the optimal solution with a high accuracy and low computational effort. After optimization, the BHA strain energy and the stabilizer side force are significantly reduced compared to the original design, which proves the developed BHA design optimization framework can lead to a significant reduction of undesirable drilling dynamics. The main content of this chapter is published in [111].

Chapter 6. REDUCED ORDER MODEL AND CONTROL

In previous chapters, a comprehensive FEM modeling framework is established for directional drillings. This model provides high-fidelity simulations for drill-string statics and dynamics and can be used to estimate torque and drag, predict drilling failures, analyze drilling vibrations, and test top drive controllers. Compared with existing FEM drill-string models, the proposed model achieves a high computational efficiency by 1). linearizing drill-string dynamics around the central axis of the well and 2). applying curved beam elements which require fewer elements to mesh the drill-string. However, the computational cost is still high because of the inherent features of FEM. Using a regular desktop computer (Intel i7-7660U @ 2.5GHz, 16GB RAM, 64bit OS), this model (with 200 elements) just achieves real time simulation under a MATLAB environment. In some cases, simulation speed and model simplicity are more important than model accuracy, as long as the main dynamics are captured. Therefore, this chapter studies reduced order models for faster drilling analysis.

6.1. Reduced Order FEM Model

Torsional dynamics are the primary dynamics of drilling activities and torsional vibration control is the type of control most often researched. Consequently, in developing reduced order models, only the torsional dynamics are considered. The stick-slip frequency is usually the lowest natural frequency of the drill-string. As a result, low-order FEM models are enough to capture the stick-slip dynamics. The dynamic responses

Part of this chapter was published in: 1. Feng, T., Zhang, H. and Chen, D., 2017, May. Dynamic Programming Based Controllers to Suppress Stick-slip in a Drilling System. In *American Control Conference (ACC), 2017* (pp. 1302-1307). IEEE.; 2. Feng, T., et al. "A Finite Element Method with Full Bit-Force Modeling to Analyze Drillstring Vibration." *Journal of Dynamic Systems, Measurement, and Control* 139.9 (2017): 091016;
The author contributes to 1. design dynamic programming controllers to suppress the stick-slip vibration; 2. derive reduced-order FEM model

of several low-order FEM models and one high-order FEM model are compared in Figure 6-1. The modal truncation method [112] is also implemented for order reduction. Based on Eq. (4.32), the dynamic model can be formulated by

$$\dot{\boldsymbol{x}} = [A]\boldsymbol{x} + \boldsymbol{B}u \tag{6.1}$$

$$y = \boldsymbol{C}\boldsymbol{x} \tag{6.2}$$

$$[A] = \begin{bmatrix} [0] & [1] \\ -[M]^{-1}[K] & -[M]^{-1}[D] \end{bmatrix} \tag{6.3}$$

$$\boldsymbol{B} = \begin{bmatrix} 0 \\ [M]^{-1}\boldsymbol{b} \end{bmatrix} \tag{6.4}$$

where $\boldsymbol{x}$, equal to $[\boldsymbol{U} \quad \dot{\boldsymbol{U}}]^T$, is the state vector; u is the input torque of the top drive; y is the rotary speed of the bit; and $\boldsymbol{b}$ denotes the position of top drive torque. Transforming the state-space of the full dynamic system into canonical form, we have

$$[T_v]^{-1}[A][T_v] = \begin{bmatrix} [A_L] & [0] \\ [0] & [A_H] \end{bmatrix} \tag{6.5}$$

$$[T_v]^{-1}\boldsymbol{B} = \begin{bmatrix} \boldsymbol{B_L} \\ \boldsymbol{B_H} \end{bmatrix} \tag{6.6}$$

$$\boldsymbol{C}[T_v] = [\boldsymbol{C_L} \quad \boldsymbol{C_H}] \tag{6.7}$$

where $[T_v]$ is the transforming matrix composed of the eigenvectors of matrix $[A]$. The modal truncated model is then $([A_L], \boldsymbol{B_L}, \boldsymbol{C_L})$ by retaining only the low-frequency

eigenvalues. A comparison between the dynamic response of the full model and the dynamic responses of the truncated models is illustrated in Figure 6-2. As can be concluded from Figure 6-1 and Figure 6-2, both the low-order FEM and the modal truncation method are able to accurately approximate the dominant dynamics of the high-order FEM model, thereby establishing an accurate reduced order model.

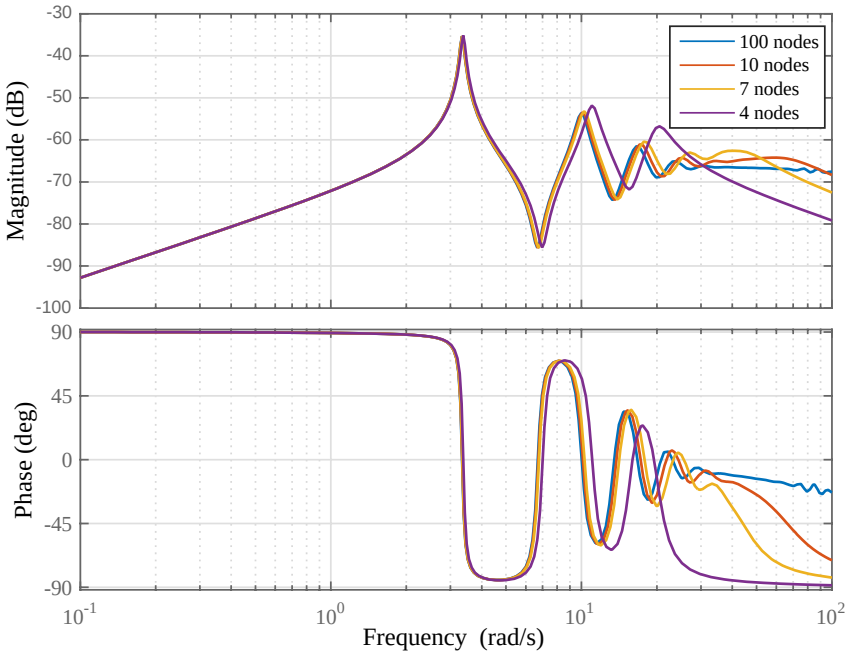

Figure 6-1. Frequency responses of a high-order FEM model and low-order FEM models

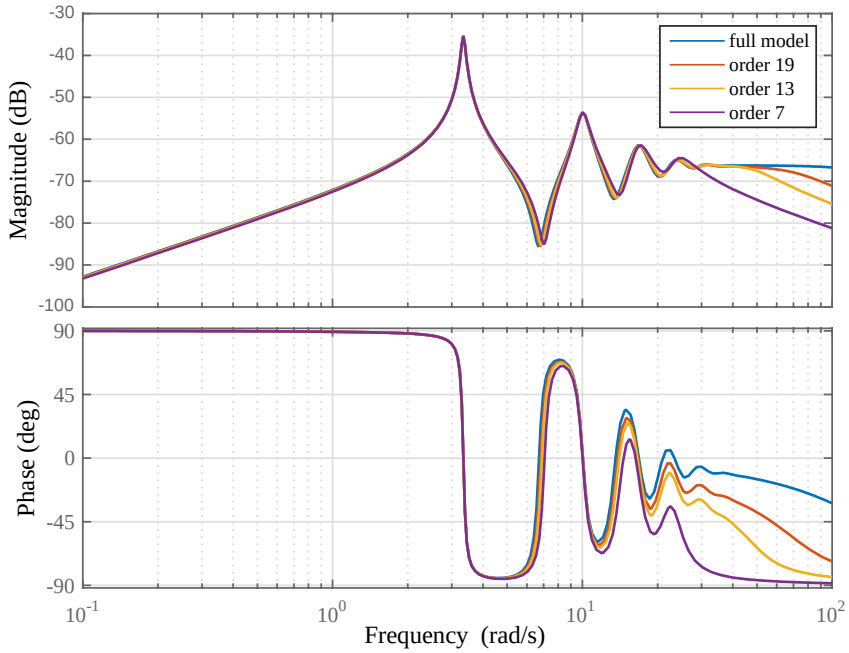

Figure 6-2. Frequency responses of the full-order model and low-order models through modal truncation

6.2. Lumped Parameter Model

A lumped-parameter model can characterize the first natural mode of a drill-string and simulate the stick-slip vibration. It is computationally efficient and widely applied in control strategy development [113]. In this section, the torsional dynamics of the drill-string is modeled using the lumped-parameter method, where the top drive and the BHA are modeled as rotary inertias, and the slender drill-pipe is modeled as a torsional spring (see Figure 6-3). The system dynamics equation can be expressed as

$$J_t\ddot{\phi}_t + c_t\dot{\phi}_t + k_s\left(\phi_t - \phi_b\right) = u \tag{6.8}$$

$$J_b\ddot{\phi}_b + c_b\dot{\phi}_b - k_s\left(\phi_t - \phi_b\right) = -T_{ob} \tag{6.9}$$

where J_t and J_b are rotary inertias of the top drive (including motor, gearbox, and other rotary components) and the BHA, respectively; c_t and c_b are damping coefficients of the top drive and the BHA, respectively; k_s is rotary stiffness of the drill-string; u is the input torque; and T_{ob} is the torque on bit, which is a nonlinear function of the bit rotary speed $\dot{\phi}_b$; ϕ_t and ϕ_b are the angular displacements of the top drive and the BHA, respectively; $\dot{\phi}_t$ and $\dot{\phi}_b$ are the angular speeds of the top drive and the bit, respectively; and $\ddot{\phi}_t$ and $\ddot{\phi}_b$ are the angular accelerations of the top drive and the bit, respectively.

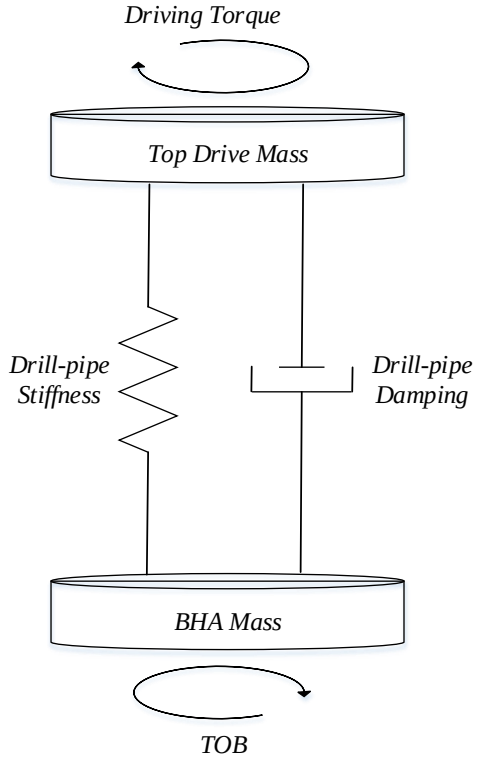

Figure 6-3. Lumped mass model

The Karnopp's friction model is applied to simulate the nonlinear relationship between the bit rotary speed $\dot{\phi}_b$ and the torque on bit T_{ob} [114][115], given by

$$T_{ob}\left(\dot{\phi}_b\right)=\begin{cases} W_{ob}R_b\mu_b\left(\dot{\phi}_b\right) & ,\ \dot{\phi}_b>\dot{\phi}_b^* \\ \min\left(T_e,\ W_{ob}R_b\mu_b\left(\dot{\phi}_b\right)\right) & ,\ \dot{\phi}_b\le\dot{\phi}_b^* \end{cases} \tag{6.10}$$

$$W_{ob}\sim N\left(W_{ob,s},\sigma^2\right) \tag{6.11}$$

$$\mu_b\left(\dot{\phi}_b\right)=\mu_d+\left(\mu_s-\mu_d\right)e^{-\gamma\left|\dot{\phi}_b\right|} \tag{6.12}$$

where W_{ob} is the WOB, which follows a normal distribution with a mean value of $W_{ob,s}$. The variance of WOB could originate from the disturbance of hook load, drilling mud circulation and bit-rock interaction; R_b is the radius of the bit; μ_b is the friction coefficient; T_e is the static TOB, which denotes the minimum TOB that the external torque need to overcome to make the bit move; $\dot{\phi}_b^*$ is the threshold value. According to Eq. (6.12) when the bit speed $\dot{\phi}_b$ is zero, μ_b is equal to the static friction coefficient μ_s. As $\dot{\phi}_b$ becomes larger, μ_b will converge to the dynamic friction coefficient μ_d. The rate of decay is determined by bit constant γ. Rewriting the above dynamic equations into state-space format $\dot{x}=f(x,u)$, we have

$$\frac{d}{dt}\begin{bmatrix}\dot{\phi}_b\\ \dot{\phi}_t\\ \phi_d\end{bmatrix}=\begin{bmatrix}-c_b/J_b & 0 & -k_s/J_b\\ 0 & -c_t/J_t & k_s/J_t\\ 1 & -1 & 0\end{bmatrix}\begin{bmatrix}\dot{\phi}_b\\ \dot{\phi}_t\\ \phi_d\end{bmatrix}+\begin{bmatrix}-1/J_b\\ 0\\ 0\end{bmatrix}T_{ob}+\begin{bmatrix}0\\ 1/J_t\\ 0\end{bmatrix}u \tag{6.13}$$

where ϕ_d, equals to $\phi_b-\phi_t$, is the phase difference. Plugging Eq. (6.10) into Eq. (6.13), the torsional dynamics of the drill-string can be modeled.

6.3. Dynamic Programming Based Controller

In this section, in order to demonstrate the utility of the reduced order models, a controller is developed by employing optimal control algorithms to suppress stick-slip vibrations. The cost function to be minimized is defined as

$$J = \sum_{k=0}^{N-1} E\left[g\left(x_k, u_k, w_k \right) \right] \tag{6.14}$$

$$g\left(x_k, u_k, w_k \right) = \left(\dot{\phi}_{t,k+1} - \omega_0 \right)^2 + \lambda_1 \left(\phi_{d,k+1} \right)^2 + \lambda_2 \left(\dot{\phi}_{b,k+1} - \omega_0 \right)^2 \tag{6.15}$$

where ω_0 is the set point of the rotary speed; w_k denotes the uncertainty caused by WOB; λ_1 and λ_2 are weight coefficients; k is the time step; and $x = [\dot{\phi}_b, \dot{\phi}_t, \phi_d]^{\mathrm{T}}$ is the state vector. The first term of $g(\cdot)$ keeps the top drive following a predefined constant speed. The second term regulates the phase fluctuation between the top drive and the BHA to reduce the stick-slip vibration. The third-term minimizes the fluctuation of the bit speed to suppress the stick-slip vibration.

The system has the following features:

1. The maximum and minimum values of the control input u are bounded ($u_{\min}<u<u_{\max}$), determined by the output capability of the top drive.
2. According to Eq. (6.13), the established system satisfies the Markov property, which means the future states depend only upon the present state and action, not on the sequence of events that precedes it (here action means exerting torque on the top drive).

$$x_{k+1} = F\left(x_k, u_k, w_k \right) \tag{6.16}$$

3. The state variables of Eq. (6.13) are bounded with bounded input u; therefore, $g(\cdot)$ in Eq. (6.15) is compact.

$$g\left(x,u,w\right)\in L_{\infty}\ \ s.t.\ \ u\in L_{\infty} \tag{6.17}$$

Based on the features 1 to 3, DP can be implemented to solve the optimization problem. The first step is to discretize the system. In the spatial domain, the state variables of Eq. (6.15) are meshed equally and a three-dimensional state space S will be obtained. Each point on the grid is called a state. According to feature 3, the number of states in S is finite so the search area on S is finite. The input variable is also equally meshed between its minimum and maximum thresholds and an action space U will be obtained. According to feature 1, the number of actions in U is also finite ($U\in[u_{min}{:}\,du:\,u_{max}]$). A mapping from state space S to action space U is called a policy π. Through DP, we can find the optimal policy π^{*} that minimizes the cost function. The drilling operation usually lasts for a very long time. Accordingly, the infinite-horizon DP ($N=\infty$) is applied, where a stationary (time-invariant) policy can be obtained. Based on Bellman's principle, we have

$$J^{*}\left(x\right)=\min_{u\in U}\left[\alpha J^{*}\left(F\left(x,u,w\right)\right)+g\left(x,u,w\right)\right],\ \ \forall x\in S \tag{6.18}$$

$$\pi^{*}\left(x\right)=\arg\min_{u\in U}\left[\alpha J^{*}\left(F\left(x,u,w\right)\right)+g\left(x,u,w\right)\right],\ \ \forall x\in S \tag{6.19}$$

where $J^{*}(x)$ is the minimum value of the cost function for state x; $\pi^{*}(x)$ is the optimal policy; $\alpha\in(0,1)$ is the discount factor. For infinite-horizon DP, the cost function is

transferred from Eq. (6.14) to Eq. (6.18) by introducing the discount factor α to keep the cost function bounded [116].

$$\left|J\left(x\right)\right| \le \frac{1}{1-\alpha} M, \ \ s.t. \ \left|g\left(x,u,w\right)\right| \le M \tag{6.20}$$

There are two basic methods to solve the DP problem: value iteration and policy iteration. Value iteration solves Bellman's equation explicitly but converges slowly. Policy iteration converges much faster but needs to solve an $N_s \times N_s$ linear equation, where N_s is the number of states. Considering that the dimension of the state vector is relatively large, the policy evaluation algorithm is also computationally extensive. In this research, the optimistic policy iteration algorithm [117] (or modified policy iteration algorithm) is implemented to find the optimal policy $\pi^*(x)$. It can explicitly calculate the cost function and require less iteration to converge than the value iteration algorithm. The flow chart is illustrated in Figure 6-4.

According to Figure 6-4, the greedy policy π_1 is implemented for initialization. Afterwards, the policy is improved through two successive procedures: policy evaluation and policy improvement. The former procedure calculates the cost function of each policy by repeating several value iterations, while the latter procedure updates the policy through minimizing the cost function. After policy improvement, the new policy will get closer to optimum. In infinite-horizon DP, the subscript *k* denotes the iteration number rather than the time step. When the value of the cost function converges, the corresponding mapping is the optimal policy. In Figure 6-4, when *m* equals one, the algorithm becomes a value iteration algorithm, and when *m* equals infinity, it becomes a

policy iteration algorithm. When taking other values, a small *m* needs to conduct more policy improvements to converge, and a large *m* takes longer for policy evaluation. In this research, to minimize the overall training computation, *m* is chosen as 15 by making a trade-off between these two factors.

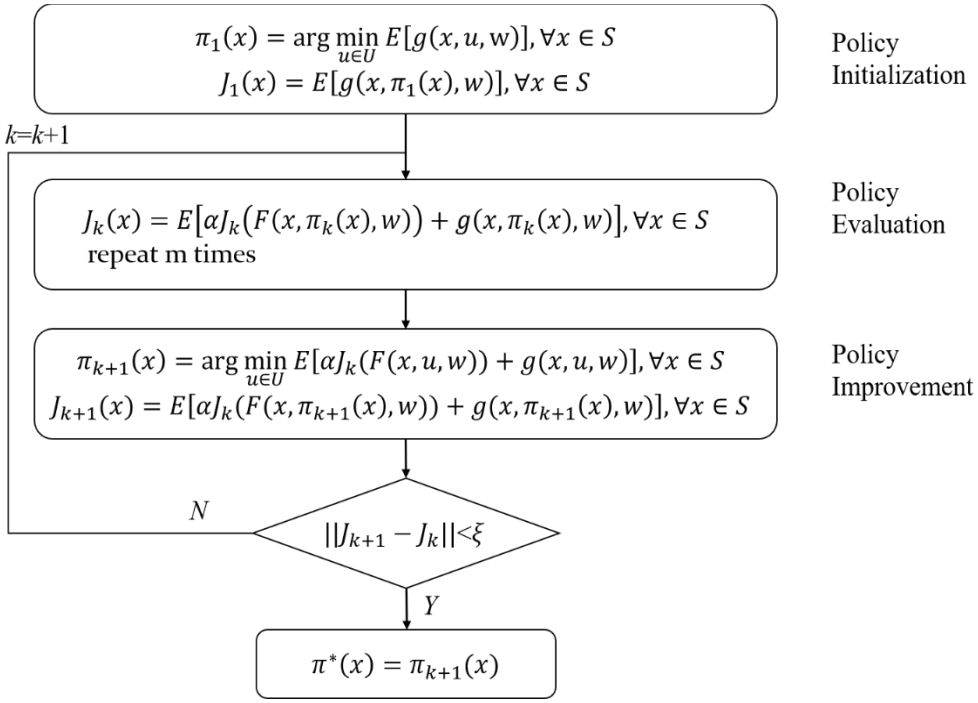

Figure 6-4. Flow chart of the optimistic policy iteration algorithm, where m is the number of value iterations used to approximate a policy iteration, and ξ takes a small positive value

Based on Eqs. (6.13) and (6.15) and Figure 6-4, simulations are carried out to get the optimal policy, see Figure 6-5, where four layers (phase difference=0, -2, -4 and -6) are selected for illustration. According to Figure 6-5, an interesting observation is that the optimal policy changes very little with BHA speed. This phenomenon holds under different drill-string and rock parameters according to the simulation. Making use of this feature, a model reduction can be achieved by only meshing $\dot{\phi}_t$ and ϕ_d to get the reduced

state space S'. Replacing S with S' in Figure 6-4, the optimistic policy iteration algorithm is conducted to get a reduced-order policy. The result is illustrated in Figure 6-6. Through model reduction, the computational speed is increased by $n \times r$ times (n is the number of grids to mesh $\dot{\phi}_b$, and r is the ratio of converging iterations of the full model to that of the reduced model. In this simulation, this value is 29×1). Generally, stick-slip vibration is indicated by a large speed fluctuation of the bit. At stick phase, drill-string strain energy builds up as the phase difference increases. After reaching a threshold value, the strain energy quickly releases, converting into kinetic energy of the BHA, where slip happens [118]. As we can conclude from Figure 6-6, with a small phase difference, a large torque is applied when the top drive speed is below the set point. However, with a large phase difference, a small torque is applied even when the top drive speed is low. This strategy can prevent strain energy from building up, therefore mitigating the stick-slip vibration. The control performances of the full-order policy and the reduced-order policy are compared in Section 6.4. Using full-order DP, we may need to optimize the policy offline due to the computational intensity and then implement the obtained map online. However, through model reduction, an online optimization can be achieved, which makes the proposed strategy able to update in real time. The proposed method is a full-state feedback controller, where $\dot{\phi}_t$ and $\dot{\phi}_b$ are measurable, but ϕ_d needs to be obtained from an observer.

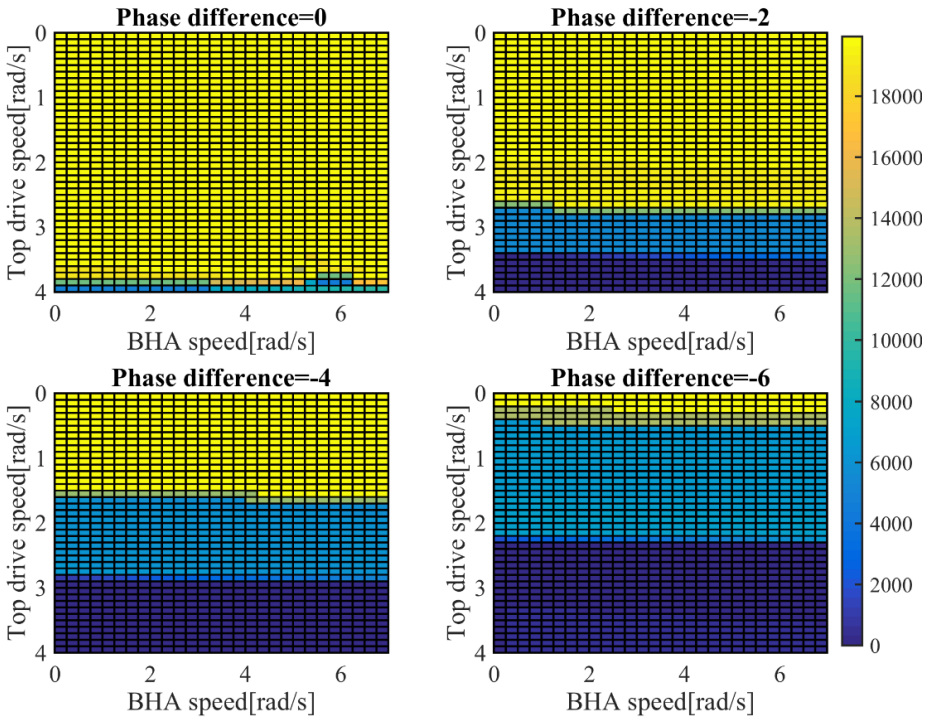

Figure 6-5. Optimal policy obtained from DP, where the color intensity indicates the value of control input

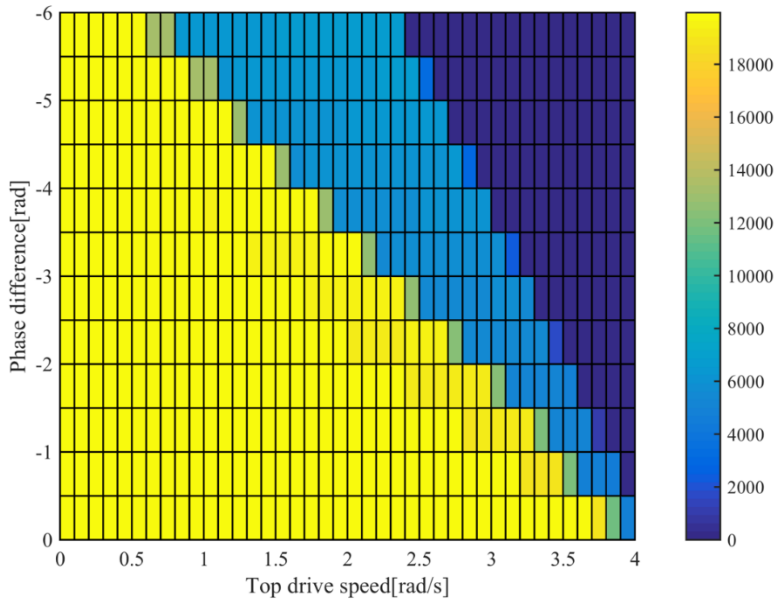

Figure 6-6. Reduced policy, where the color intensity indicates the value of control input

6.4. Simulation

In this section, simulations are carried out to verify the performance of the DP based controllers. The parameters are listed in Table 6-1. Since the policies map discrete states to discrete actions, a linear interpolation is implemented to obtain the final input as the system operates continuously. A PI controller is also simulated for comparison. The simulation results are illustrated through Figure 6-7 to Figure 6-9. According to Figure 6-7, the top drive speed is maintained relatively constant with a PI controller, but the BHA speed oscillates significantly between 0 and twice the set point, which indicates a stick-slip vibration. As illustrated in Figure 6-8, using the DP based controller, the BHA speed and top drive speed have some minor oscillations at the beginning, yet they quickly converge to the set point and get stabilized. Accordingly, the proposed DP based controller can effectively suppress the stick-slip vibration. Comparing Figure 6-8 and Figure 6-9, the performance of the reduced-order DP controller is very close to its full-order counterpart, while the computational efficiency in obtaining the reduced-order policy is significantly increased. This result justifies the application of model reduction to this problem.

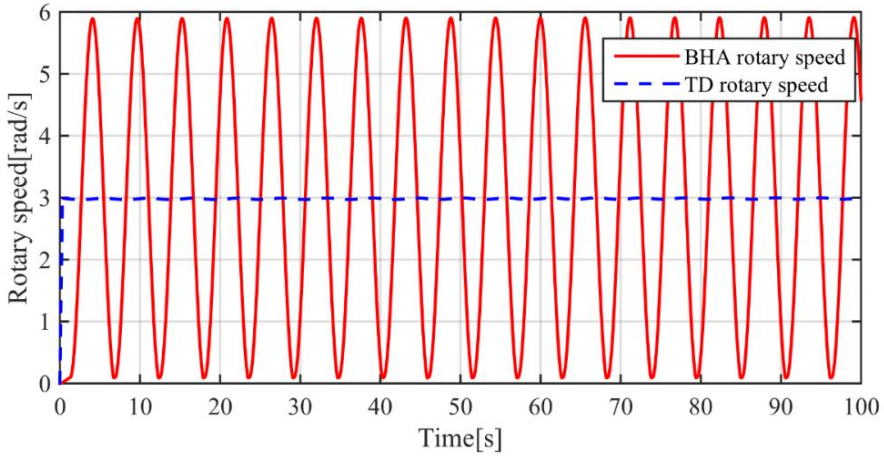

Figure 6-7. Performance of the PI controller

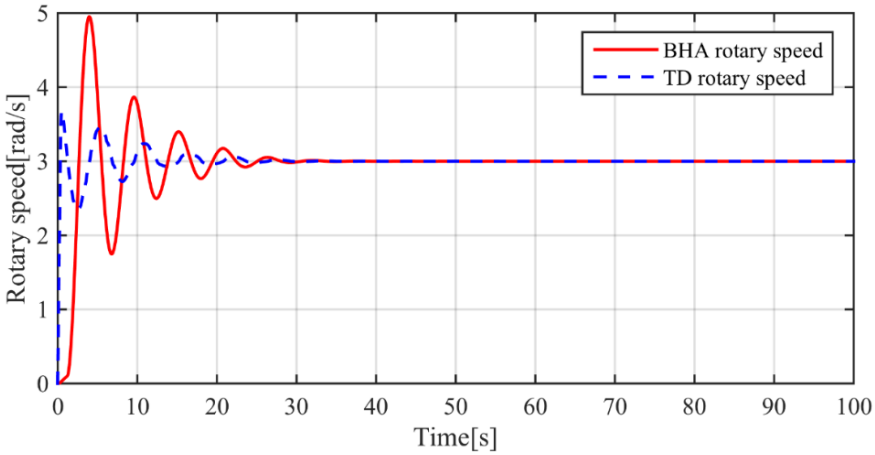

Figure 6-8. Performance of full-order DP based controller

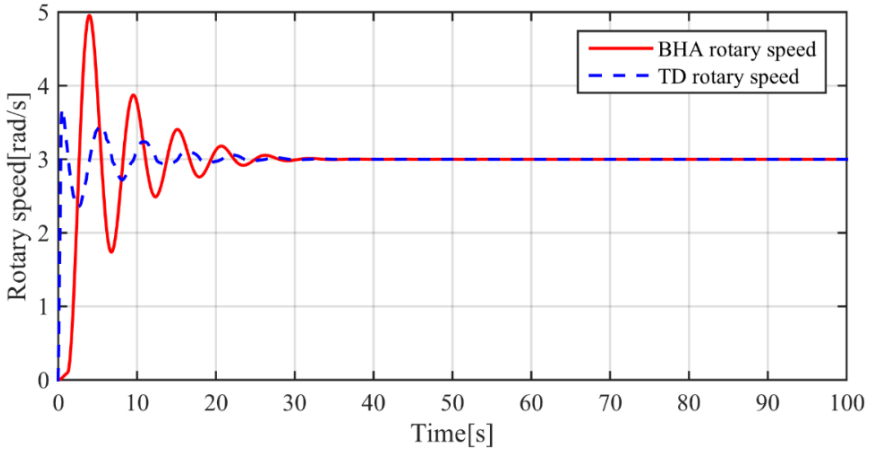

Figure 6-9. Performance of reduced-order DP based controller

In order to verify the robustness and stability of the proposed controller, the following perturbations are added in a non-ideal scenario.

1. Disturbances are added to the WOB, which could originate from hook load variation, mud circulation variation, and bit-rock interaction disturbances;
2. A non-ideal speed sensor is implemented where the presence of noise is considered.

Under the non-ideal scenario, the system is controlled by PI controller at the beginning, then the DP based controller is activated at a random time. The simulation result is illustrated in Figure 6-10. Although there are some minor fluctuations due to WOB oscillation, the whole system can still get stabilized quickly and remain stable after the implementation of the DP based controller. Simulations are carried out under different parameters and the proposed DP-based controller shows similar robustness.

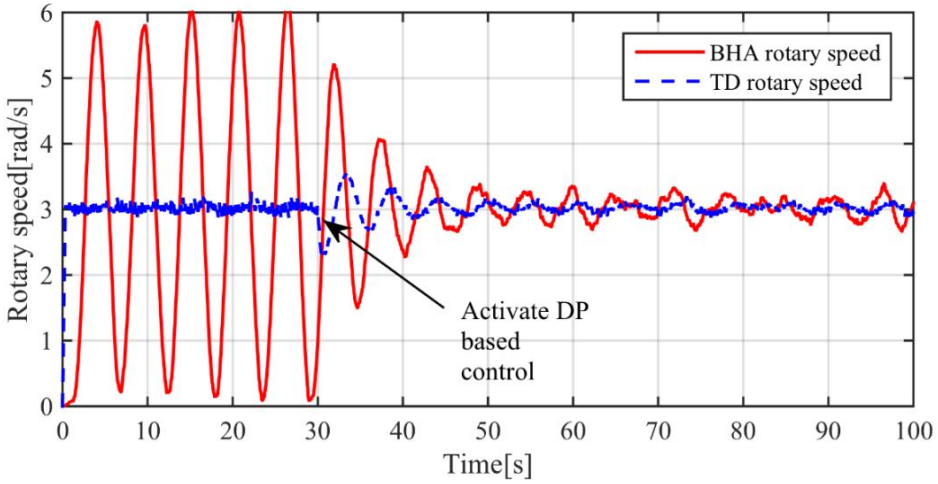

Figure 6-10. Robustness of the DP based controller

Symbol	Description	Value
J_t	Top drive rotary inertia	2122 [kg·m^2]
J_b	BHA rotary inertia	374 [kg·m^2]
k	Rotary stiffness of the drill-string	473 [Nm/s]
c_b	BHA damping	20 [Nms/rad]
c_t	Top drive damping	300 [Nms/rad]
R_b	Bit radius	0.1 [m]
μ_s	Static friction coefficient	0.8
μ_d	Dynamic friction coefficient	0.6
γ	Bit constant	1
W_{ob}	Weight on bit	40000 [N]
K_P	Proportional coefficient	10000
K_I	Integral coefficient	500

Table 6-1. Simulation parameter

6.5. Conclusion

In some cases (e.g., control design), simulation speed and model simplicity are more important, whereas the model accuracy is not the primary concern. Therefore, this chapter studies reduced order models for fast simulation. Firstly, low-order FEM models and modal truncated FEM models are studied. They perform well capturing the drill-string dynamics at low frequencies where stick-slip happens. A lumped mass model is also established, which can represent the first mode of a drill-string. Based on the lumped mass model, a DP is implemented to get the optimal policy that minimizes the stick-slip vibration. According to the optimal policy, the BHA speed is found to have negligible influence on control input; therefore, a dimension reduction is performed to eliminate the dependence of control input on BHA rotary speed, which significantly increases the computational efficiency. Simulations are carried out, where the stick-slip vibration is

effectively suppressed by both full-order policy and reduced-order policy obtained from DP. The DP controller is published in [22], which can be referred to for further study.

Chapter 7. CONCLUSION AND FUTURE WORK

7.1. Conclusion

This dissertation establishes an FEM modeling framework to describe directional drilling behaviors, which integrates a high-efficiency FEM drill-string model and a comprehensive boundary condition for drill-string and wellbore interaction. Drill-string kinematics can be conveniently described with reference to the well's central axis; therefore, knowing the well trajectory is essential in analyzing drill-string dynamics. This dissertation first discusses the minimum curvature method which obtains the continuous well trajectory from discrete survey measurements. It is proven that the obtained trajectory is not only continuous but also smooth (its derivative is continuous). The simulation results indicate a high accuracy estimate of well trajectory is obtained from the minimum curvature method. In addition, the DLS, walk rate, and build rate, which are commonly used by drilling industry to represent well geometries, can be conveniently represented using the minimum curvature method.

Analyzing directional drilling dynamics is a nonlinear large displacement problem. The developed FEM model linearizes the drill-string dynamics around the central axis of a directional well, which significantly simplifies the problem and increases the simulation speed. The linearization method is verified by comparing its results against existing methods. In traditional finite element models, a directional drill-string is approximated with a series of straight elements. However, the coupling mechanism among different degrees of freedoms is not considered by the straight beam elements. Meanwhile, the

straight beam approximation introduces additional discretization error; therefore, a very fine meshing is necessary to guarantee the numerical accuracy for the straight beam method, which leads to a low computational efficiency. To solves these problems, a six DOF curved beam element is derived using the assumed strain field method. According to the simulation results, the developed curved beam element achieves higher accuracy than the straight beam element in both static and dynamic analyses. As a result, compared with the straight beam elements, fewer curved beam elements can be used to achieve the same accuracy, which further reduces the computational cost.

The developed boundary conditions for directional drilling include models for the top drive and the draw-works, a model for drill-string and wellbore contact, and a model for bit forces. By combining the FEM models and the boundary conditions, a comprehensive modeling framework is established for directional drilling. Numerical methods are also presented for static and dynamic analyses. From static analyses, torque and drag can be calculated to prevent drilling failure. The strain and stress distributions along the drill-string can also be obtained to avoid stress concentration. From dynamic analyses, the normal drilling scenarios, the stick-slip vibrations, and the whirling vibrations are simulated using the proposed FEM modeling framework. The top drive controllers are also incorporated as torsional boundary conditions. The guidelines for tuning the control parameters are obtained from dynamic simulations.

Based on the developed FEM model, a framework to optimize the BHA structure is proposed to reduce drilling vibrations. BHA vibration indices are calculated using FEM simulations, which are used to formulate the cost function. The GA is selected to

solve the nonconvex optimization problem, which can find the optimal solution with a high accuracy and low computational effort. After optimization, the BHA strain energy and the stabilizer side force are significantly reduced compared to the original design, which proves the BHA optimization method can lead to a significant reduction of undesirable drilling dynamics. Lastly, reduced order models are discussed for fast simulation and control design.

7.2. Future Work

Based on the above completed tasks, future research topics are proposed in this section. In this work, a numerical Rayleigh damping is used to model the hydraulic effect of the mud. It would be of interest to model the mud damping with physical meanings, e.g., model the mud as a non-Newtonian fluid.

This dissertation studies the topics of controlling top drive torque and optimizing BHA structure to reduce drilling vibrations. A new trend is to directly control downhole actuators to eliminate the vibrations. From this aspect, designing new downhole actuators and developing corresponding control algorithms would be another interesting research topic.

The proposed FEM model can capture drill-string dynamics with a given well trajectory. However, it is unable to simulate the well propagation process with given drilling and RSS parameters. In order to achieve this, the RSS must be modeled, and the rock features and cutting process of the cutters need to be studied.

REFERENCES

[1] Cherutich, S.K., 2009. Rig selection and comparison of top drive and rotary table drive system for a cost effective drilling project in Kenya. Report, 8, pp.65-84.

[2] Allouche, E. N., Ariaratnam, S. T., and Lueke, J. S. (2000). Horizontal directional drilling: profile of an emerging industry. Journal of Construction Engineering and Management, 126(1), 68-76.

[3] Cooper, G.A., 1994. Directional drilling. Scientific American, 270(5), pp.82-87.

[4] Allouche, E.N., Ariaratnam, S.T. and Lueke, J.S., 2000. Horizontal directional drilling: profile of an emerging industry. Journal of Construction Engineering and Management, 126(1), pp.68-76.

[5] https://www.scientificamerican.com/article/bp-relief-well-drilling/

[6] Harris, Frank. Ground Engineering Equipment Methods. McGraw-Hill: New York: 1983.

[7] Pan, L., 2014. Stability Analysis of the Rotary Drill-String.

[8] Menand, S., Simon, C., Gerbaud, L., Ben Hamida, M., Denoix, H.J., Cuillier, B., Gaombalet, J., Amghar, Y. and Sinardet, H., 2012, January. PDC Bit Steerability Modeling and Testing for Push-the-bit and Point-the-bit RSS. In IADC/SPE Drilling Conference and Exhibition. Society of Petroleum Engineers.

[9] Stroud, D., Russell, M. and Peach, S., 2003, January. Development of the industry's first slimhole point-the-bit rotary steerable system. In SPE Annual Technical Conference and Exhibition. Society of Petroleum Engineers.

[10] Schaaf, S., Pafitis, D. and Guichemerre, E., 2000, January. Application of a point the bit rotary steerable system in directional drilling prototype well-bore profiles. In SPE/AAPG Western Regional Meeting. Society of Petroleum Engineers.

[11] Gravley, W., 1983. Review of downhole measurement-while-drilling systems. Journal of Petroleum Technology, 35(08), pp.1-439.

[12] Moore, J.C., Shipley, T.H., Goldberg, D., Ogawa, Y., Filice, F., Fisher, A., Jurado, M.J., Moore, G.F., Rabaute, A., Yin, H. and Zwart, G., 1995. Abnormal fluid

pressures and fault-zone dilation in the Barbados accretionary prism: Evidence from logging while drilling. Geology, 23(7), pp.605-608.

[13] Klotz, C., Bond, P.R., Wassermann, I. and Priegnitz, S., 2008, January. A new mud pulse telemetry system for enhanced MWD/LWD applications. In IADC/SPE Drilling Conference. Society of Petroleum Engineers.

[14] de Almeida Jr, I.N., Antunes, P.D., Gonzalez, F.O.C., Yamachita, R.A., Nascimento, A. and Goncalves, J.L., 2015. A review of telemetry data transmission in unconventional petroleum environments focused on information density and reliability. Journal of Software Engineering and Applications, 8(09), p.455.

[15] Jellison, M.J., Hall, D.R., Howard, D.C., Hall Jr, H.T., Long, R.C., Chandler, R.B. and Pixton, D.S., 2003, January. Telemetry drill pipe: enabling technology for the downhole internet. In SPE/IADC drilling conference. Society of Petroleum Engineers.

[16] Tucker, W. R., and Wang, C., 1999, "An Integrated Model for Drill-String Dynamics," J. Sound Vib., 224(1), pp. 123–165.

[17] Jansen, J. D., 1991, "Non-Linear Rotor Dynamics as Applied to Oilwell Drill- string Vibrations," J. Sound Vib., 147(1), pp. 115–135.

[18] Elsayed, M. A., Dareing, D. W., and Vonderheide, M. A., 1997, "Effect of Torsion on Stability, Dynamic Forces, and Vibration Characteristics in Drill- strings," ASME J. Energy Resour. Technol., 119(1), pp. 11–19.

[19] Macpherson, J. D., Mason, J. S., and Kingman, J. E. E., 1993, "Surface Measurement and Analysis of Drill-String Vibrations While Drilling," SPE/IADC Drilling Conference, Amsterdam, The Netherlands, Feb. 22–25, pp. 953–963.

[20] Dunayevsky, V.A., Abbassian, F. and Judzis, A., 1993. Dynamic stability of drillstrings under fluctuating weight on bit. SPE drilling & completion, 8(02), pp.84-92.

[21] Spanos, P.D., Sengupta, A.K., Cunningham, R.A. and Paslay, P.R., 1995. Modeling of roller cone bit lift-off dynamics in rotary drilling. Journal of Energy ResourcesTechnology, 117(3), pp.197-207.

[22] Feng, T., Zhang, H. and Chen, D., 2017, May. Dynamic programming based controllers to suppress stick-slip in a drilling system. In American Control Conference (ACC), 2017(pp. 1302-1307). IEEE.

[23] Chevallier, A.M., 2001. Nonlinear stochastic drilling vibrations (Doctoral dissertation, Rice University). pp. 20.

[24] Richard, Thomas, Christophe Germay, and Emmanuel Detournay. A simplified model to explore the root cause of stickslip vibrations in drilling systems with drag bits. Journal of sound and vibration 305.3 (2007): 432-456.

[25] Skaugen, E., 1987, January. The effects of quasi-random drill bit vibrations upon drillstring dynamic behavior. In SPE Annual Technical Conference and Exhibition. Society of Petroleum Engineers.

[26] Feng, T., Vadali, M., Ma, Z., Chen, D. and Dykstra, J., 2017. A Finite Element Method with Full Bit-Force Modeling to Analyze Drillstring Vibration. Journal of Dynamic Systems, Measurement, and Control.

[27] Close, D.A., Owens, S.C. and MacPherson, J.D., 1988, January. Measurement of BHA vibration using MWD. In SPE/IADC Drilling Conference. Society of Petroleum Engineers.

[28] Cook, R.L., Nicholson, J.W., Sheppard, M.C. and Westlake, W., 1989, January. First real time measurements of downhole vibrations, forces, and pressures used to monitor directional drilling operations. In SPE/IADC drilling conference. Society of Petroleum Engineers.

[29] Cunningham, R.A., 1968. Analysis of downhole measurements of drill string forces and motions. Journal of Engineering for Industry, 90(2), pp.208-216.

[30] Heisig, G., Sancho, J. and Macpherson, J.D., 1998, January. Downhole diagnosis of drilling dynamics data provides new level drilling process control to driller. In SPE Annual Technical Conference and Exhibition. Society of Petroleum Engineers.

[31] Robnett, E.W., Heisig, G., McGinley, P.J. and Macpherson, J.D., 2002, January. Real-time Downhole Drilling Process Data Complement Surface Data in Drilling

Optimization. In IADC/SPE Asia Pacific Drilling Technology. Society of Petroleum Engineers.

[32] Schlumberger: Drilling Dynamics Sensors and Optimization

[33] Ertas, D., Bailey, J.R., Wang, L. and Pastusek, P.E., 2014. Drillstring mechanics model for surveillance, root cause analysis, and mitigation of torsional vibrations. SPE Drilling & Completion, 29(04), pp.405-417.

[34] Jansen, J.D., Nonlinear Dynamics of Oilwell Drillstrings, in Delft University of Technology. 1993, Delft University of Technology: Delft University Press.

[35] Johancsik, C.A., Friesen, D.B. and Dawson, R., 1984. Torque and drag in directional wells-prediction and measurement. Journal of Petroleum Technology, 36(06), pp.987-992.

[36] Sheppard, M.C., Wick, C. and Burgess, T., 1987. Designing well paths to reduce drag and torque. SPE Drilling Engineering, 2(04), pp.344-350.

[37] Tikhonov, V., Valiullin, K., Nurgaleev, A., Ring, L., Gandikota, R., Chaguine, P. and Cheatham, C., 2014. Dynamic Model for Stiff-String Torque and Drag. SPE Drilling & Completion, 29(03), pp.279-294.

[38] Ho, H.S., 1988, January. An improved modeling program for computing the torque and drag in directional and deep wells. In SPE Annual Technical Conference and Exhibition. Society of Petroleum Engineers.

[39] Rezmer-Cooper, I., Chau, M., Hendricks, A., Woodfine, M., Stacey, B. and Downton, N., 1999, January. Field data supports the use of stiffness and tortuosity in solving complex well design problems. In SPE/IADC drilling conference. Society of Petroleum Engineers.

[40] Menand, S., Sellami, H., Tijani, M., Stab, O., Dupuis, D.C. and Simon, C., 2006, January. Advancements in 3D drillstring mechanics: from the bit to the topdrive. In IADC/SPE drilling conference. Society of Petroleum Engineers.

[41] Mitchell, R.F., Bjorset, A. and Grindhaug, G., 2015. Drillstring analysis with a discrete torque/drag model. SPE Drilling & Completion, 30(01), pp.5-16.

[42] Tan Meilan. Double nonlinear finite element method on drillstring in 3D curved wellbores. (Doctoral dissertation, Nanjing University of aeronautics and astronautics), 2004. (in Chinese)

[43] Millheim, K., Jordan, S., & Ritter, C. J. (1978). Bottom-hole assembly analysis using the finite-element method. Journal of Petroleum Technology, 30(02), 265-274.

[44] Wilson, J.K. and Heisig, G., 2015. Nonlinear Drillstring-Dynamics Modeling of Induced Vibrations in Unconventional Horizontals. SPE Drilling & Completion, 30(03), pp.243-256.

[45] Bailey, J. R., Biediger, E., Sundararaman, S., Carson, A. D., Elks, W. C., and Dupriest, F. E. (2008, January). Development and application of a BHA vibrations model. In International Petroleum Technology Conference. International Petroleum Technology Conference.

[46] Bailey, J. R., and Remmert, S. M. (2010). Managing drilling vibrations through BHA design optimization. SPE Drilling & Completion, 25(04), 458-471.

[47] Spanos, P.D., Payne, M.L. and Secora, C.K., 1997. Bottom-hole assembly modeling and dynamic response determination. Journal of Energy Resources Technology, 119(3), pp.153-158.

[48] Yigit, A. S., and Christoforou, A. P., 1998, "Coupled Torsional and Bending Vibrations of Drillstrings Subject to iMPact With Friction," J. Sound Vib., 215(1), pp. 167–181.

[49] Christoforou, A. P., and Yigit, A. S., 1997, "Dynamic Modelling of Rotating Drillstrings With Borehole Interactions," J. Sound Vib., 206(2), pp. 243–260.

[50] Leine, R. I., Van Campen, D. H., and Keultjes, W. J. G., 2002, "Stick-Slip Whirl Interaction in Drillstring Dynamics," ASME J. Vib. Acoust., 124(2), pp. 209–220.

[51] Vadali, M., Sun, Z., Xue, Y., and Dykstra, J., 2014, "Dynamic Modeling of Bottomhole Assembly," ASME Paper No. DSCC2014-5927.

[52] Han, J.H., Kim, Y.J. and Karkoub, M., 2013. Modeling of wave propagation in drill strings using vibration transfer matrix methods. The Journal of the Acoustical Society of America, 134(3), pp.1920-1931.

[53] Kreuzer, E. and Steidl, M., 2012. Controlling torsional vibrations of drill strings via decomposition of traveling waves. Archive of Applied Mechanics, 82(4), pp.515-531.

[54] Millheim, K.K. and Apostal, M.C., 1981. The effect of bottomhole assembly dynamics on the trajectory of a bit. Journal of Petroleum Technology, 33(12), pp.2-323.

[55] Khulief, Y.A. and Al-Naser, H., 2005. Finite element dynamic analysis of drillstrings. Finite elements in analysis and design, 41(13), pp.1270-1288.

[56] Ritto, T.G., Soize, C. and Sampaio, R., 2009. Non-linear dynamics of a drill-string with uncertain model of the bit–rock interaction. International Journal of Non-Linear Mechanics, 44(8), pp.865-876.

[57] Arbatani, S., Callejo, A., Kövecses, J., Kalantari, M., Marchand, N.R. and Dargahi, J., 2016. An approach to directional drilling simulation: finite element and finite segment methods with contact. Computational Mechanics, 57(6), pp.1001-1015.

[58] Dong, G. and Chen, P., 2016. A Review of the Evaluation, Control, and Application Technologies for Drill String Vibrations and Shocks in Oil and Gas Well. Shock and Vibration, 2016.

[59] Barton, S.P., May, H.S. and Johnson, S., 2009. Gauge, Cutting Structure, Torque Control Components--What Really Counts for Optimal Tool Face Control With FC Drill Bits?. SPE Drilling & Completion, 24(02), pp.293-300.

[60] Pessier, R. and Damschen, M., 2011. Hybrid bits offer distinct advantages in selected roller-cone and PDC-bit applications. SPE Drilling & Completion, 26(01), pp.96-103.

[61] Schwefe, T., Ledgerwood III, L.W., Jain, J.R., Fuselier, D.M., Oueslati, H. and Endres, L., 2014, March. Development and testing of stick/slip-resistant PDC bits. In IADC/SPE Drilling Conference and Exhibition. Society of Petroleum Engineers.

[62] Skaugen, E. and Kyllingstad, A., 1986, January. Performance testing of shock absorbers. In SPE Annual Technical Conference and Exhibition. Society of Petroleum Engineers.

[63] Reimers, N., 2012. Antistall tool reduces risk in drilling difficult formations. Journal of Petroleum Technology, 64(01), pp.26-29.

[64] Dareing, D.W., 1984. Drill collar length is a major factor in vibration control. Journal of petroleum technology, 36(04), pp.637-644.

[65] Dunlop, J., Isangulov, R., Aldred, W.D., Sanchez, H.A., Flores, J.L.S., Herdoiza, J.A., Belaskie, J. and Luppens, C., 2011, January. Increased rate of penetration through automation. In SPE/IADC Drilling Conference and Exhibition. Society of Petroleum Engineers.

[66] Sevrarens, A.F.A., vanden Molengraft, M.J.G., Kok, J.J. and vanden Steen, L., 1998. H∞ control for suppressing stick-slip in oil well drillstring. Trans IEEE, Control System, (4), pp.19-30.

[67] Hernandez-Suarez, R., Puebla, H., Aguilar-Lopez, R. and Hernandez-Martinez, E., 2009. An integral high-order sliding mode control approach for stick-slip suppression in oil drillstrings. Petroleum Science and Technology, 27(8), pp.788-800.

[68] Li, L., Zhang, Q. and Rasol, N., 2011. Time-Varying Sliding Mode Adaptive Control for Rotary Drilling System. JCP, 6(3), pp.564-570.

[69] Zribi, M., Karkoub, M. and Huang, C.C., 2011. Control of stick-slip oscillations in oil well drill strings using the back-stepping technique. International Journal of Acoustics and Vibration, 16(3), p.134.

[70] Halsey, G.W., Kyllingstad, A. and Kylling, A., 1988, January. Torque feedback used to cure slip-stick motion. In SPE Annual Technical Conference and Exhibition. Society of Petroleum Engineers.

[71] Tucker, W.R. and Wang, C., 1999. On the effective control of torsional vibrations in drilling systems. Journal of Sound and Vibration, 224(1), pp.101-122.

[72] Jansen, J.D. and Van den Steen, L., 1995. Active damping of self-excited torsional vibrations in oil well drillstrings. Journal of sound and vibration, 179(4), pp.647-668.

[73] Kyllingstad, A. and Nessjøen, P.J., 2009, January. A new stick-slip prevention system. In SPE/IADC Drilling Conference and Exhibition. Society of Petroleum Engineers.

[74] Kyllingstad, A. and Nessjoen, P.J., 2010, January. Hardware-in-the-Loop Simulations Used as a Cost-Efficient Tool for Developing an Advanced Stick-Slip Prevention

System. In IADC/SPE Drilling Conference and Exhibition. Society of Petroleum Engineers.

[75] Sawaryn, S.J. and Thorogood, J.L., 2003, January. A compendium of directional calculations based on the minimum curvature method. In SPE annual technical conference and exhibition. Society of Petroleum Engineers.

[76] Atluri, S.N. and Cazzani, A., 1995. Rotations in computational solid mechanics. Archives of Computational Methods in Engineering, 2(1), pp.49-138.

[77] Zupan, D. and Saje, M., 2003. The three-dimensional beam theory: Finite element formulation based on curvature. Computers & structures, 81(18), pp.1875-1888.

[78] Liu, M. and Gorman, D.G., 1995. Formulation of Rayleigh damping and its extensions. Computers & structures, 57(2), pp.277-285.

[79] Le, T.N., Battini, J.M. and Hjiaj, M., 2011. Efficient formulation for dynamics of corotational 2D beams. Computational Mechanics, 48(2), pp.153-161.

[80] Feng, T., Kim, I. and Chen, D., 2018. Dynamic Modeling of Directional Drillstring: A Linearized Model Considering Well Profile. Journal of Dynamic Systems, Measurement, and Control, 140(6), p.061005.

[81] Dawe, D.J., 1974. Numerical studies using circular arch finite elements. Computers & Structures, 4(4), pp.729740.

[82] Sabir, A.B. and Ashwell, D.G., 1971. A comparison of curved beam finite elements when used in vibration problems. Journal of Sound and Vibration, 18(4), pp.555-563.

[83] Reissner, E., 1972. On one-dimensional finite-strain beam theory: the plane problem. Zeitschrift für angewandte Mathematik und Physik ZAMP, 23(5), pp.795-804.

[84] Simo, J.C., 1985. A finite strain beam formulation. The three-dimensional dynamic problem. Part I. Computer methods in applied mechanics and engineering, 49(1), pp.55-70.

[85] Romero, I., 2008. A comparison of finite elements for nonlinear beams: the absolute nodal coordinate and geometrically exact formulations. Multibody System Dynamics, 20(1), pp.51-68.

[86] Koziey, B.L. and Mirza, F.A., 1994. Consistent curved beam element. Computers & structures, 51(6), pp.643654.

[87] Litewka, P. and Rakowski, J., 1997. An efficient curved beam finite element. International Journal for Numerical Methods in Engineering, 40(14), pp.2629-2652.

[88] Dawe, D.J., 1974. Numerical studies using circular arch finite elements. Computers & Structures, 4(4), pp.729740.

[89] Palaninathan, R. and Chandrasekharan, P.S., 1985. Curved beam element stiffness matrix formulation. Computers & structures, 21(4), pp.663-669.

[90] Raveendranath, P., Singh, G. and Pradhan, B., 2000. Free vibration of arches using a curved beam element based on a coupled polynomial displacement field. Computers & Structures, 78(4), pp.583-590.

[91] Choi, J.K. and Lim, J.K., 1993. Simple curved shear beam elements. Communications in numerical methods in engineering, 9(8), pp.659-669.

[92] Feng, T., Bakshi, S., Gu, Q., Chen, D., 2019. A Finite Element Modeling Framework for Planar Curved Beam Dynamics Considering Nonlinearities and Contacts. Journal of Computational and Nonlinear Dynamics, doi: 10.1115/1.4043452.

[93] Feng, T., Gu, Q., Kim, I. and Chen, D., 2018, September. Dynamic Analyses of Directional Drilling Using Curved Beam Theorem. In ASME 2018 Dynamic Systems and Control Conference (pp. V002T17A001-V002T17A001). American Society of Mechanical Engineers.

[94] Pai, P.F. and Palazotto, A.N., 1996. Large-deformation analysis of flexible beams. International Journal of Solids and Structures, 33(9), pp.1335-1353.

[95] Burr, A.H., 1981. Mechanical analysis and design-Chapter 10. Elsevier North-Holland, xxvi+ 640, 26 x 19 cm.

[96] Fumio, K., 1975. On the validity of the finite element analysis of circular arches represented by an assemblage of beam elements. Computer Methods in Applied Mechanics and Engineering, 5(3), pp.253-276.

[97] Huněk, I., 1993. On a penalty formulation for contact-impact problems. Computers & structures, 48(2), pp.193203.

[98] Detournay, E. and Defourny, P., 1992, January. A phenomenological model for the drilling action of drag bits. In International journal of rock mechanics and mining sciences & geomechanics abstracts (Vol. 29, No. 1, pp. 13-23). Pergamon.

[99] Detournay, E., Richard, T. and Shepherd, M., 2008. Drilling response of drag bits: theory and experiment. International Journal of Rock Mechanics and Mining Sciences, 45(8), pp.1347-1360.

[100] Feng, T., Vadali, M. and Chen, D., 2017, October. Modeling and Analysis of Directional Drilling Dynamics. In ASME 2017 Dynamic Systems and Control Conference (pp. V003T43A006-V003T43A006). American Society of Mechanical Engineers.

[101] Perneder, L., Detournay, E. and Downton, G., 2012. Bit/rock interface laws in directional drilling. International Journal of Rock Mechanics and Mining Sciences, 51, pp.81-90.

[102] Christoforou, A.P. and Yigit, A.S., 2003. Fully coupled vibrations of actively controlled drillstrings. Journal of sound and vibration, 267(5), pp.1029-1045.

[103] Dawson, R., 1984. Drill pipe buckling in inclined holes. Journal of Petroleum Technology, 36(10), pp.1-734.

[104] Qian-bei, Y., Ju-bao, L. and Ri-zhi, D., 2017. The research of post-buckling about slender rod string in wellbore based on energy method and experiment. Journal of Petroleum Science and Engineering, 156, pp.732-739.

[105] Karnopp, D., 1985. Computer simulation of stick-slip friction in mechanical dynamic systems. Journal of dynamic systems, measurement, and control, 107(1), pp.100-103.

[106] Tanese, R., 1989. Distributed genetic algorithms for function optimization.

[107] Beasley, J.E. and Chu, P.C., 1996. A genetic algorithm for the set covering problem. European journal of operational research, 94(2), pp.392-404.

[108] Haupt, R.L., Haupt, S.E. and Haupt, S.E., 1998. Practical genetic algorithms (Vol. 2). New York: Wiley.

[109] Carr, J., 2014. An introduction to genetic algorithms. Senior Project, 1, p.40.

[110] Bhattacharjya, R.K., 2012. Introduction to genetic algorithms. IIT Guwahati, 12.

[111] Feng, T., Bakshi, S., Gu, Q., Yan, Z., Chen, D., 2019. Design Optimization of Bottom-Hole Assembly to Reduce Drilling Vibration. Accepted by Journal of Petroleum Science and Engineering.

[112] Gressick, W., Wen, J.T. and Fish, J., 2005. Order reduction for large-scale finite element models: A systems perspective. International Journal for Multiscale Computational Engineering, 3(3).

[113] Canudas-de-Wit, C., Rubio, F.R. and Corchero, M.A., 2008. D-OSKIL: A new mechanism for controlling stick-slip oscillations in oil well drillstrings. IEEE Transactions on Control Systems Technology, 16(6), pp.1177-1191.

[114] Navarro-López, E.M. and Cortés, D., 2007, July. Sliding-mode control of a multi-DOF oilwell drillstring with stick-slip oscillations. In 2007 American Control Conference (pp. 3837-3842). IEEE.

[115] Márquez, M.B.S., Boussaada, I., Mounier, H. and Niculescu, S.I., 2015. Analysis and Control of Oilwell Drilling Vibrations. In A Time-Delay Systems Approach, ser. Advances in Industrial Control. Springer.

[116] Johnsen, E., Richard E. Bellman and Stuart E. Dreyfus: Applied Dynamic Programming. Princeton University Press, 1962. 363 s., 8, 50$. Ledelse og Erhvervsøkonomi.

[117] Bertsekas, D.P., Bertsekas, D.P., Bertsekas, D.P. and Bertsekas, D.P., 1995. Dynamic programming and optimal control (Vol. 1, No. 2). Belmont, MA: Athena scientific.

[118] Navarro-López, E.M. and Suárez, R., 2004, September. Practical approach to modelling and controlling stick-slip oscillations in oilwell drillstrings. In Proceedings of the 2004 IEEE International Conference on Control Applications, 2004.(Vol. 2, pp. 1454-1460). IEEE.

Visa

Tianheng Feng was born in Jiangsu, China in 1991. He received the B.S. degree and the M.S. degree in Mechanical Engineering from Shanghai Jiao Tong University, in 2013 and 2015, respectively. In 2015, he started his Ph.D. program in Mechanical Engineering at The University of Texas at Austin. His current research interests include dynamic system modeling and control with applications in directional drilling, lithium-ion battery, electrical vehicles etc.

Email: f.tianheng@utexas.edu

This dissertation was typed by Tianheng Feng